UNIVERSITY OF COPENHAGEN

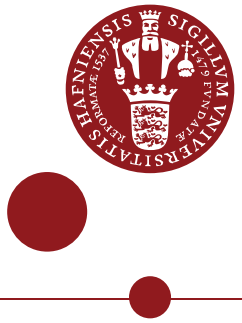

PhD in Computer Science

Dynamic Tomography Imaging of Biological Structures

Reconstructing the dynamic tailbeating of sperm

Mette Bjerg Lindhøj

Supervised by Tim B. Dyrby and Jon Sporring

December 17, 2021

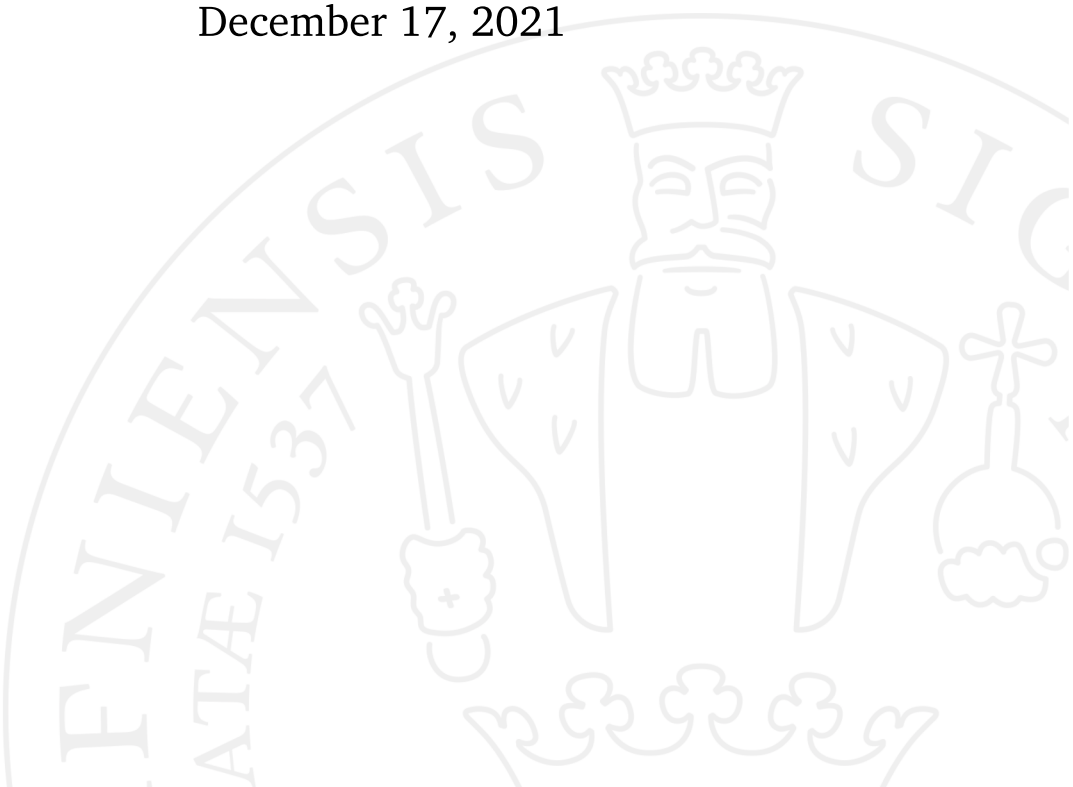

Mette Bjerg Lindhøj
Dynamic Tomography Imaging of Biological Structures
PhD in Computer Science, December 17, 2021
Supervisors: Tim B. Dyrby and Jon Sporring

University of Copenhagen
Faculty of Science
PhD Degree in Computer Science
Universitetsparken 5
2100 Copenhagen Ø

Preface

This PhD project aimed to determine whether synchrotron X-ray imaging can be used for 3D+time imaging of live sperm tail beating as part of the MAX4Imagers project (PI: Tim Dyrby) funded by the Capital Region Research Foundation (Grant number: A5657). No synchrotron X-ray data exists of live sperm. Hence, gathering data for reconstruction has been a big part of the project and has proven very challenging. Finding a way to obtain data has meant scouring the literature within many different fields and collaborating with experts from many domains. With a background in software development and mathematics, this has been time-consuming and challenging as it has required me to gather knowledge far outside my field. Below I will describe the process which led to this final work.

One significant challenge of this project has been designing a way of imaging the sperm in a synchrotron and getting synchrotron time for experimenting. Initially, Henning Friis Poulsen and Carsten Gundlach of the Technical University of Denmark (DTU) were contacted to help shed some light on how sperm could be imaged by synchrotron X-ray tomography. They mentioned that sperm are typically imaged in the water window due to the optimal contrast conditions in this unique spectral region. However, such imaging requires cryo-conditions, and as frozen sperm do not move, it was necessary to look for an alternative. Therefore, Rajmund Mokso was contacted, who suggested working with Anne Bonnin at the TOMCAT Nanoscope of the Swiss Light Source. The Nanoscope was chosen as it has the resolution and field of view needed to see sperm. Furthermore, the Nanoscope offers fast imaging, which is needed for dynamic imaging. A total of three proposals were submitted to PSI.

The first synchrotron proposal was rejected because the feasibility of the experiment was questioned by the experts assessing the proposals. Anne Bonnin very generously spent some of her beamtime to help us improve the setup. There were two significant issues; the first was that the sperm tails did not provide any contrast. Many possible solutions were explored with help from two friends, Anne Zebitz from the Department of Health Technology at DTU and Troels Elmer Jeppesen from the Department of Biomedical Sciences at the University of Copenhagen (KU). In the end, attaching iron-oxide nanoparticles to the cells was the method of choice, which required the help of Kirsten Marie Ørnsbjerg Jensen, Susan Rudd Cooper and Andy Sode Anker from the Department of Chemistry, KU, for synthesizing the nanoparticles. The particles were attached to the cells with help from Kristian Almstrup and Sissel Marie Bredesen at Rigshospitalet. The attachment was verified using transmission electron microscopy (TEM), which required the help of Klaus Qvotrup and Zhila Nikrozi at the Core Facility for Integrated Microscopy, KU. The initial TEM images showed that more particles had to be loaded into the cells. Mie Kristensen from the Department of Pharmacy, KU, generously spent her time helping me solve this challenge.

The second big obstacle for a successful experiment was practical issues related to creating small samples. For the static samples, the help came from a surprising source. A family member and mechanic by trade, Søren Isaksen, came up with a fast way of polishing all my static Epon samples, and for that, he deserves a big thank you. For the live samples, the challenge was even greater. By advice from Anne Bonnin and Rajmund Mokso, catching a single sperm and containing it within the beam was deemed the most promising sample for dynamic live imaging. However, both sperm and beam are in the micrometre scale, and handling samples this small is not straightforward. Morten Rønn Petersen at Rigshospital spent time with me trying to catch and contain a single cell with his specialized ICSI equipment. Unfortunately, as the equipment was not portable or available at the beamline, custom labware that could perform the task of catching a single sperm had to be built. Lasse Højlund Eklund Thamdrup made custom containers at DTU to contain the sperm within the beam.

The second beamtime proposal was rejected because of the COVID-19 situation. I want to acknowledge The Paul Scherrer Institut, Villigen, Switzerland, for accepting the third proposal and provisioning synchrotron radiation beamtime

(20201724) at the beamline TOMCAT of the Swiss Light Source. Anne Bonnin of PSI deserves a special thank you for spending her beamtime performing the initial tests and being a big help during the beamtime. Visiting her at PSI and working together towards seeing live sperm in her Nanoscope was the high point of my PhD. To all the people who helped make this come true, thank you. Unfortunately, collecting data of live cells was never successful, and because the beamtime was only available late in the project, a solution has not been found to the two remaining problems; the sperm motility is quickly affected by the ionizing radiation, and the liquid in the small container holding the sperm sample evaporates almost immediately. Thank you to the Center for Quantification of Imaging Data from MAX IV (QIM), funded by The Regional Council of Denmark (Regionsrådet) in The Capital Region of Denmark, for extending my salary. The funding allowed me time to finish despite many challenges and late results.

A second challenge of the project has been the dynamic reconstruction. Because the sperm movement is fast and complex, no algorithms were found to perform the reconstruction. Therefore, much research was done into using other imaging modalities to model the sperm movement, which could guide the tomographic reconstruction. One of these methods were based on using TEM. Thank you, William Laprade and Silas Nyboe Ørting from the QIM group, for all your work on the segmentation for building the model. While the segmentation proved challenging and never fully succeeded, there is still hope that the data can be used in the future. Another modality we tried was Light Sheet Fluorescent Imaging. Thank you to Gustavo Castro and Emilio Gualda at the Spanish Institute of Photonic Sciences for letting me visit and continuing the work. Within the last month of this project, they demonstrated promising results for future sperm imaging. Unfortunately, it was too late to include conclusive results in this thesis, but the data is still being analyzed by a master student who has taken over this side project.

Even though a 3D+time reconstruction was never achieved, much progress was made, and many challenges were overcome during the project. Thank you to everyone who helped me along the way and my friends and family for their support. My supervisors Jon Sporring and Tim Dyrby deserve a final thank you for all their kindness and encouragement along the way.

Abstract

Dynamic tomographic imaging can visualize 3D biomechanical systems in action at a very high resolution. Very few imaging techniques make this possible, which makes the modality very desirable for answering questions about the dynamics of biological samples. However, dynamic tomographic imaging of biological samples is complex for three reasons. Firstly obtaining contrast in living soft tissue can be difficult. Secondly, the sample is exposed to ionizing radiation during imaging, which is harmful to live samples. Finally, dynamic tomographic reconstruction is complex, and the approach depends on the dynamics of the object. In this thesis, sperm cells were chosen as the sample of choice because studying their 3D tail-beating pattern is important for understanding factors related to fertility. Furthermore, sperm cells are an excellent object for probing the limits of 3D dynamic imaging systems because they are small, fast-moving and easy to come by. The main results presented are threefold. Firstly, a non-toxic labelling method based on iron-oxide nanoparticles was developed for imaging the sperm, and it is shown that labelling with nanoparticles is also practical for dynamic tomographic reconstruction. Secondly, a practical approach to assessing the functional radiation damage caused to living sperm by synchrotron radiation is presented. Finally, a high-level parallel programming approach to tomographic reconstruction was developed, which is hardware-independent and especially well suited for speeding up sparse reconstruction.

Contents

1 Introduction

Can Synchrotron X-ray tomography (SXRT) be used for reconstructing the dynamic tail beating pattern of living sperm in 3D?

The above question is the leading research question studied in this thesis, and it is relevant for two main reasons. Firstly, methods that allow imaging of the 3D dynamics of sperm tail beating are needed to understand sperm motility and human reproduction factors. Secondly, SXRT is a unique modality in that it can be used for fast, high-resolution 3D dynamic imaging of live biological samples [27] and sperm are suitable for probing the limits of the modality as they are small, fast-moving and easy to come by.

Answering the main research question has posed many challenges, and therefore many possible solutions have been explored. In the following, the main sub-questions discussed in the subsequent chapters are briefly described

How can we obtain a signal from a swimming sperm for SXRT imaging?

This question is investigated in Chapter 2. Sperm and the aqueous environment they need to survive have similar X-ray attenuation properties, making it difficult to see live cells. Therefore, different methods were explored for enhancing the contrast in the X-ray projections. The most promising of these methods was staining the cells with iron-oxide nanoparticles. In the chapter, an article under review about this approach is presented. Furthermore, an idea is presented for an experimental setup for catching and containing a single cell within the field of view of the synchrotron. The data will be released upon acceptance of the article.

Can the sperm survive the beam?

X-rays cause radiation damage to living tissue. Hence, it is highly relevant to understand whether the movement of the sperm would remain natural

when inside the X-ray beam from the synchrotron. In Chapter 3 the effect of the beam on the cells is investigated. An article under submission with results from analysing the videos is presented. The data will be released upon acceptance of the article.

What are the possibilities and limitations of dynamic tomography? Classical tomographic algorithms have an underlying assumption that the object to be reconstructed is static during the complete acquisition of the projection data. However, living samples often violate this assumption, leading to poor reconstructions. In Chapter 4 a brief introduction to classical tomographic reconstruction algorithms is given. Then some sparse reconstruction algorithms and dynamic algorithms are evaluated to assess whether these approaches could be applied to reconstruct a dynamic sperm. The chapter also includes an article on a parallel implementation of forward and back-projection, especially well suited for sparse problems, accepted at the High-Performance Computing & Simulation Conference 2019.

Several data sets have been collected to investigate the research question. They are described in brevity below. Some of the data sets are still being used for ongoing research projects.

3D Synchrotron Data All the synchrotron volumes of sperm have been collected at the TOMCAT beamline (Swiss Light Source (SLS)), as this instrument has the most promising specs in terms of spatial and temporal resolution. In the first data set, we imaged unstained cells. However, the cells were not visible, only the dense DNA found in the sperm head region. Therefore various contrast methods were examined, including inverse staining with Gadolinium, Osmium staining and staining with iron-oxide nanoparticles as discussed in Chapter 2. See Figure 1.1 for an example of the synchrotron data.

Videos of sperm inside the beam Several videos were recorded with a digital microscope during X-ray exposure to the synchrotron beam. See Figure 1.2 for an example of one of the video frames, and Chapter 3 for more details.

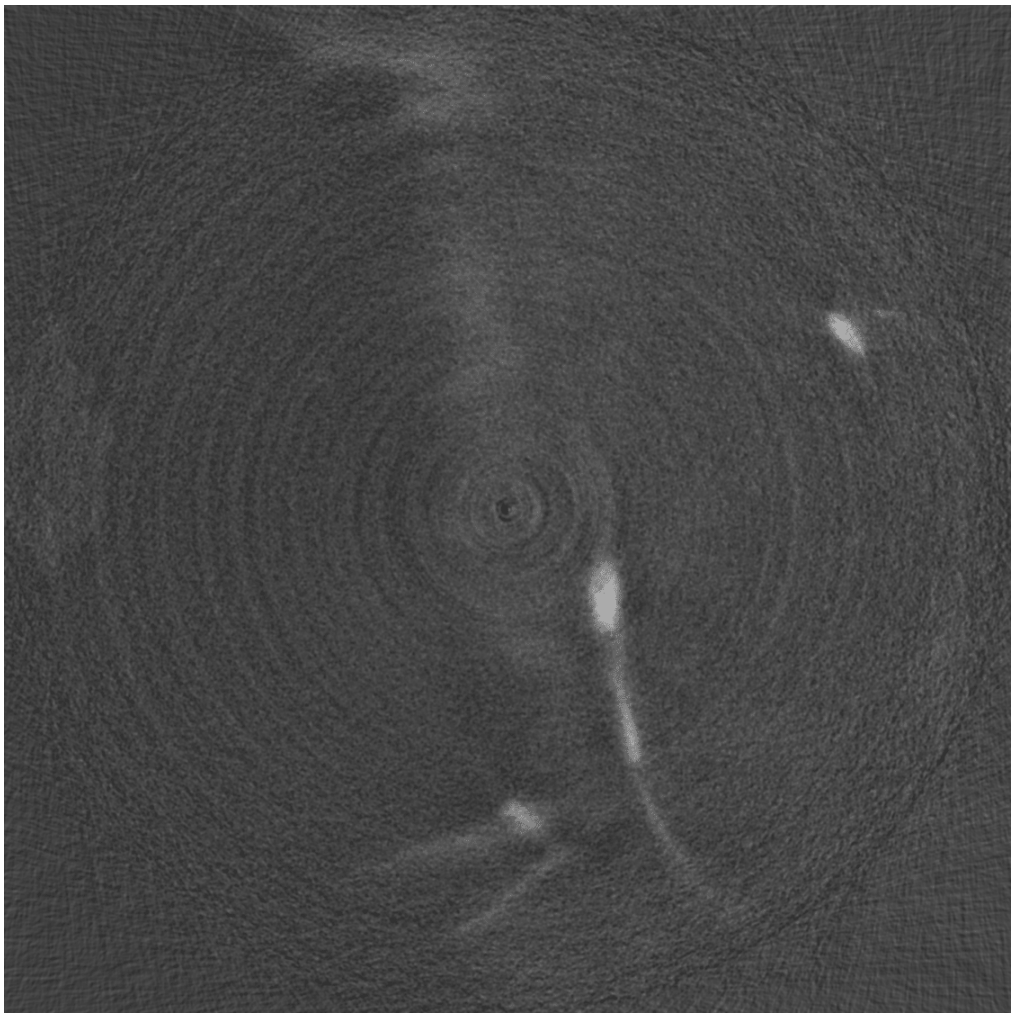

Figure 1.1.: Synchrotron Data The image shows a slice of a reconstruction of Osmium stained sperm. The light shape is a cell.

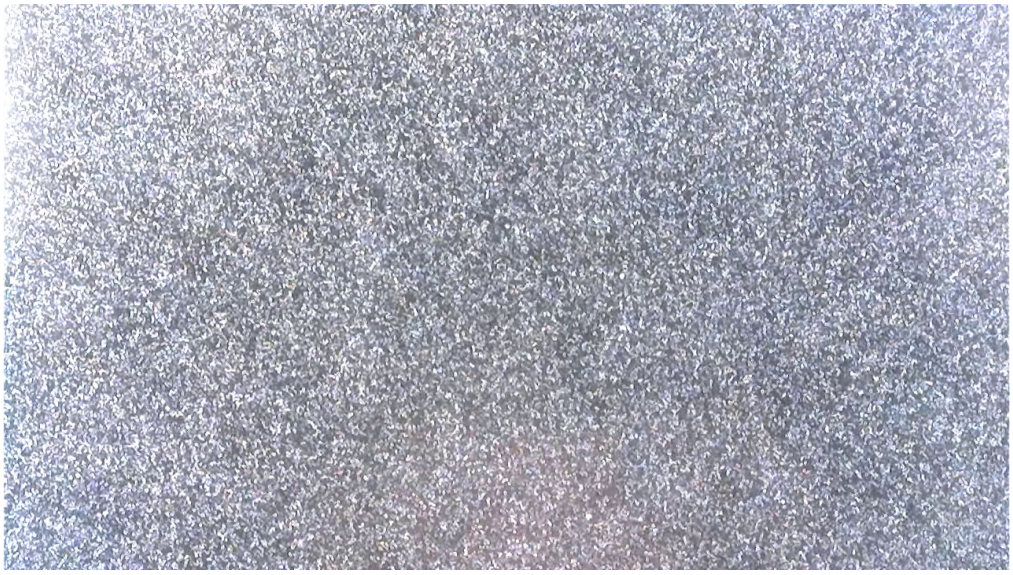

Figure 1.2.: **Video frame** The image shows a video frame from one of the videos recorded with a microscope camera to determine the effect of the synchrotron beam on the movement of the cells. The cells are all the bright dots in the image.

3D cone-beam Micro-CT of homemade phantom Four 3D volumes of cone-beam micro-ct data were collected at Helsinki University. The phantoms were worm-like, and the aim was to have some high-quality data for testing different tomographic reconstruction approaches. More details can be found in Chapter 4.

3D Electron Microscopy Two 3D Electron Microscopy data sets were collected at Core Facility for Integrated Microscopy, Department of Biomedical Sciences, Copenhagen University, one for human sperm and one for boar sperm. The data sets were collected to make a model of sperm poses. The data was also used to estimate the sperm sizes and compare human and boar sperm, as boar sperm were more practical to work with as they are more robust and easier to come by. The data has been partially segmented, but due to the high density of the cells, separating the cells has been difficult, and it seems unlikely that the cells poses are representative of natural swimming poses. See Figure 1.4 for a brief overview of the data. More information can be found in the Appendix A.

3D+time Light Sheet Fluorescent Microscopy Several 4D (3D+time) volumes of swimming sperm were collected. The boar sperm were stained

(a) Image of 4 phantoms

(b) A projection of S-shaped phantom

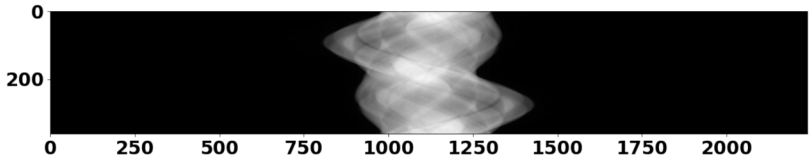

(c) Sinogram of central slice of S-shaped phantom with 361 projections and 2240 detector columns

Figure 1.3.: **Worm phantoms** (a): The four phantoms that were made of hair bands and play dough. (b): A projection of the S-shaped phantom is shown on the bottom right in the image (a). (c): A sinogram of the central slice of the S-shaped phantom with 2240 projections from 361 different angles.

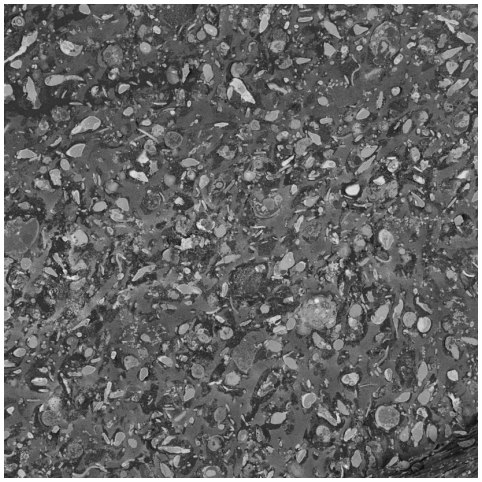

(a) Slice of human 3D EM data

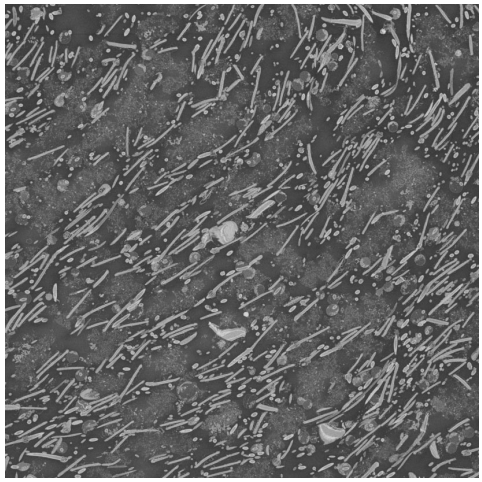

(b) Slice of boar 3D EM data

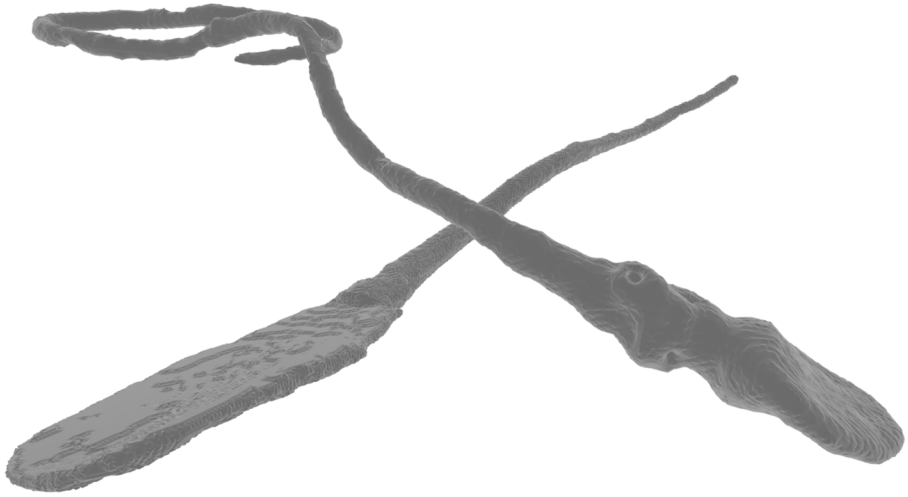

(c) 3D segmentation of a human and boar sperm from EM data

Figure 1.4.: 3D EM data: (a) and (b) show a slice of the 3D EM data from human sperm and boar sperm respectively. (c) shows a segmentation of a boar and human cell. Boar sperm are larger than human sperm and have flat heads, compared to the wedge-shaped head of human sperm. Both were segmented by a neural network. The human cell was post-processed by hand to get a complete cell. The boar sperm is missing a large part of the tail.

(a) Slice of LSFM data

(b) 3D segmentation of LSFM sperm data

Figure 1.5.: LSFM data: (a) Shows a slice of the data, the light oval shape in the centre of the image is part of a boar sperm head (b) An initial segmentation of the data. Due to the anisotropy of the data, the sperm shapes become distorted, and only some of the cell is visible in the segmentation.

with R18, a fluorescent dye. The data sets were acquired as an alternative to SXRT, and the aim was to use the data for modelling sperm tail movements. The resulting data sets show swimming sperm in 4D, but the spatial resolution of the microscope is highly an-isotropic, and the data contains unexplained artefacts. Some initial segmentation has been carried out, but very little of the tail is visible. More analysis of the data is required to detect any tail beating patterns. See Figure 1.5 for a brief overview of the data. More information can be found in Appendix B.

2 Contrast

How can we obtain a signal from a swimming sperm for SXRT imaging?

The question above is the central question studied in this chapter:

1. First, a brief introduction is given to synchrotron light and why synchrotrons can be suitable for dynamic SXRT imaging.

2. Then X-rays' contrast mechanisms are introduced to explain why obtaining contrast from moving sperms in a synchrotron is difficult.

3. Then an article based on the work carried out during the PhD is included, which proposes a novel contrast method for live cell SXRT imaging.

4. Finally, an experimental setup is proposed for imaging a single cell within the field of view of the Nanoscope, TOMCAT Beamline, Paul Scherrer Institute, which was used for the experiments.

X-rays are part of the electromagnetic spectrum; see Figure 2.1 and were first discovered by Wilhelm Conrad Röntgen, who was awarded the Nobel Prize in physics in 1901 for the discovery [32]. When the energy of a charged particle, such as an electron, changes from higher energy to lower energy, the difference in energy is emitted as electromagnetic radiation in the form of photons, which have an associated frequency and wavelength. In conventional X-ray tubes, thermal electrons escape from a heated cathode and are accelerated between the cathode and an anode. The X-rays are emitted when the electrons are decelerated upon hitting the anode material [25], see Figure 2.2.

The discovery of the synchrotron was made independently by Vladimir Veksler in 1944 and Edwin McMillan in 1945, and it differs from X-ray tubes in the way the particles are accelerated [23]. In a synchrotron, see Figure 2.5, the electrons are accelerated by shooting them through a linear accelerator (Linac),

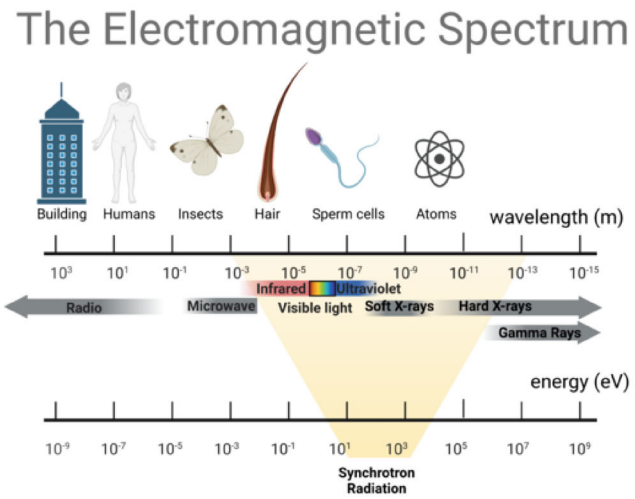

Figure 2.1.: Electromagnetic Spectrum. An illustration showing the electromagnetic spectrum with energies and wavelengths

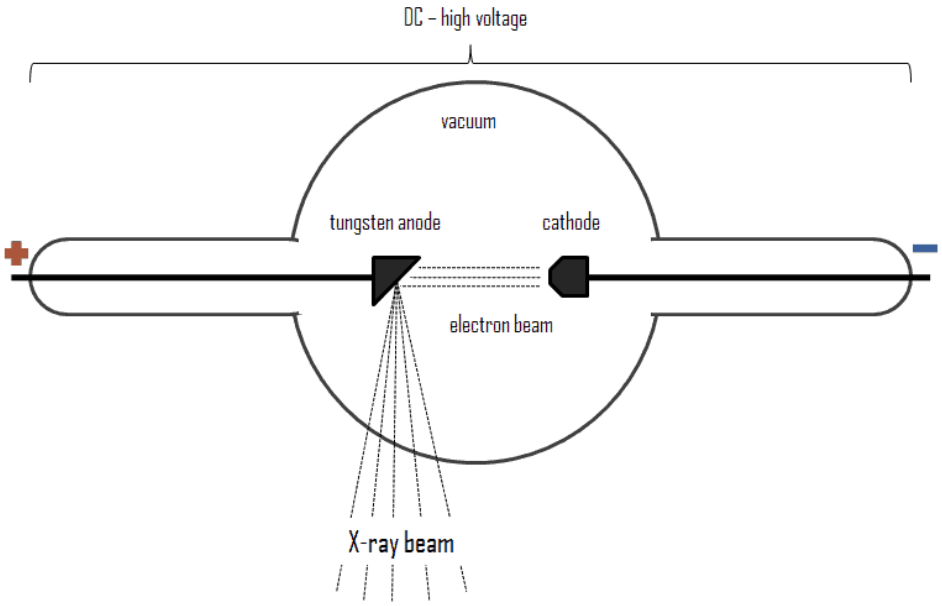

Figure 2.2.: Schematic drawing of X-ray tube. An illustration showing how X-rays are produced in a conventional X-ray tube. The image is from `www.radiation-dosimetry.org`

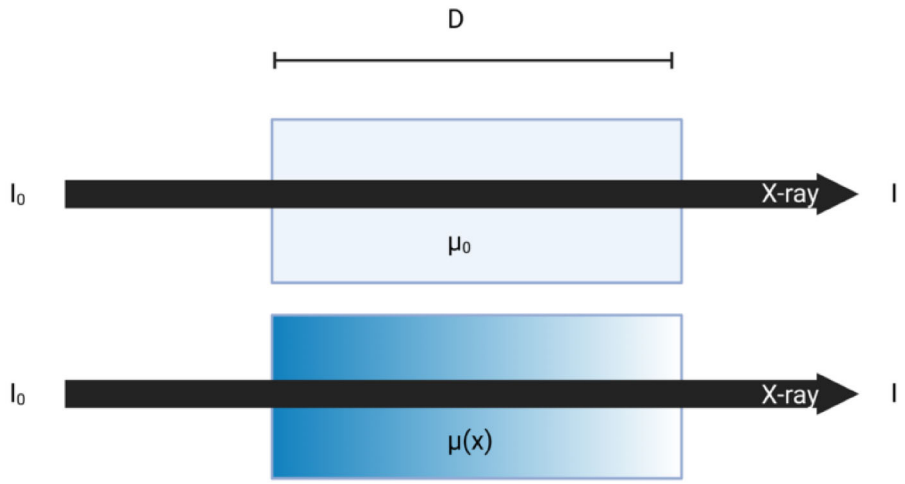

Figure 2.3.: Lambert-Beer law. An illustration of the attenuation of x-rays. On the top, a material with a constant attenuation coefficient μ_0 is considered passing through an object of length D. On the bottom, the material's attenuation $\mu(x)$ varies with the position x in the object.

which creates a high energy electron beam. The electrons are then focused and further accelerated by the use of magnets [26]. Once they reach their target energy, they can be stored a the storage ring, where the kinetic energy of the particles is kept constant. The X-rays are produced when the particles change direction. The emitted light is steered to the beamline and harvested with different optics to investigate objects of interest.

SXRT is based on tomographic reconstruction from X-ray projections which is discussed in Chapter 4. The simplest model for X-ray contrast is attenuation which is governed by the Lambert-Beer law [25]. Assume the unobstructed X-ray beam has intensity I_0, and after passing through the object, the intensity is reduced to I. The Lambert-Beer law states that I, which is proportional to the number of photons, is given by:

$$I(x - \Delta x) = I(x) - \mu I(x)\Delta x \tag{2.1}$$

when passing distance Δx through an object with attenuation coefficient μ [25], see Figure 2.3. By reordering and taking limits of Equation 2.1 the

following differential equation is obtained for a homogeneous material with attenuation coefficient μ.

$$\frac{dI}{I(x)} = -\mu dx \tag{2.2}$$

The solution of the differential equation (2.2) is

$$I(x) = I_0 e^{-\mu x} \tag{2.3}$$

The signal-to-noise ratio (SNR) in the image can be defined as

$$SNR = \sqrt{\bar{n}} \frac{|I_f - I_b|}{\sqrt{I_f + I_b}}, \tag{2.4}$$

where I_f is the foreground intensity, I_b is the background intensity, and $\bar{n}$ is the average number of photons hitting the feature [11]. Therefore, the quality of the projections depends on the intensity difference between the foreground and background, the number of photons in the beam, and the exposure time. The quality of synchrotron light is often measured in brightness, which considers the number of photons produced per Second, the cross-sectional area of the beam, the beams angular divergence and the photons falling within a 0.1% bandwidth of a given wavelength, see Figure 2.4. The brightness of synchrotron light sources is several magnitudes higher than conventional X-ray sources, allowing X-ray projections to be acquired with shorter exposure times at the same SNR.

There are many differences between the beamlines in a synchrotron. For the sperm experiments, the TOMCAT beamline at Swiss Light Source (SLS) was chosen. See Figure 2.5 for an overview of the Swiss Light Source, SLS and its beamlines. The TOMCAT Nanoscope has the field of view, 75 μm, able to capture a whole sperm and a 65 nm effective pixel size, which is suitable for sperm imaging.

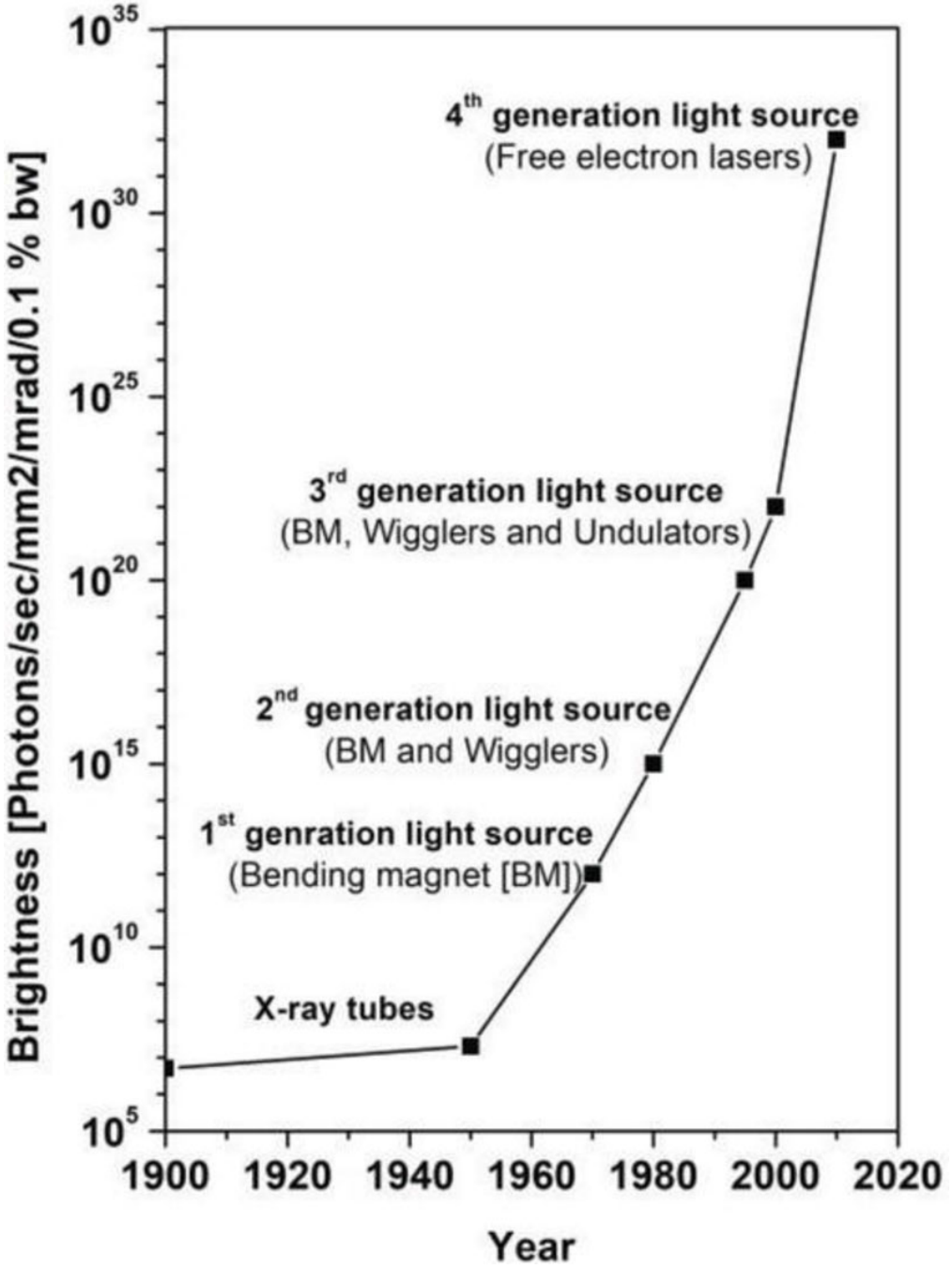

Figure 2.4.: **Brightness of X-rays**. The main quality difference between X-ray sources is the brightness. SLS is a third-generation synchrotron light source, hence the brightness is much higher than that obtained in a laboratory micro-CT based on X-ray tubes. The image is from `https://www.intechopen.com/chapters/65550`.

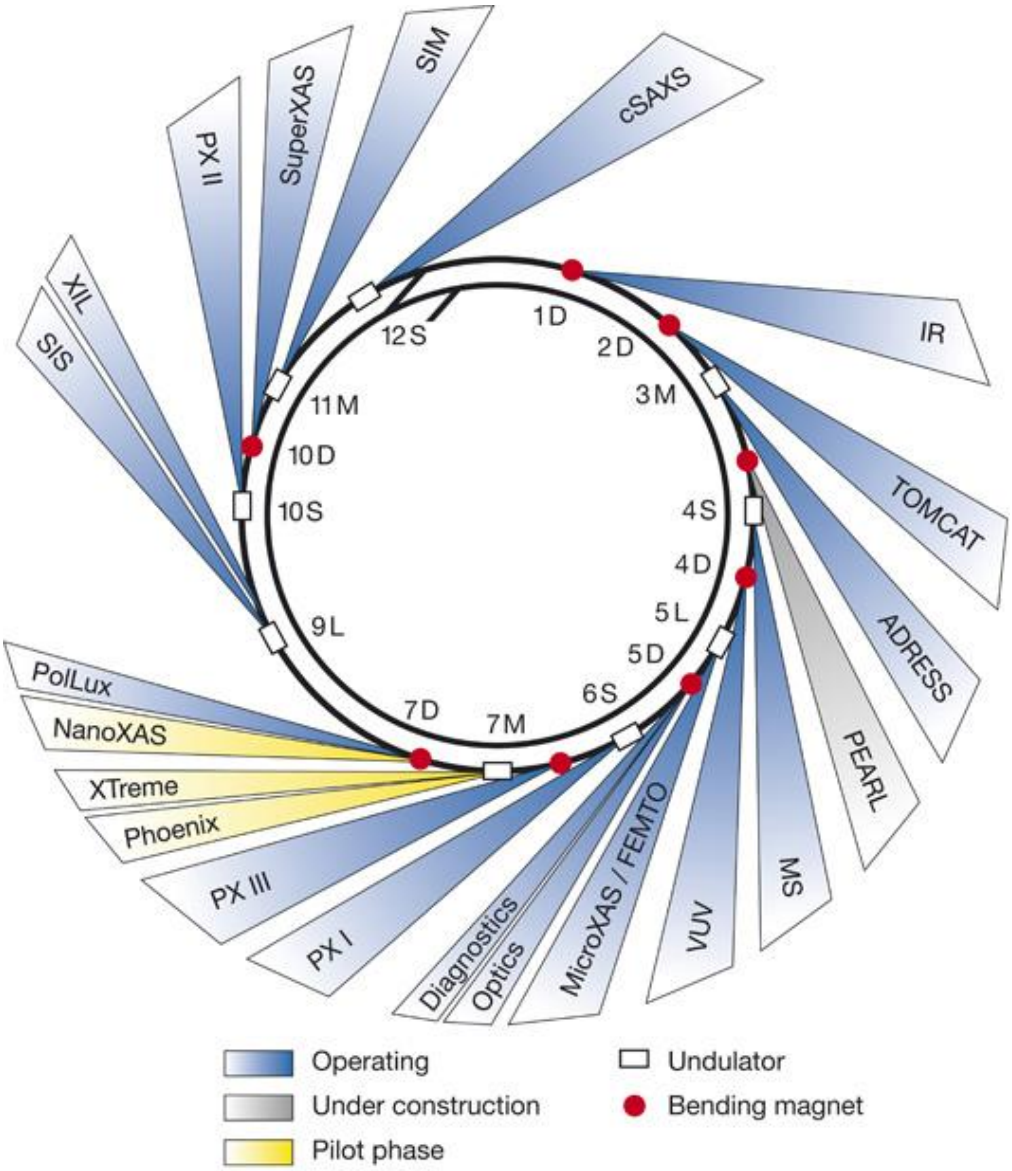

Figure 2.5.: SLS beamlines. The illustration shows the beamline layout of the Swiss Light Source. TOMCAT, used for the sperm experiments, can be seen on the right. The linear accelerator, shown as a black line inside the ring on the top, accelerates the electrons and feeds them into the inner booster ring. The booster ring accelerates the electrons to the desired speed, and the outer storage ring stores the electrons, using magnets and undulators to steer the beam and generate X-rays. At the endstation, optics condition the X-rays to optimize the beam for a specific application. The image is from `https://www.psi.ch/en/sls/about-sls`

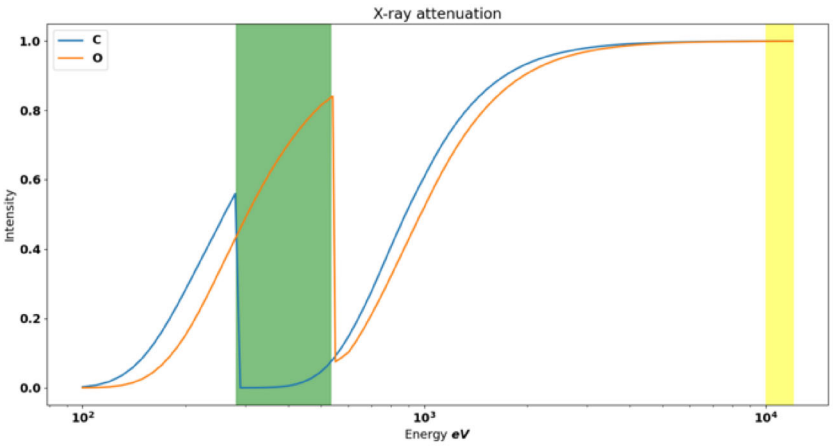

Figure 2.6.: Attenuation of Carbon and Oxygen. Attenuation of x-rays through 1 μm of different materials. The water-window is shaded in green, the energy range of the TOMCAT beamline is shaded in yellow. The x-axis is logarithmic. The python library XrayDB `https://xraypy.github.io/XrayDB/python.html` was used to obatin the data for the graphs.

Unfortunately, sperm and the aqueous environment in which they thrive have very similar X-ray attenuation coefficients at the energies in which the TOMCAT beamline operates (8 keV to 20 keV). Good X-ray contrast from sperms on a water background is found in a unique spectral region called the *water window*, see Figure 2.6, which lies between discontinuities in the attenuation coefficient of carbon and oxygen, two dominating components of sperms and water in terms of X-ray attenuation. Unfortunately, it is unlikely that live-cell imaging is possible in the water window due to radiation damage, see Chapter 3. Therefore, several methods were examined for increasing the contrast in the energy range offered at TOMCAT:

Decreasing background intensity Low-density liquids such as paraffin oil have lower attenuation coefficients than water. However, mixing sperms with paraffin oil is not straightforward as the cells are already in a watery buffer and can not easily be caught and dried while still keeping them alive. Furthermore, it is unlikely that the sperms would swim naturally in paraffin oil.

Inverse contrast from gadolinium and Iodine Gadolinium and Iodine based drugs are frequently used for X-ray contrast in, for example, angiography. The drugs increase the attenuation of the watery blood and could also

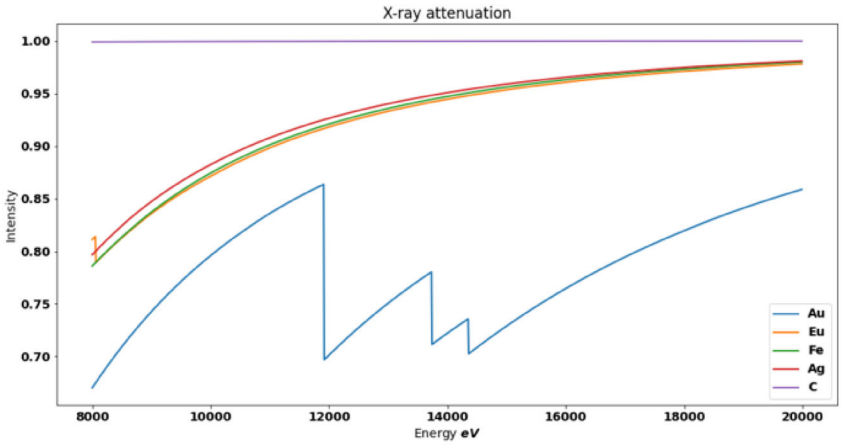

Figure 2.7.: Attenuation of materials considered for enhanced contrast. Attenuation of x-rays through 1 μm of different materials. The energy range matches that of the TOMCAT beamline. All materials are more attenuative than carbon. Gold has a number of discontinues jumps in the profile, a very large jump around 12 keV and two at higher energies. Europium also has a discontinuity just above 8 keV. The python library XrayDB `https://xraypy.github.io/XrayDB/python.html` was used to obatin the data for the graphs.

increase the attenuation of the fluid surrounding the sperms. Some tests were performed at the TOMCAT nanoscope, but no promising results were obtained. The contrast agents did not mix well with the buffer, resulting in areas with too much absorption and areas with no contrast effect.

Phase Contrast The Lambert-Beer law describes how the amplitude of the X-rays changes as they pass through matter. When waves pass through matter, both the amplitude and the phase are altered; this can be exploited in phase-contrast imaging. The TOMCAT nanoscope uses Zernike phase contrast [35]. However, even with phase contrast, the sperm were not visible.

Sample preparation The quality of the tomographic scan is highly dependent on the sample preparation. Samples prepared for the TOMCAT Nanoscope should preferably have a diameter that fits within the field of view of 75 μm. At the end of this chapter, a cheap, portable setup is proposed for isolating sperm and containing them within the field of view is proposed.

Osmium Some of the sperm samples were labelled using Osmium. Osmium is highly toxic and would kill the cells, but the labelling allowed static 3D imaging to determine how low an exposure time could be used with well-labelled cells. The results are described in the following article.

Nanoparticles Nanoparticles can be used for X-ray contrast, and Gold, Silver, Europium, and Iron-based nanoparticles were considered as these have previously been shown to enter sperms [36, 22, 5]. All these elements have increased attenuation compared to carbon, see Figure 2.7. Interestingly attenuation coefficients are not continuous as a function of energy but have discontinuities at specific energies. The discontinuities can be used to advantage in multi-energy setups [37]. An improved contrast can be obtained by taking the difference between a projection acquired above the discontinuity and below. Both Gold and Europium have discontinuities within the energy range of the TOMCAT beamline, and it could warrant further research on whether a dual-energy approach is possible to increase contrast. In terms of contrast, gold would be the best choice, but gold nanoparticles have been shown to affect sperm motility [41] adversely. Iron oxide nanoparticles were chosen as the final contrast method, as they were found to be the least likely to alter the sperms swimming pattern. The results are written in the following article.

Iron Oxide Nanoparticles as a Contrast Agent for Synchrotron Imaging of Sperm Cells

Mette Bjerg Lindhøj[1,2,*], Susan Rudd Cooper[3], Andy S. Anker[3], Anne Bonnin[4], Mie Kristensen[5], Klaus Qvortrup[6], Kristian Almstrup[7], Kirsten M. Ø. Jensen[3], Tim B. Dyrby[2,8], and Jon Sporring[1]

[1]Department of Computer Science, University of Copenhagen, Copenhagen, Denmark.
[2]Danish Research Centre for Magnetic Resonance, Center for Functional and Diagnostic Imaging and Research, Copenhagen University Hospital Hvidovre, Hvidovre, Denmark.
[3]Department of Chemistry and Nano-Science Center, University of Copenhagen, Copenhagen, Denmark.
[4]Paul Scherrer Institut, Villigen PSI, Switzerland.
[5]Department of Pharmacy, University of Copenhagen, Copenhagen, Denmark.
[6]Core Facility for Integrated Microscopy, University of Copenhagen, Copenhagen, Denmark.
[7]Department of Growth and Reproduction, Copenhagen University Hospital - Rigshospitalet, Copenhagen, Denmark.
[8]Department of Applied Mathematics and Computer Science Technical University of Denmark, Kongens Lyngby Denmark.
[*]memo@di.ku.dk

Abstract

Fast phase-contrast imaging offered by modern synchrotron facilities opens the possibility of imaging dynamic processes of biological

material such as cells. Cells are mainly composed of carbon and hydrogen, which have low X-ray attenuation, making cell studies with X-ray tomography challenging. At specific low energies, cells provide contrast, but cryo-conditions are required to protect the sample from radiation damage. Thus, non-toxic labelling methods are needed to prepare living cells for X-ray tomography at higher energies. We propose using iron oxide nanoparticles due to their proven compatibility in other biomedical applications. We show how to synthesize and attach iron oxide nanoparticles and demonstrate that cell-penetrating peptides facilitate iron oxide nanoparticle uptake into sperm cells. We show results from the TOMCAT Nanoscope (Swiss Light Source), showing that iron oxide nanoparticles allow the heads and midpiece of fixed sperm samples to be reconstructed from X-ray projections taken at 10 keV.

1 Introduction

Synchrotron X-ray tomography (SXRT) is a vital tool in scientific research of biological samples offering insight into diverse domains such as axon and muscle fibre morphology (1, 2) and the biomechanics of insects (3–5). Combining the spatial resolution to view axons with the temporal resolution needed to see the dynamics of a blowfly offers excellent possibilities for studying the biomechanics of single cells.

Achieving dynamic tomography of single cells is dependent on two essential factors: High spatio-temporal resolution and high sample contrast at a low absorbed dose.

The recent development of brilliant synchrotron light sources and fast detector systems have made it possible to capture much faster motion and a wider range of sizes than ever seen before (6). Within the last decade, the effective pixel size has been pushed to the micro-and nanometer scale with sub-second exposure times (3, 6–14).

Mammalian sperm cells are very suitable candidates for probing the limits of SXRT for dynamic single-cell imaging as these are primary mammalian cells readily available and among the most dynamic cells known. Furthermore, changes in sperm motility caused by environmental chemicals acting on CatSper, the primary calcium channel of sperm cells, has been proposed to be a potential mechanism involved in recent decreasing fertility trends (15, 16). Dynamic single-cell studies of sperm cells is highly relevant for understanding parameters important for fertility.

The image intensity value in an X-ray projection comes mainly from a reduction of the intensity of the X-ray beam as it passes through the material,

known as attenuation. The attenuation is caused by absorption or scattering of the beam and is affected by factors such as the atomic properties of the material and the beam energy. At most energies, cells and water-like substances, such as cell media needed for cells to survive, have very similar attenuation properties. This makes SXRT of living cells challenging as they provide almost no X-ray contrast against their surroundings. The water window is a unique spectral region where the attenuation difference between carbon and oxygen is especially large (17), allowing cells to be clearly distinguished from a water background (18). However, the increased absorption also increases the radiation dose deposited in the cells. Therefore, vitrification of the sample is required to protect the sample from radiation damage during X-ray tomography in the water window, making the study of living cell dynamics impossible.

Different materials can be added to cells to achieve sufficient contrast in X-ray imaging at higher energies where the absorbed dose is less. One such method is the addition of electron-dense osmium tetroxide to myelin for enhanced contrast of axons (1). While osmium also provides good contrast in sperm cells, it is highly toxic, making it unfit for living cells. Other known contrast agents for X-ray imaging are iodine or gadolinium-based drugs, used for contrast enhancement during, e.g., angiography (19, 20) in medical CT scans. Gold nanoparticles can also provide contrast enhancement during X-ray imaging (21–23). Unfortunately, gold nanoparticles have adverse effects on the motility of sperm cells, leaving approximately one-quarter of the cells immotile after treatment (24).

Iron oxide nanoparticles are widely used in biomedicine due to their high biocompatibility and magnetic properties. Furthermore, they enter sperm cells through endocytosis without affecting their motility or ability to fertilize an egg (25). Iron oxide attenuates the beam more than cells, making it a promising candidate for enhanced contrast in SXRT of biological samples such as sperm cells.

When using nanoparticles for contrast enhancement during SXRT, the number of particles taken up by the cell, and their ability to distribute throughout the cell, are essential to provide sufficient contrast. To aid the uptake of the nanoparticles, cell-penetrating peptides (CPP), such as Penetratin, can be used (26). CPPs comprise a family of short peptides (up to approximately 30 amino acids), which inherently permeates cell membranes. Several CPPs, including Penetratin, are classified as cationic/amphipathic (27). They internalize into cells via direct membrane translocation or endocytosis and have demonstrated the ability to facilitate uptake of co-incubated cargo such as nanoparticles into various cell types (28). Penetratin has earlier demonstrated efficient internalization into

sperm cells without compromising their cell viability or motility (29).

Our study aims to determine whether iron oxide nanoparticles can be used as a contrast agent for high energy synchrotron X-ray tomography of living sperm cells. To this end, we performed experiments to investigate whether we could reach the spatial and temporal resolution needed to image live sperm cells with SXRT and whether iron oxide nanoparticles could be used as a non-toxic alternative to existing staining methods. To develop the staining method, we synthesized iron oxide nanoparticles covered in polyvinyl alcohol and incubated them with boar sperm cells, using Penetratin to facilitate the uptake. We used transmission electron microscopy to verify the attachment of the nanoparticles to the sperm cells and obtained SXRT volumes of fixed sperm cells stained with iron oxide nanoparticles at the TOMCAT beamline (Swiss Light Source (SLS)) to assess the success of the staining.

2 Results

2.1 Millisecond exposure times and nanometer resolution are possible using osmium staining

To ascertain whether we could reach a high enough spatio-temporal resolution to view a moving sperm cell, we did a speed test at the TOMCAT beamline at SLS. We used fixed sperm cells stained with 2% osmium for the speed test; see Materials and Methods. We tested exposure times ranging from 200 ms to 20 ms pr. projection. The noise in the reconstruction increased as exposure time decreased, which is to be expected, see Figure 1(A, C). However, even at a 20 ms exposure time, it was still possible to segment the cell shown in Figure 1(B), including a good portion of the tail. The tail in the given segmentation was measured to be 35 µm long and was cut off at the edge of the field of view. Human cells, used during this test, have a tail length of approximately 50 µm. Thus, more than half the tail was visible. Other cells in the 20 ms segmentation were more affected by the increased noise level, probably due to slightly less staining. We achieved the tomographic acquisition of fixed sperm cells with 65 nm effective pixel size and using 500 projections at 50 projections per second (pps).

2.2 The synthesized nanoparticles consisted of a magnetite core coated in PVA

To make the non-toxic iron oxide nanoparticle contrast agent for the sperm cells, we synthesized iron oxide nanoparticles coated in polyvinyl alcohol

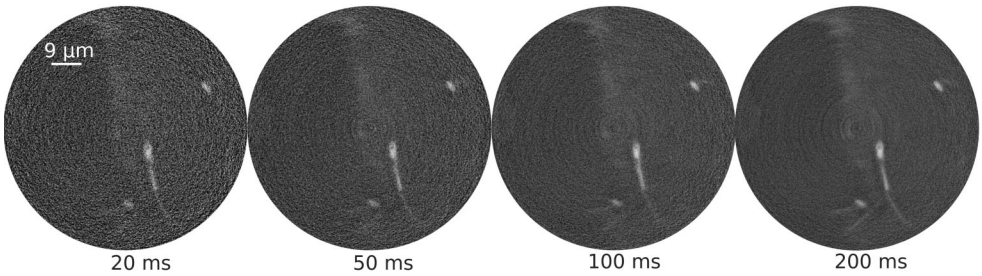

A Reconstruction slices

B Segmented cell

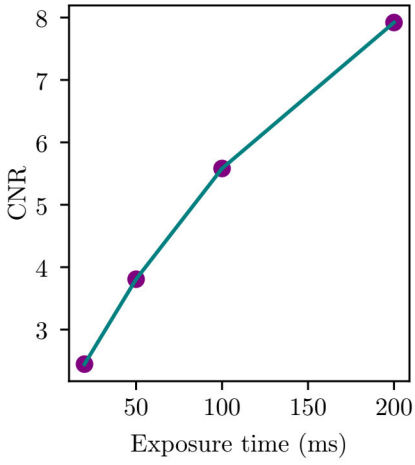

C CNR vs. exposure time

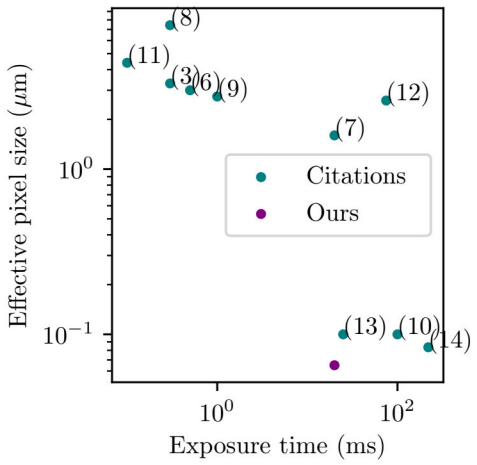

D Pixel size vs. exposure time

Fig. 1. Speed test results. To perform the speed test we varied exposure times from 20 ms to 200 ms. Lower exposure times resulted in more noise as expected (**A** and **C**). However, from the segmentations (**B**) it is clear that even though noise is increasing it has very little effect on the segmentation when the sperm cell is adequately stained. The plot (**D**) shows the effective pixel size vs. exposure times as reported in different publications. If more than one combination is reported, we picked the one closest to ours. The point labels are the citation numbers. The purple dot is our results. Both axis are logarithmic.

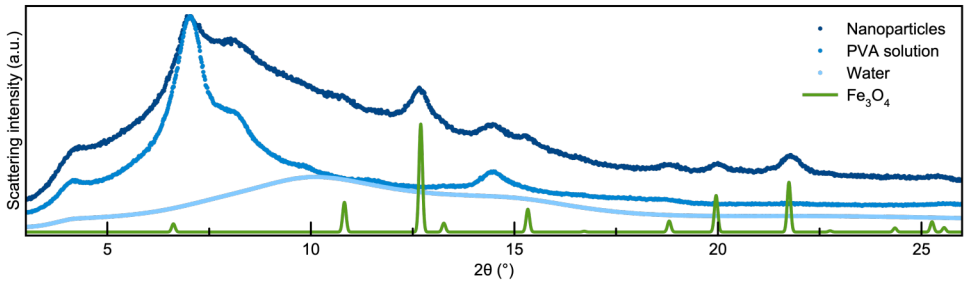

Fig. 2. PXRD analysis. The graph shows a comparison of PXRD data of the solid nanoparticles before being thoroughly dried (dark blue), a PVA solution (medium blue), water (light blue), and a calculated scattering pattern of a published magnetite structure (green) (30). The data are collected by measuring the scattering intensity at different scattering angles (2θ). The peaks from the scattering pattern of our synthesized nanoparticles (dark blue) coincide with the peaks from the PVA and iron oxide scattering patterns (medium blue and green) and are not present in the water background, indicating that the particles are iron oxide nanoparticles covered in PVA.

(PVA) by modifying a previously reported co-precipitation method (31), see Materials and Methods. Then, to verify the method's success, we used Powder X-ray diffraction (PXRD) to estimate the size of the particles and verify their crystal structure. Powder X-ray Diffraction (PXRD) is used to identify and characterize the structure of crystalline materials. The PXRD peaks contain information on the atomic arrangement in materials.

Figure 2 shows the X-ray diffraction pattern of the nanoparticles compared to the calculated X-ray scattering patterns of magnetite (30).The X-ray scattering pattern from the nanoparticle suspension shows Bragg reflections (peaks) at values of 2θ equal to 12.7°, 15.3°, 18.8°, 20.0° and 21.8°, which are also in the calculated magnetite pattern. In addition, in the X-ray scattering pattern from the nanoparticle suspension, we see large, broad peaks centred at 2θ equal to 7.0°, 8.0° and a peak at 2θ equal to 14.5°, which are also present in the X-ray scattering pattern from the PVA solution, but not in the X-ray scattering pattern from the water background. This suggests that PVA is in the particle suspension, and we expect it to cover the surface of the nanoparticles. Using the Scherrer equation, equation (1) in Materials and Methods, we estimated the crystallite size of the particles to be approximately 6 nm in diameter. Conclusively, PXRD analysis confirms that iron oxide nanoparticles with a size of approx. 6 nm have been synthesized, and that they are most likely covered by PVA. Combined with the small size of the particles, they seem to be a promising candidate for an X-ray contrast

agent.

2.3 The nanoparticles had entered the cells

To stain the sperm cells with the iron oxide nanoparticles, we incubated a density gradient purified sperm sample with a suspension of the synthesized nanoparticles. The nanoparticles were incubated with the sperm cells using Penetratin to aid the uptake of the particles; see Materials and Methods. Then, the sperm samples were fixed and imaged with transmission electron microscopy (TEM) to verify that the particles had entered the sperm cells. The TEM images verified that the electron-dense magnetite nanoparticles had entered the cells (Figure 3). We determined the location of the particles to be inside the heads, midpieces and tails of the cells by investigating the texture of the cells in the EM-images. Traces of particles outside the cells were also observed.

2.4 Heads and midpieces can be segmented from the synchrotron data

To assess the success of our contrast method, we performed SXRT of fixed sperm cells stained with nanoparticles and segmented the volumes. We used morphological measurements of the sperm cells and compared them to our segmentations.

We used boar sperm cells of the Duroc breed to conduct our experiment as they are more robust for storage and transportation and more readily available in large amounts than the human cells used for the speed test.

Typical sperm cells, as illustrated in Figure 4(A), consists of a head, a midpiece, and a tail. The sperm cells of the Duroc boar that we used have been reported to have a flat oval head $9.4 \pm 0.3\,\mu m$ by $4.8 \pm 0.2\,\mu m$ and a tail $43.7 \pm 1.2\,\mu m$ long (32). To estimate the midpiece and tail morphology, we acquired a 3D TEM image stack of a Duroc sperm pellet and segmented it. From these segmentations, we estimate that the midpiece is about $11.0 \pm 0.1\,\mu m$ long and $0.9 \pm 0.1\,\mu m$ wide. We estimate that the tail is approximately 500 nm in diameter at its widest place shortly after the neck and that the tail slowly decreases in width towards the tip to approximately 300 nm in diameter. These measurements are consistent with the sperm morphology measures on domestic pigs in (33).

We chose to conduct our experiments at the TOMCAT Nanoscope (SLS), as it has a $75\,\mu m$ field of view, large enough to capture a whole cell and a 65 nm effective pixel size high enough to capture the tail. The samples we

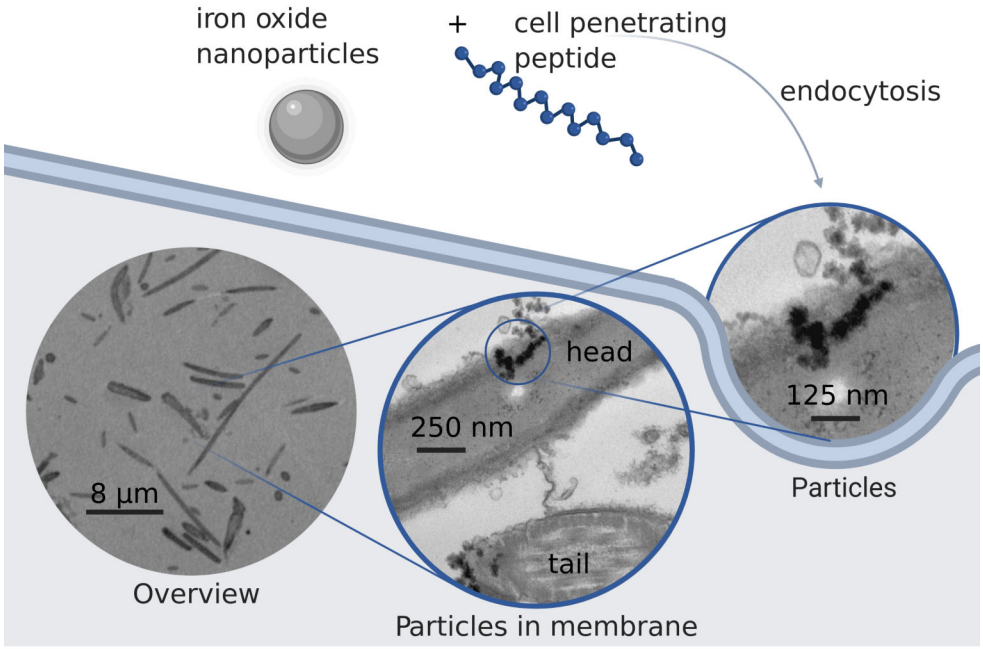

Fig. 3. TEM images of cells stained with nanoparticles. The figure illustrates how we believe the incubation worked. By incubating the sperm cells with iron oxide nanoparticles and Penetratin, the iron oxide nanoparticles internalized into the cell membrane (blue line). The three circular images are selected regions of TEM images at differing scales. On the left is an overview of the sample, showing that the sperm cells are relatively close together, which is a possible cause for our inability to segment the tails in the synchrotron volumes. In the centre circle, the particle placement is shown. The particles were found both in the heads and tails as labelled in the image. The placement was determined by the texture of the image. On the right, we show a close up of the particles, where we see that several particles group together, forming lumps.

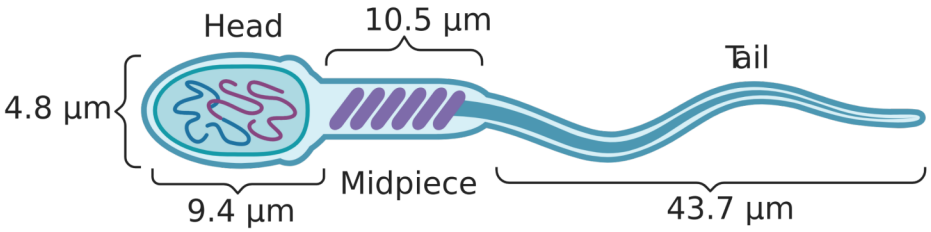

A Typical duroc cell

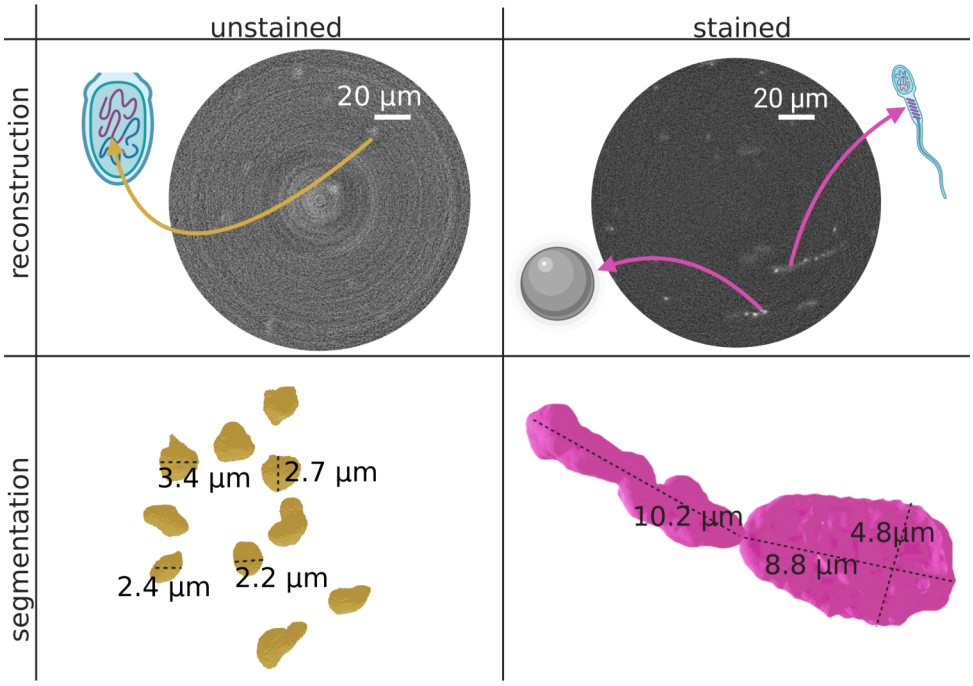

B Synchrotron reconstructions and segmentations

Fig. 4. Synchrotron results. **A**: An illustration of a Duroc sperm cell with relevant mean measures. **B**: A tabular illustration showing the differences between unstained sperm cells (left column) and sperm cells stained with iron oxide nanoparticles (right column). In the unstained sample (left column) we weren't able to find any shapes reminiscent of sperm cells, only blobs we believe to be dense DNA inside the sperm heads. When the sperm cells were stained (right column) with our iron oxide nanoparticles the heads and midpieces could be segmented, which was verified by comparing the measures in the segmentation with the known morphological measurements of Duroc sperm cells (**A**).

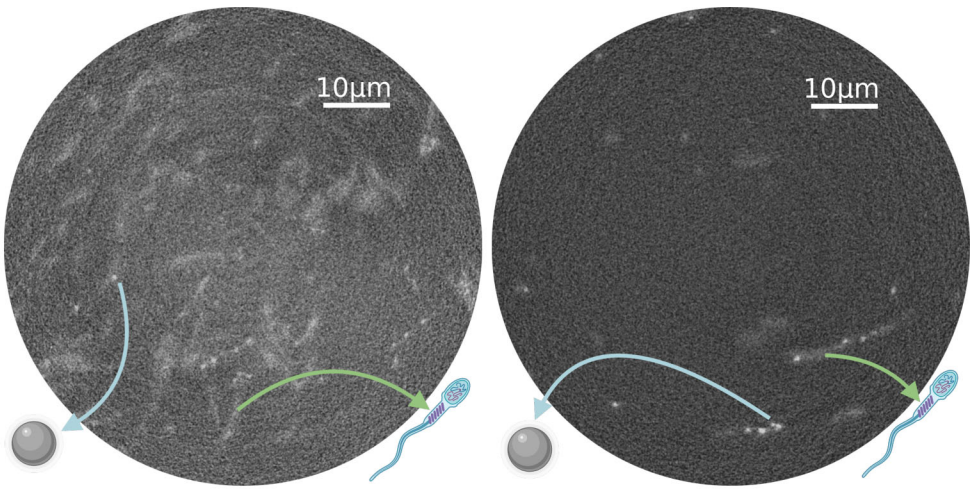

A No CPP used **B** Penetratin

Fig. 5. Effect of penetratin. A: The reconstruction slice from a sample stained with nanoparticles without the use of any CPP. **B** The reconstruction of a slice from a sample coincubated with iron oxide nanoparticles and Penetratin. While the staining without using Penetratin was improved compared to an unstained sample the contrast with Penetratin to aid the uptake was better and allowed clear heads and midpieces of the sperm cells to be segmented.

Sample	Particle-to-cell ratio (PCR)	Cell-to-background ratio (CBR)
2	0.0006	0.017
3	0.0060	0.023

Table 1. Differences between using Penetratin and no CPP. The table shows a comparison of the PCR and CBR between sample 3, where we used Penetratin to aid the uptake of the iron oxide nanoparticles and sample 2, where no CPP was used to facilitate the uptake. While the PCR is similar in both samples, the results indicate that Penetratin made a big difference as the PCR is an order of magnitude greater in sample 3. This is further implied by the contrast difference between the two samples seen in Figure 5.

tested were all fixed Epon embedded samples as these are easier to work with than living hydrated samples. The density of water and Epon are both close to 1 g/ml, making the attenuation enhancement determined by the Epon samples comparable to what we would gain in a fluid sample.

We tested four samples at the synchrotron:

1. Unstained cells.
2. Cells that had been incubated with magnetite nanoparticles without the use of Penetratin.
3. Cells that had been incubated with magnetite nanoparticles using Penetratin to aid the uptake.
4. Cells stained with osmium.

In sample 1, Figure 4(B), we were able to identify blob-like structures 2 µm to 3 µm in diameter, which we believe are dense DNA inside the sperm cell heads. We could not identify any structures resembling complete sperm cells in this sample.

In sample 2, we were able to identify sperm-like structures vaguely resembling a head and midpiece, suggesting that the particles were taken up by the sperm cells and thereby increase contrast.

In sample 3, we were able to see the head and midpieces of the sperm cells. We detected several bright spots, consistent with enhanced contrast due to nanoparticles, surrounded by very low contrast lighter areas which we believe is the cell tissue. See Table 1 and Figure 5 for a comparison of sample 2 and 3.

We also measured the particle-to-cell ratio (PCR) in the two samples; see Materials and Methods. For sample 2, we measured a PCR of 0.0006, and

for sample 3, we measured a PCR of 0.0060. The cell concentration in the second and third samples was in the same order of magnitude with a cell-to-background ratio (CBR) of 0.017 versus 0.023 in samples 2 and 3 (Table 1). Since the samples' cell density is comparable and sample 3 seems to contain more high contrast areas than sample 2, we believe that Penetratin is aiding the uptake of the nanoparticles.

The segmentation of sample 3 showed oval disc-like structures, with a cylindrical attachment consistent with sperm heads and midpiece. The shape and size of the disc structures are consistent with the expected shape and size of a Duroc sperm head, and the length of the cylindrical attachment matches that of a Duroc midpiece. The results are displayed in Figure 4(B).

The results from samples 2 and 3 suggest that magnetic nanoparticles can be used to enhance the contrast of sperm cells in synchrotron imaging at high energies. By taking advantage of the membrane permeating properties of the CPP Penetratin (26) we were able to increase the uptake of magnetic nanoparticles and thereby the contrast.

We measured the contrast-to-noise ratio (CNR) in the reconstructions of the different samples, see Materials and Methods. For the samples stained with osmium used for the speed test, the CNR ranged from 2.4 to 7.9. The CNR was dependent on the projection speed ranging from 20 ms to 200 ms respectively. See the graph in Figure 1. Osmium is well distributed around the cells and is not present in the surrounding material. Therefore, in the high contrast reconstructions of the osmium samples, we can easily segment the entire cell. In samples 2 and 3, we measured the CNR of the particles to be 8.6 and the CNR of the cells to be between 1 and 1.7. At a 20 ms projection speed, it is therefore unlikely we would be able to see any cell, but likely that the particles would still be visible.

3 Discussion

Achieving dynamic SXRT of sperm cells is a compromise between three factors; spatial resolution, temporal resolution and dose. Our results show that using iron oxide nanoparticles for enhancing contrast in sperm cells during high-energy SXRT is a promising step towards reaching a feasible compromise. We demonstrate this through two main results; a new staining method for high-energy SXRT of sperm cells and showing that it is possible to obtain the required spatial and temporal resolution.

Acquiring X-ray contrast at 10 keV, as we have done, requires labelling of the cells. Several works have shown that it is possible to increase contrast in X-ray projections by adding contrast enhancers such as osmium, gadolinium,

iodine or gold nanoparticles (19–23). We have demonstrated that osmium provides superior contrast enhancement to our proposed method, and other contrast methods might also provide contrast for sperm cells in synchrotron experiments. However, to the best of our knowledge, no other existing contrast method can be used with sperm cells without compromising their motility. We also believe that the staining method could potentially be used to prepare other biological samples for SXRT, where survival of the specimen is important. The synthesis and internalization of iron oxide nanoparticles in sperm cells has previously been demonstrated, (25), but the novelty of our work is demonstrating that by using the CPP Penetratin, it is possible to increase the contrast at high energy SXRT experiments enough to visualize sperm heads and midpieces.

Increasing the energy has the potential to decrease radiation damage to the sample. Two factors are important in lowering radiation damage; time and dose. The absorbed dose is measured as the absorbed energy pr. unit mass and is dependent on the X-ray mass attenuation coefficient of the sample. Higher mass attenuation is directly related to a higher dose (34). The mass attenuation coefficients of soft tissue, similar in composition to sperm cells, decrease as energy increases (35). Hence, obtaining contrast of cells at higher energies is an essential step towards a viable tradeoff between dose and resolution for dynamic SXRT of live cells.

We have shown that at the Nanoscope, TOMCAT beamline at Swiss Light Source (SLS), we can achieve a 65 nm effective pixel size at an exposure time of 20 ms. This is, to our knowledge, the best in terms of exposure time at the needed resolution to be able to see sperm cells (Figure 1(D)). Previous works within the last decade have pushed the limits with regards to obtaining high spatial resolution at low exposure times. Many have achieved very low exposure times (3, 6–8, 11), but with resolutions in the micrometre scale, which is too low to image sperm cells. Others have achieved great spatial resolution but at slightly higher exposure times (7, 10, 12–14). As sperm cells move fast, higher exposure times increase the dose and also decreases the temporal resolution.

The beat cross frequency (BCF) of a sperm cell is defined as the number of times the head crosses the direction of movement. Boar sperm BCF is temperature-dependent, ranging from 15 Hz to 35 Hz as recorded optically with a 75 fps frame rate (36). With adequate staining, we should capture the movement of boar sperm cells at low temperatures with a projection rate of 50 projections per second. This demonstrates that it is possible to find a favourable tradeoff between spatial and temporal resolution in SXRT.

Since our future aim is to reconstruct the dynamic tail-beat of a sperm cell, an open question is whether the particles can also provide contrast in

the tail region. As seen in the EM results in Figure 3, we found areas where several particles had entered the cells together instead of single particles evenly distributed. We observed particles in all regions of the cell, including the tail.

The synchrotron images corroborate the theory that the particles tend to group together inside the cells. The high contrast areas we believe to be the nanoparticles are larger in diameter than a single particle, as the diameter of a single particle (6 nm) is below the resolution of the synchrotron (65 nm). The SXRT volume with stained cells also contains bright spots beside those attached to a head and midpiece, implying that some particles had either not entered the cells or were attached to the tails, which we could not segment. To determine whether the particles provide contrast in the tail region, we would ideally need to image a single cell with nanoparticles internalized devoid of extracellular particles.

The results show the cells to be bloated compared to our TEM segmentation. The bloating is likely due to the smoothing effect of the non-local means filter we used for segmentation combined with the particles not being evenly distributed in the cells. Hence, a bright particle at one side of the midpiece will give a bloated lump in the segmentation, as we see in Figure 4.

The most significant limitation of the method presented in this study is the uneven distribution of iron oxide nanoparticles in the cells. Therefore, it is essential to determine how to get an even distribution of particles inside the cells to improve the method for visualization of sperm cell tail region. Also, the method is not meant as a tool for viewing the inner bio mechanics of the cells, but as a means to gain enough contrast to reconstruct the shape of the cell changing over time in 3D.

In conclusion, iron oxide nanoparticles can be used as a contrast agent in SXRT imaging of sperm cell heads and midpieces without adversely affecting their motility. While the feasibility of our staining method is demonstrated on sperm cells, the method likely applies to many other cells as iron-oxide nanoparticles are widely used because of their low toxicity and biocompatibility. Our results in terms of spatial and temporal resolution also cover most other cells, as most animal and plant cells are 1 µm to 100 µm in diameter and sperm cells are among the most dynamic cells known.

4 Methods and Material

4.1 Nanoparticle synthesis

We synthesized iron oxide nanoparticles by modifying a previously reported co-precipitation method (31). Afterwards, a PVA solution was added to the nanoparticle suspension to incorporate a PVA surface coating (25).

Iron oxide colloids were synthesized by dissolving 2.08 g $FeCl_2 \cdot 4H_2O$ (CAS: 13478-10-9) and 0.80 g $FeCl_3$ (CAS:7705-08-0) into a 25 ml 0.5 M HCl (CAS: 7647-01-0) under an N_2 atmosphere. Next, the acidic Fe salt solution was added dropwise to 25 ml of an aqueous 1.08 M NaOH (CAS: 1310-73-2) solution under stirring. A PVA solution was made by dissolving 2.52 g PVA (CAS: 9002-89-5) in 50 ml deionized (DI) water under stirring for 30 minutes. The PVA solution was then added to the iron oxide suspension and stirred for another 30 minutes. The particles were washed 6 times with DI water, followed by precipitation by centrifugation at 4500 rpm for 20 minutes, to remove NaCl. Precipitated particles were re-dispersed in DI water and sonicated for 30 seconds in between washes.

4.2 PXRD analysis

We collected X-ray diffraction data from the iron oxide particles, the PVA solution, and a water background. Note that the iron oxide particles had not been thoroughly dried before measurements, and a scattering signal from water is therefore expected. The X-ray scattering pattern of magnetite was calculated with CrystalDiffract®: a powder diffraction program for Mac and Windows. CrystalMaker Software Ltd, Oxford, England (www.crystalmaker.com). We used a transmission setup on an Empyrean Series 3 diffractometer from Panalytical with a Scintillation Detector and a AgKα X-ray source. Data from the particles and PVA solution were measured in 1.0 mm borosilicate capillaries, and data from water were measured in a 0.8 mm borosilicate capillary. The size of the magnetite crystallites was estimated with the Scherrer equation (37, 38), Equation 1.

$$L = \frac{K \cdot \lambda}{FWHM \cdot \cos(\theta)} \tag{1}$$

Where K is the Scherrer constant (0.9), γ is the wavelength of X-rays used (0.56 Å), FWHM is the width of the peak at half maximum ($2\theta = 0.52°$) and θ is the angle of the chosen peak ($2\theta = 12.67°$).

4.3 Incubation of cells with nanoparticles

The rinsed magnetic nanoparticles were ground with a mortar to a fine powder and 52 mg was added to 20 ml 4 mM human tubular fluid (HTF) in a 50 ml falcon tube. The suspension was then whirled for a short time at maximum power, heated to approximately 45 °C and sonicated for 30 minutes. This was repeated three times until the particles were nicely dispersed in the liquid.

For our test, we used boar sperm of the Duroc breed. The sperm was cleaned prior to incubation using PureSperm 50[1] to get rid of non-sperm objects which seem to attract the nanoparticles. First, 1 ml of the sample was placed on 2 ml cold PureSperm 50 in a 15 ml falcon tube. Next, we spun the sample at 400 g for 15 minutes at the lowest acceleration and deceleration and carefully removed the top 2 layers and 3/4 of layer three such that approximately 0.5 ml of the cloudy fluid remained above the pellet. We made HTF+ by adding 150 µl sodium pyruvate to 50 ml HTF buffer. The sperm sample was resuspended and diluted with HTF+ until the concentration was $13 \times 10^6\,\mathrm{ml}^{-1}$. We then made a pellet from 1 ml of the rinsed sperm suspension by spinning 10 minutes at 700 rcf and removing the fluid.

Right before incubation, the nanoparticle suspension was filtered in a 0.2 µm filter to get rid of any large aggregates. After filtration we added 15 µl sodium pyruvate per 5 ml of the filtrate and 30 µl Human Serum Albumin (HSA) per 1 ml of the filtrate and vortexed the suspension. Finally, 1.5 ml of the buffer solution containing nanoparticles was added to the sperm pellet and 27 µl Penetratin stock for a final Penetratin concentration of 5 µM.

The sperm cells were incubated at 37 °C for 80 minutes under foil, lightly shaking. The final pellet was created by spinning at 700 rcf for 10 minutes, removing the top and slowly adding 500 µl glutaraldehyde to the pellet for fixation. See Figure 6. Due to the need to filter the nanoparticle suspension, it is not possible to accurately report the final nanoparticle concentration.

[1] PureSperm 50: Mix 3 parts PureSperm 40 (Nidacon, PS40-100) and 1 part PureSperm 80 (Nidacon, PS80-100). E.g 9 ml PureSperm 40 and 3 ml PureSperm 80. Vortex. Store in refrigirator

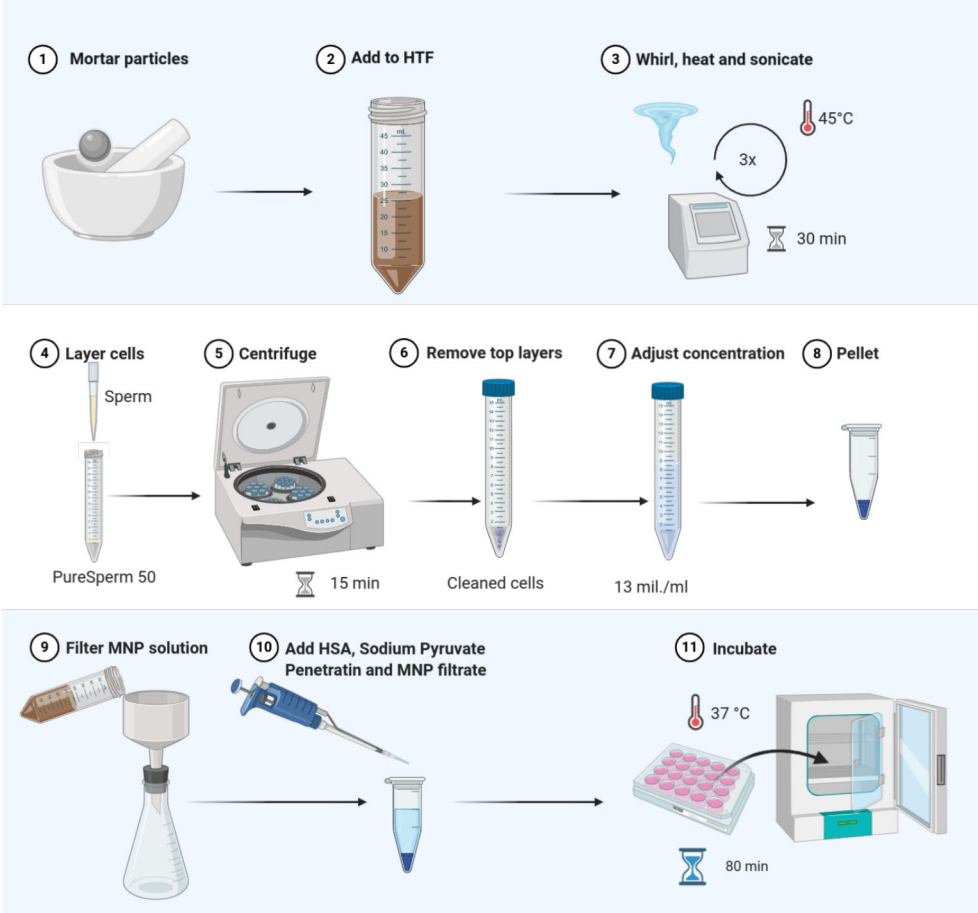

Fig. 6. Overview of the incubation procedure. The first row shows how to disperse the nanoparticles thouroughly in the HTF buffer suitable for sperm cells. The second row shows how to clean the sperm cells to get rid of objects otherwise attracting the iron oxide nanoparticles. The last row shows how to prepare the final incubation fluid and incubate the cells.

4.3.1 EM imaging

Samples were fixed with 2% v/v glutaraldehyde in 0.05 M sodium phosphate buffer (pH 7.2). Following centrifugation, the sample pellets were resuspended and rinsed in 0.15 M sodium cacodylate buffer (pH 7.2) three times. Next, the sample pellets were embedded in low-melting-point Agarose and postfixed in 1% w/v OsO_4 in 0.12 M sodium cacodylate buffer (pH 7.2) for 2 h. The specimens were dehydrated in graded series of ethanol, transferred to propylene oxide and embedded in Epon according to standard procedures. Sections, approximately 60 nm thick, were cut with an Ultracut UCT microtome (Leica, Wienna, Austria) and collected on copper grids with Formvar supporting membranes, stained with uranyl acetate and lead citrate, and subsequently examined with a Philips CM 100 TEM (Philips, Eindhoven, The Netherlands), operated at an accelerating voltage of 80 kV and equipped with an OSIS Veleta digital slow-scan 2k x 2k CCD camera (Olympus, Germany). Digital images were recorded with the ITEM software package.

4.3.2 Synchrotron imaging

The samples were prepared for the Nanoscope experiment by encasing them in EPON blocks, similar to the EM preparation but without any osmium staining. The blocks were then cut into small rods with a Dremel saw, such that the sample was centred in the rod. The rod was then inserted into the Dremel and rotated at minimum or close to minimum speed while carefully sanding the sample using sandpaper with decreasing grain sizes until the sample was below 500 µm in diameter. These samples were imaged using SXRT at the TOMCAT nanoscope at two different energies (10 and 12 keV).

The TOMCAT Nanoscope is a full-field transmission X-ray microscope working from 8 keV to 20 keV. The instrument is composed of a custom-designed beamshaper (39), an order selected aperture (OSA), a fresnel zone plate and corresponding phase rings. The beamshaper having a total diameter of 2975 µm is made of iridium. It has an outermost zone width of 60 nm, a square sub-field size with side of 75 µm and radial periodicity of 75.75 µm between each ring of sub-fields. It produces a top-flat illumination in its focal plane at 1684 mm, at a distance of 18.5 m from the X-ray source at 12 keV or at 1403.4 mm at a distance of 18.85 m from the X-ray source at 10 keV. The OSA was adjusted to keep only the first order of diffraction: the direct beam is stopped by a circular tungsten beamstop with a diameter of 2 mm. The Fresnel Zone Plate (FZP) acts as an objective lens. At 12 keV, we choose a zone plate in iridium with a diameter of 170.5 µm and a focal length of 99 mm. At 10 keV, we choose a zone plate in iridium with a diameter of

204.6 µm and a focal length of 99 mm. In order to exploit phase contrast, Zernike phase rings are placed at the back-focal plane of the FZP. Projections of the sample are collected onto the detector, consisting of a Gadox scintillator screen, optical coupling fibres, and an sCMOS sensor (customized PCO Edge 4.2 by Rigaku) situated about 10 m after the sample.

For the speed test, Figure 1, we used an energy of 12 keV to take advantage of the maximum efficiency of the setup. We collected 501 projections over 180 degrees, associated with two series of 50 flats and one series of 20 darks. Exposure time was set to 200 ms, 100 ms, 50 ms and 20 ms.

For the unstained sample in Figure 4 we used an energy of 12 keV and collected 1500 projections together with 30 darks and two series of 50 flats. For the nanoparticle stained samples in Figure 4 and Figure 5 we decided to decrease the energy to 10 keV to benefit from the higher absorption and therefore increase the contrast in the samples. In this case, we collected 1500 projections over 180 degrees, associated with two series of 100 flats and one series of 20 darks. Exposure time was set to 150 ms. All reconstructions were achieved using the Gridrec reconstruction algorithm as implemented at the beamline (40). 3D datasets generated were saved in 8bits.

4.3.3 Segmentation and ratio measurements

We segmented the cells in the reconstructed volume using scikit-image (41). We first used a sigmoid function to dampen the very high values from the nanoparticles. We then applied a non-local means filter with a patch size of 5, patch distance of 6, a σ of 0.005 and a cut-off distance of 0.5. The volume was then thresholded using a triangle threshold (42). Finally, we found all the connected components and deleted those containing less than 80000 voxels. The threshold of 80000 voxels was determined by visual inspection.

To measure the contrast-to-noise ratio of the reconstructions, we selected pixels belonging to either cells, particles or background. We then used the following formula to determine the CNR:

$$CNR := \frac{\bar{I}_{obj} - \bar{I}_{bg}}{\sigma_{bg}},$$

where $\bar{I}_{obj}$ is the mean intensity of the pixels we have selected for our object (either cell or particles), $\bar{I}_{bg}$ is the mean intensity of the area we have selected as background, and σ_{bg} is the standard deviation of the background intensities.

To measure the particle-to-cell and cell-to-background ratios we first segmented the cells as described above. We then segmented the particles by applying a Gaussian filter with standard deviation $\sigma = 3.0$ and thresholded

the result using a yen threshold (43), which effectively selected the high contrast particle regions but not the cells. The PCR and PBR are then defined as:

$$PCR := \frac{|P \bigcap C|}{|C|},$$
$$CBR := \frac{|C|}{|B|}$$

where P, C and B is the set of voxels classified as particle, cell and background, respectively.

The visual illustrations in the article were created in BioRender.com.

5 Author Contributions

Conceptualization, M.B.L, A.B, T.D, K.A, J.S and M.K; Methodology, S.R.C, A.S.A, K.A, K.Q, and M.B.L; Formal Analysis, M.B.L, S.R.C, and A.S.A; Investigation, M.B.L, S.R.C, A.S.A, K.Q and A.B; Writing - Original Draft, M.B.L, S.R.C, A.S.A, K.Q, A.B, and M.K; Writing - Review & Editing, A.B, T.D, K.A, J.S, M.K, A.S.A, S.R.C, M.B.L, K.Q and K.M.Ø.J; Visualization, M.B.L, A.S.A and S.R.C; Supervision, J.S, T.D and K.M.Ø.J; Funding Acquisition, J.S., T.D. and K.M.Ø.J.

6 Acknowledgement

MBL was supported by the Capital Region Research Foundation (Grant number: A5657) on the MAX4Imagers project (PI: Tim Dyrby).

ASA, SRC and KMØJ are grateful to the Villum Foundation (grant number: VKR00015416) and the Carlsberg Foundation (grant number: CF17-0976) for funding.

We acknowledge the Paul Scherrer Institut, Villigen, Switzerland, for the provision of synchrotron radiation beamtime (20201724) at the beamline TOMCAT of the Swiss Light Source.

References

(1) M. Andersson et al. "Axon morphology is modulated by the local environment and impacts the noninvasive investigation of its structure–function relationship". In: *Proceedings of the National Academy of Sciences* 117.52 (Dec. 2020), pp. 33649–33659. ISSN: 0027-8424.

(2) L. Borg et al. "Muscle fibre morphology and microarchitecture in cerebral palsy patients obtained by 3D synchrotron X-ray computed tomography". In: *Computers in Biology and Medicine* 107 (Apr. 2019), pp. 265–269. ISSN: 00104825.

(3) R. Mokso et al. "Four-dimensional in vivo X-ray microscopy with projection-guided gating". In: *Scientific Reports* 5 (2015), pp. 1–6. ISSN: 20452322.

(4) T. dos Santos Rolo, A. Ershov, T. van de Kamp, and T. Baumbach. "In vivo X-ray cine-tomography for tracking morphological dynamics". In: *Proceedings of the National Academy of Sciences* 111.11 (Mar. 2014), pp. 3921–3926. ISSN: 0027-8424.

(5) S. M. Walker et al. "In Vivo Time-Resolved Microtomography Reveals the Mechanics of the Blowfly Flight Motor". In: *PLoS Biology* 12.3 (2014). ISSN: 15457885.

(6) R. Mokso et al. "GigaFRoST: The gigabit fast readout system for tomography". In: *Journal of Synchrotron Radiation* 24.6 (2017), pp. 1250–1259. ISSN: 16005775.

(7) D. Kazantsev, E. Guo, A. B. Phillion, P. J. Withers, and P. D. Lee. "Model-based iterative reconstruction using higher-order regularization of dynamic synchrotron data". In: *Measurement Science and Technology* 28.9 (2017). ISSN: 13616501.

(8) A. Gonzalez-Tendero et al. "Whole heart detailed and quantitative anatomy, myofibre structure and vasculature from X-ray phase-contrast synchrotron radiation-based micro computed tomography". In: *European Heart Journal - Cardiovascular Imaging* 18.7 (July 2017), pp. 732–741. ISSN: 2047-2404.

(9) J. W. Buurlage et al. "Real-time reconstruction and visualisation towards dynamic feedback control during time-resolved tomography experiments at TOMCAT". In: *Scientific Reports* 9.1 (2019), pp. 1–11. ISSN: 20452322.

(10) A. T. Kuan et al. “Dense neuronal reconstruction through X-ray holographic nano-tomography”. In: *Nature Neuroscience* 23.12 (2020), pp. 1637–1643. ISSN: 15461726.

(11) K. Z. Zefreh, F. M. Welford, and J. Sijbers. “Investigation on the effect of exposure time on scintillator afterglow for ultra-fast tomography acquisition”. In: *Journal of Instrumentation* 11.12 (2016). ISSN: 17480221.

(12) C. Rau et al. “Micro- and nano-tomography at the DIAMOND beamline I13L imaging and coherence”. In: October 2017 (2017), p. 28. ISSN: 1996756X.

(13) J. Villanova et al. “Fast in situ 3D nanoimaging: a new tool for dynamic characterization in materials science”. In: *Materials Today* 20.7 (2017), pp. 354–359. ISSN: 18734103.

(14) S. Flenner et al. “Pushing the temporal resolution in absorption and Zernike phase contrast nanotomography: Enabling fast in situ experiments”. In: *Journal of Synchrotron Radiation* 27 (2020), pp. 1339–1346. ISSN: 16005775.

(15) C. Schiffer et al. “Direct action of endocrine disrupting chemicals on human sperm”. In: *EMBO reports* 15.7 (July 2014), pp. 758–765. ISSN: 1469-221X.

(16) A. Rehfeld et al. “EDC IMPACT: Chemical UV filters can affect human sperm function in a progesterone-like manner”. In: *Endocrine Connections* 7.1 (Jan. 2018), pp. 16–25. ISSN: 2049-3614.

(17) R. Carzaniga, M. C. Domart, L. M. Collinson, and E. Duke. “Cryo-soft X-ray tomography: A journey into the world of the native-state cell”. In: *Protoplasma* 251.2 (2014), pp. 449–458. ISSN: 0033183X.

(18) C. Jacobsen and J. Kirz. “X-ray microscopy with synchrotron radiation”. In: *Nature Structural Biology* 5.8 SUPPL. (1998), pp. 650–653. ISSN: 10728368.

(19) H. S. Thomsen. “Gadolinium- or iodine-based contrast media: which choice?” In: *Acta Radiologica* 55.7 (Sept. 2014). ISSN: 0284-1851.

(20) J. L. Wichmann et al. “Diagnostic accuracy of late iodine-enhancement dual-energy computed tomography for the detection of chronic myocardial infarction compared with late gadolinium-enhancement 3-T magnetic resonance imaging”. In: *Investigative Radiology* 48.12 (2013), pp. 851–856. ISSN: 00209996.

(21) N. Aslan, B. Ceylan, M. M. Koç, and F. Findik. "Metallic nanoparticles as X-Ray computed tomography (CT) contrast agents: A review". In: *Journal of Molecular Structure* 1219 (Nov. 2020), p. 128599. ISSN: 00222860.

(22) C.-C. Chien et al. "Gold nanoparticles as high-resolution X-ray imaging contrast agents for the analysis of tumor-related micro-vasculature". In: *Journal of Nanobiotechnology* 10.1 (2012). ISSN: 1477-3155.

(23) D. P. Cormode and Z. A. Fayad. "Nanoparticle contrast agents for CT: Their potential and the challenges that lie ahead". In: *Imaging in Medicine* 3.3 (2011), pp. 263–266. ISSN: 17555191.

(24) V. Wiwanitkit, A. Sereemaspun, and R. Rojanathanes. "Effect of gold nanoparticles on spermatozoa: the first world report". In: *Fertility and Sterility* 91.1 (Jan. 2009), e7. ISSN: 00150282.

(25) S. B. D. Makhluf, R. Qasem, S. Rubinstein, A. Gedanken, and H. Breitbart. "Loading magnetic nanoparticles into sperm cells does not affect their functionality". In: *Langmuir* 22.23 (2006), pp. 9480–9482. ISSN: 07437463.

(26) D. Derossi, A. Joliot, G. Chassaing, and A. Prochiantz. "The third helix of the Antennapedia homeodomain translocates through biological membranes." In: *Journal of Biological Chemistry* 269.14 (Apr. 1994). ISSN: 00219258.

(27) Pooga Margus and Ü. Langel. "Classes of Cell-Penetrating Peptides". In: *Cell-Penetrating Peptides: Methods and Protocols*. Ed. by Ü. Langel. New York, NY: Springer New York, 2015, pp. 3–28. ISBN: 978-1-4939-2806-4.

(28) A. Jones and E. Sayers. "Cell entry of cell penetrating peptides: Tales of tails wagging dogs". In: *Journal of controlled release : official journal of the Controlled Release Society* 161 (Apr. 2012), pp. 582–591.

(29) S. Jones et al. "Intracellular translocation and differential accumulation of cell-penetrating peptides in bovine spermatozoa: evaluation of efficient delivery vectors that do not compromise human sperm motility". In: *Human Reproduction* 28.7 (July 2013). ISSN: 0268-1161.

(30) M. E. Fleet. "The structure of magnetite: two annealed natural magnetites, Fe3.005O4 and Fe2.96Mg0.04O4". In: *Acta Crystallographica Section C Crystal Structure Communications* 40.9 (Sept. 1984). ISSN: 01082701.

(31) L. Babes, B. Denizot, G. Tanguy, J. J. Le Jeune, and P. Jallet. “Synthesis of Iron Oxide Nanoparticles Used as MRI Contrast Agents: A Parametric Study”. In: *Journal of Colloid and Interface Science* 212.2 (Apr. 1999). ISSN: 00219797.

(32) S. Kondracki, M. Iwanina, A. Wysokińska, and M. Huszno. “Comparative analysis of Duroc and Pietrain boar sperm morphology”. In: *Acta Veterinaria Brno* 81.2 (2012). ISSN: 0001-7213.

(33) N.-H. Gu, W.-L. Zhao, G.-S. Wang, and F. Sun. “Comparative analysis of mammalian sperm ultrastructure reveals relationships between sperm morphology, mitochondrial functions and motility”. In: *Reproductive Biology and Endocrinology* 17.1 (2019), p. 66. ISSN: 1477-7827.

(34) F. Attix. “Introduction To Radiological Physics and”. In: *John Wiley & Sons, Inc* (2004), p. 607.

(35) J. Seibert and J. Boone. “X-Ray Imaging Physics for Nuclear Medicine Technologists. Part 2: X-Ray Interactions and Image Formation”. In: *Journal of nuclear medicine technology* 33 (Apr. 2005), pp. 3–18.

(36) B. de Wagenaar et al. “Spermometer: electrical characterization of single boar sperm motility.” eng. In: *Fertility and sterility* 106.3 (Sept. 2016), pp. 773–780. ISSN: 1556-5653 (Electronic).

(37) P. Scherrer. *Kolloidchemie*. Berlin, Heidelberg: Springer Berlin Heidelberg, 1912, pp. 387–409. ISBN: 978-3-662-33518-5.

(38) J. I. Langford and A. J. C. Wilson. “Scherrer after sixty years: A survey and some new results in the determination of crystallite size”. In: *Journal of Applied Crystallography* 11.2 (Apr. 1978). ISSN: 0021-8898.

(39) K. Jefimovs, J. Vila-Comamala, M. Stampanoni, B. Kaulich, and C. David. “Beam-shaping condenser lenses for full-field transmission X-ray microscopy”. In: *Journal of Synchrotron Radiation* 15.1 (Jan. 2008), pp. 106–108. ISSN: 0909-0495.

(40) E. H. R. Tsai, F. Marone, and M. Guizar-Sicairos. “Gridrec-MS : an algorithm for multi-slice tomography”. In: *Optics Letters* 44.9 (2019), pp. 2181–2184.

(41) S. van der Walt et al. “scikit-image: image processing in Python”. In: *PeerJ* 2 (June 2014). ISSN: 2167-8359.

(42) G. W. Zack, W. E. Rogers, and S. A. Latt. “Automatic measurement of sister chromatid exchange frequency.” In: *Journal of Histochemistry & Cytochemistry* 25.7 (July 1977), pp. 741–753. ISSN: 0022-1554.

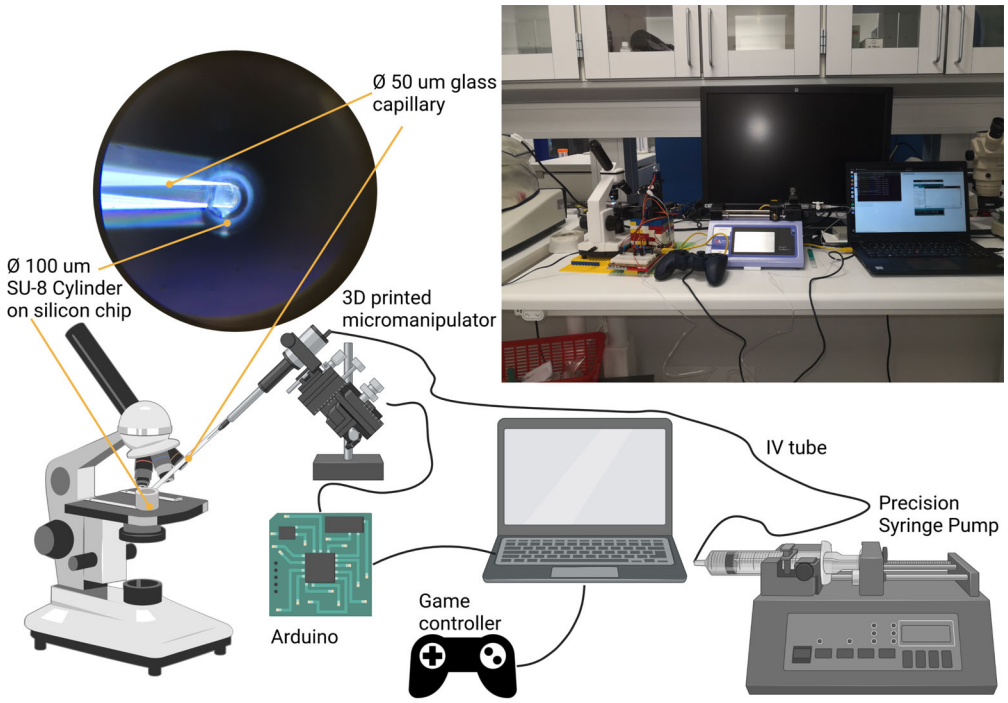

Figure 2.8.: Micromanipulator setup A schematic drawing of the micromanipulator setup with all its components. The figure was created using BioRender.com.

2.1 Experimental setup for single cell live imaging

An essential factor of SXRT quality is sample preparation. For live sperm cell imaging, it would be optimal to capture a single sperm cell within the field of view. However, achieving this posed two significant challenges, obtaining a container small enough to fit within the field of view of the TOMCAT Nanoscope, (75 μm), and getting the cell into the container.

Intracytoplasmic sperm injection (ICSI) systems are used during in vitro fertilization (IVF) to capture single sperm cells and inject them directly into the egg with an ICSI pipette. ICSI pipettes have a diameter smaller than 75 μm. Therefore, capturing a cell with the ICSI system and imaging the cell inside the pipette was initially considered. Unfortunately, preliminary tests showed that the beam causes everything to shift inside the capillary, thus making the cell shift out of the field of view in the vertical direction. The most likely cause of the shift is a slight temperature increase which causes the liquid in the

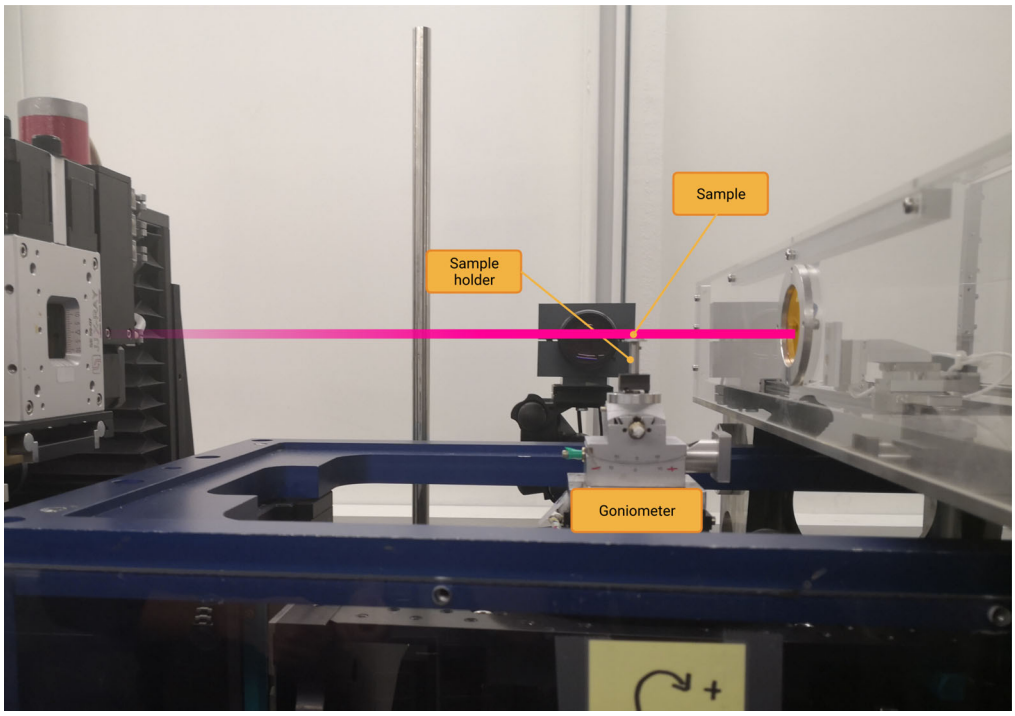

Figure 2.9.: Mounted SU-8 container The SU-8 container was mounted on a goniometer for alignement.

capillary to expand. Furthermore, ICSI systems are expensive and not easily moved to the synchrotron facility.

Containers were custom made at The Danish Technical University, Department of Health Technology Nanoprobes to keep the cells within the field of view in the vertical direction. The containers were made by Lasse Højlund Eklund Thamdrup, a micro and nanofabrication specialist. The containers were made from SU-8 photoresist spun onto a Silicium chip. They had an inner diameter of 98.8(22) μm and a height of 94.60(195) μm and thus almost fit within the field of view.

A small micromanipulation system based on [4] was built, with inspiration from the ICSI system to get the cells into the SU-8 containers. ICSI systems are designed to catch a specific sperm cell that is particularly promising for fertilization. Selecting a specific cell requires a very stable system and highly trained professionals. However, catching a specific sperm cell for the synchrotron application was not the goal, but catching anyone cell would be good enough. Therefore the setup was designed for transportation as it was more critical to prepare fresh samples at the synchrotron facility.

The system consisted of four major components - a microscope, Arduino, 3D printed micromanipulator and a precision syringe pump, see Figure 2.8. The micromanipulator was built based on the specifications given here: `https://open-labware.net/projects/micromanipulator/`, with minor modifications to adjust to the components we had available. The microscope was a standard Byomic Beginners Microscope used for beginner biology exploration. The SU-8 chip was placed on a microscope slide. A 50 μm capillary was attached to the syringe pump through an IV tube. The connection between the capillary and the IV tube was sealed with standard aquarium silicone from a hardware store. The capillary stabilized inside a venflon needle covered with plastic tubing was placed in the micromanipulator. The sperm cells were extracted from a petri dish into the glass capillary using the syringe pump. The capillary was then moved from the petri dish and placed at the edge of the container using the 3D-printed micromanipulator. Finally, the syringe pump was set to inject the cells slowly.

The setup was initially tested using Ø230 μm SU-8 containers. With practice and adjustments of the cells concentration, visual inspection verified that getting a single cell inside the container was possible. However, when the containers were reduced to Ø100 μm, it was evident that the liquid evaporated almost immediately after injection. Hence, a way to quickly seal the container after injection must be found for the setup to be successful.

Another problem with the method was the Silicium chip under the container, which reflected the beam unless the chip was perfectly aligned, so the beam avoided the chip entirely. Aligning the chip was highly time-consuming and challenging as the goniometer used for alignment was manual, and the only way to check the alignment precisely enough was by use of the beam, see Figure 2.9. During alignment, the containers' cells were also exposed to the beam, which is problematic as the dose should be minimized during live experiments.

The setup was promising for catching and containing a single cell for SXRT. However, a way to stop the evaporation must be found, or the liquids in the container evaporate before imaging is possible. Furthermore, the setup should be installed around the beam to achieve alignment before the cells are injected into the container.

Survival

3

Can the sperm survive the beam?

Defining when a cell is dead is not obvious [19], hence for the sake of clarity, the above question needs to be slightly refined. Two sperm events will be considered for analyzing radiation damage, *viability* and *motility*. Non-viable cells will be defined as cells where damage has occurred to the cell membrane. Viability can be measured using propidium iodide, which stains cells with damaged membranes, allowing them to be counted by imaging techniques. Motility refers to the sperms' ability to move.

It is fundamental to explore whether their dynamics are unaffected by the ionizing radiation from a synchrotron beam to determine whether it is possible to do synchrotron imaging of motile sperm. The question is difficult to answer for two reasons.

1. The radiation dose absorbed in a cell is difficult to calculate as it depends on many parameters that can be hard to estimate.

2. The damage caused by the radiation depends not only on the total absorbed dose but also on its effects on the surrounding medium and the time frame of the dose delivery, as the damage occurs at different time scales.

Therefore, an experiment was carried out at the TOMCAT beamline, PSI, to assess the effect of ionizing radiation from a synchrotron on sperm viability and motility. A description of the method and an analysis of the results can be found in the following article.

A Practical Approach to Estimating the Effect of Synchrotron Radiation on Sperm Motility and Viability

Mette Bjerg Lindhøj[1,2,*], Anne Bonnin[3], Kristian Almstrup[4], Tim B. Dyrby[2,5], Rajmund Mokso[6], and Jon Sporring[1]

[1]Department of Computer Science, University of Copenhagen, Copenhagen, Denmark.
[2]Danish Research Centre for Magnetic Resonance, Center for Functional and Diagnostic Imaging and Research, Copenhagen University Hospital Hvidovre, Hvidovre, Denmark.
[5]Department of Applied Mathematics and Computer Science Technical University of Denmark, Kongens Lyngby Denmark.
[4]Department of Health Technology Technical University of Denmark, Kongens Lyngby Denmark.
[3]Paul Scherrer Institut, Villigen PSI, Switzerland.
[4]Department of Growth and Reproduction, Copenhagen University Hospital - Rigshospitalet, Copenhagen, Denmark.
[6]MAX IV Laboratory, Lund University, Lund, Sweden
[*]memo@di.ku.dk

Abstract

Studying the dynamics of sperm tail beating in 3D is important for understanding decreasing fertility trends related to motility. Synchrotron X-ray tomography (SXRT) shows promising results for imaging live biological samples in 3D and time, making it a candidate for imaging sperm tail beating patterns. However, the dose of ionizing radiation (IR) that the cells would receive during image acquisition is of concern as this is likely to affect essential cellular functions. The

effect of IR on motility at the dose rates encountered in a synchrotron has never been assessed. Here, results are presented of analyzing the movement and viability of sperm cells exposed at varying durations at the TOMCAT beamline (Swiss Light Source (SLS)) which has the field of view and spatial resolution needed to reconstruct sperm cells coupled with sub-second exposure times. The results indicate that motility is affected long before viability and that sperm cell dynamics are affected very quickly by the beam.

1 Introduction

According to Abbe's diffraction limit, microscopes can not resolve objects closer than $\frac{\lambda}{2\mathrm{NA}}$, where λ is the wavelength of the light source, and NA is the numerical aperture. This naturally allows electron-and X-ray microscopes to have a higher image resolution than optical microscopes, as these light sources have a much lower wavelength. A shallow depth of field further limits standard optical microscopes whereas, electron and X-ray microscopes have the added advantage of allowing 3D imaging. Recent advances in synchrotron X-ray technology and detector systems have opened the possibility for synchrotron X-ray tomography (SXRT) to be used for dynamic 3D imaging of live biological samples (1), which is unique to this modality. However, successfully imaging live specimens is challenging as it requires simultaneously optimizing image quality on temporal and spatial image resolution at a dose where the sample survives.

Dynamic single-cell studies of sperm cells in 3D are relevant for understanding parameters important for motility. Recent studies have shown that the 3D dynamics reveal motion patterns that cannot be directly observed under a standard optical microscope where only the 2D motion is visible (2). Changes in sperm motility caused by environmental chemicals acting on the primary calcium channel of sperm have been proposed as a mechanism involved in recent decreasing fertility trends (3, 4), and synchrotron imaging is a candidate tool to further study the effect of environmental chemicals on single-sperm motility. Within the last decade, image resolution of SXRT imaging has been pushed to the micro-and nanometer scale with sub-second exposure times (5–14). Hence, it could be feasible to perform SXRT of a sperm cell to analyze the tail beat. However, a fundamental question is whether the cells can survive in the beam and whether the tail beating could be unaffected long enough for the data to be relevant.

Radiation can cause severe damage to living organisms, including oxidation, DNA damage, cell death, inactivation of muscle function and incapac-

itation and death in various insects and small animals (15–23). A previous study coupled dose to image resolution in unlabelled biological samples under cryogenic conditions (24). The study estimated that the dose for unlabelled protein in amorphous ice at a 100 nm image resolution would be close to the dose which is associated with immediate inactivation of muscle function (25) and above the dose where the majority of radiation-resistant bacteria die (18). Typically, SXRT of cells is performed under cryogenic conditions in a unique energy band called the water window, where the contrast of unlabelled cells is optimal, and the damaging effect of reactive oxygen species are minimized. However, labelling could be an option to increase the contrast and allow imaging at higher energies. At higher energies, the attenuation coefficients of soft tissue are lower, decreasing the dose absorbed by the sperm. Furthermore, the impact of radiation damage could be different in sperm, bacteria and complex organisms such as insects and mammals. Radiation effects on male fertility have been studied before (26), but only considering the detrimental effects to spermatogenesis during medical radiotherapy.

The damage caused by ionizing radiation is not only a question of the total dose delivered. The damage takes time to occur, and different types of damage occur at different time scales and do not necessarily end when the exposure stops. Third generation light sources, which produce brilliant X-rays, allow fast imaging by having a very high flux, delivering high doses at a fast rate. Hence, sperm imaged in such a synchrotron would receive a high radiation dose, but whether they would be motile long enough to capture the natural tail beating pattern remains an open question. Additionally, sperm is an exciting subject for probing the effects of radiation damage on cells as they are among the most dynamic cells and readily available, allowing us to measure changes to both viability and motility.

Dynamic single-cell studies pose many practical problems in terms of sample preparation. Catching and containing a single cell within the field of view can be very difficult as perishable live samples must be prepared on-site with available or portable equipment, and these differ between instruments. The experimental method described in this article provides a practical approach to assess the damage caused by a specific beam on a population of sperm and estimate the relative dose on a single-cell sample. The advantage is that the population study is much easier to perform and can therefore be used to probe the feasibility of a single-cell experiment.

2 Methods and Material

To better understand how synchrotron radiation affects sperm, a test was at the TOMCAT beamline (Swiss Light Source (SLS)). A population of sperm were exposed to the X-ray beam while simultaneously monitoring their movement with an optical microscope camera. Subsequently, a NucleoCounter® SP-100™cell counter was used to assess the viability of the sperm. In the following, the experimental setup is explained. Then the analysis of the video data to estimate the effect on sperm motility is presented. Finally, as the experiment should indicate the feasibility of a possible live single-cell experiment, and the dose is not directly comparable, an estimation of the dose relationship between the performed population experiment and a future single-cell experiment is presented. The estimate is based on using the Nanoscope, a full-field transmission X-ray microscope (TXM), where the X-ray beam is focused with optics to obtain the required resolution and field of view for single-cell imaging.

2.1 Mounting a video camera above an exposed sample can be used to assess sperm motility.

A population experiment was performed to assess the effect of the X-ray beam on the sperm. We placed 1 ml of Duroc boar sperm in a Ø 3.5 cm plastic Petri dish. The Petri dish was positioned with laser on a mirror on rotation stage in front of the X-ray beam. Above the dish, we mounted an optical microscope camera, see Figure 1. The mirror increased the light needed to see the cells. The dish was placed so that the X-ray beam would go approximately through the centre of the dish.

We recorded a video with the optical microscope camera, which was left to record before, during, and after X-ray exposure. We performed five experiments at varying X-ray exposure times. The sperm in the five tests were exposed for 1,5,10,15, and 45 minutes. The Petri dish was turned on the rotation stage to expose all cells as evenly as possible during exposure. Immediately after X-ray exposure, we measured the number of dead cells in a NucleoCounter using a membrane-impermeable DNA intercalator, propidium iodide.

The full X-ray beam was used to maximize the number of cells exposed to the beam during the experiment. The Nanoscope X-ray beam, which can be used to image single sperm cells, is focused by optics to obtain the required resolution for single-cell imaging and is therefore different from the beam used for the performed motility test, see Figure 1. The difference affects the dose, which is analyzed below. The full X-ray beam used during the

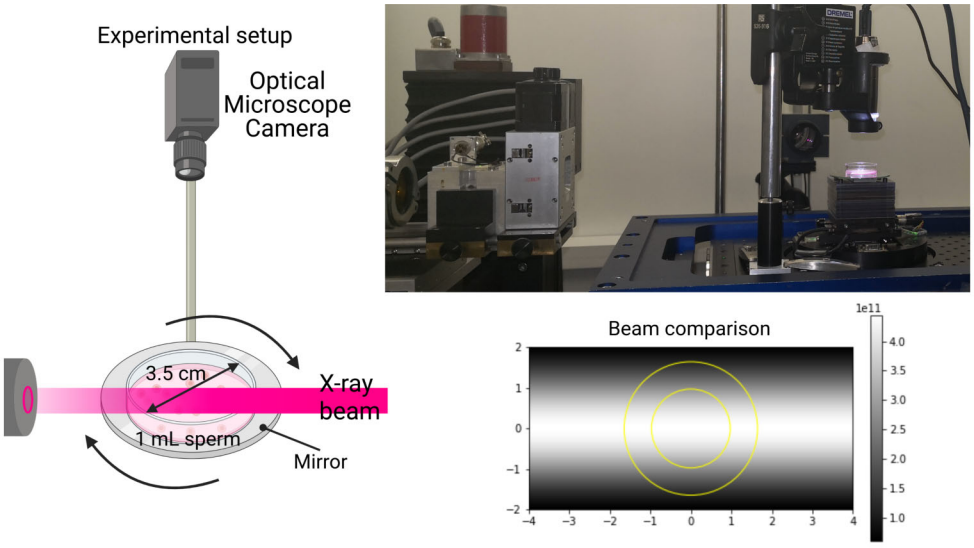

Fig. 1. Experimental Setup On the left is a schematic drawing of the experimental setup with the camera mounted above an Ø3.5 cm petri dish with 1 ml sperm in it. On the top right is a picture of the actual setup. The bottom right is a plot of the X-ray beam model used in the dose calculation. The background image shows the X-ray beam intensity profile as a colour gradient with white being $N_{photons}$ and black being no photons. The yellow doughnut on top is the part of the X-ray beam used by the Nanoscope.

experiment was 8 mm wide and 4 mm high.

A fresh sperm sample was drawn from the same batch during the whole experiment for each test. The tube was gently turned a couple of times before the sample was taken to distribute the cells well. During X-ray exposure, the Petri dish was turned using the rotation stage. Before counting the cells in the cell counter, they were gently mixed with the pipette to disperse them in the liquid uniformly. All measurements were done twice.

The cell counter measured the cell density before and after the experiment. As a control, sperm not exposed to the X-ray beam was used. The control eliminated the possibility that cells were dying due to other factors.

2.2 Entropy and correlation measures between frames can be used to assess the motility in the recorded videos.

The videos recorded during the experiment were analyzed to assess the damage to the motility of the sperm cells. We used two measures; the correlation of the intensity values between frames and the entropy of the pixels in the time direction.

The videos were loaded into python using the *av* library. The videos were in HSV format, and we only considered the last channel. We analyzed 100 frames prior to X-ray exposure and 100 frames after X-ray exposure. The number 100 was chosen because 100 frames were available before and after X-ray exposure in each video. The dimensions of the resulting data blocks were $100 \times 1280 \times 720$ pixels. The resulting blocks were a 3D dataset with two spatial axes and a time axis. The spatial dimensions were flattened to get a 2D matrix with the pixel intensity varying with time through each column. We determined the entropy value within each column using the scikit-image (27) local entropy function with our 2D matrix and a neighbourhood corresponding to a single column. The median of the entropy over all pixels was chosen as the final entropy value. Numpy was used to calculate the Pearson product-moment correlation coefficients between frames.

2.3 The dose relationship between a population experiment and a single-cell setup can be estimated.

The dose relationship between the performed experiment and a future single-cell experiment must be estimated to assess the feasibility. For the estimate, we will use the equation for skin entry dose of (28)

$$D[\mathrm{Gy}] = 10^3 \cdot N \cdot \left(\frac{\mu_{en}}{\rho}\right) h\nu, \tag{1}$$

where D is the skin entry dose, N is the total number of incident photons per cm^2, $\frac{\mu_{en}}{\rho}$ is the mass energy absorption coefficient given in $\mathrm{cm}^2\,\mathrm{g}^{-1}$ which can be obtained from the NIST database (29) and $h\nu$ is the energy of one photon in J.

The terms in (1) will be compared starting from the last term to make a comparison between the skin entry dose in the performed population experiment and the skin entry dose in a future single-cell experiment. The population experiment was performed at 10 keV, which is the same energy that would be used for a future single-cell experiment. Hence $h\nu$ would not change. The term $\left(\frac{\mu_{en}}{\rho}\right)$ is dependent on the material in the sample and therefore would not change. The only difference between the dose in the performed experiment and a future single-cell experiment is N, the total number of incident photons per $1\,\mathrm{cm}^2$. The full X-ray beam was used during the performed population experiment. The Nanoscope X-ray beam would be used for a single-cell experiment. The X-ray beam model for each X-ray beam is displayed in Figure 1.

The number of photons measured at the center of the full X-ray beam is $N_{photons} = 4.4368 \cdot 10^{11}[\mathrm{photons/mm}^2 \cdot \mathrm{s}]$ at 10 keV. The number of photons is not constant throughout the X-ray beam cross-section. In the horizontal direction, the X-ray beam is close to constant; the beam follows a Gaussian curve in the vertical direction. Hence, the following approximation will be used for estimating the number of photons during one second per mm^2, $f(x, y)$, at a point (x, y) in the X-ray beam centered at (0.0), see Figure 1:

$$f(x, y) = N_{photons} \exp\left(-\frac{1}{2}y^2\right). \tag{2}$$

To get the total number of photons $N_{fullbeam}$ in the X-ray beam, an integration of $f(x, y)$ over the total area can be performed

$$N_{fullbeam} = \int_{-2}^{2}\int_{-4}^{4} f(x, y)dxdy \approx 4.45 \cdot 10^{12}. \tag{3}$$

To calculate the number of photons in the Nanoscope beam N_{nano+}, (2) is converted to polar coordinates, the integral over the Nanobeam area is determined

$$N_{nano+} = \int_{0.0}^{D/2.0} \int_{0.0}^{2\pi} N_{photons} \exp\left(-\frac{1}{2}\left(r \cdot \sin(\theta)\right)^2\right) d\theta dr \quad (4)$$

$$- \int_{0.0}^{d/2.0} \int_{0.0}^{2\pi} N_{photons} \exp\left(-\frac{1}{2}\left(r \cdot \sin(\theta)\right)^2\right) d\theta dr \approx 4.34 \cdot 10^{11}, \quad (5)$$

where $D = 3.294$ is the diameter of the outer yellow circle in Figure 1 and $d = 1.946$ is the diameter of the inner circle, both in mm. Furthermore, the Nanoscope uses a condenser which has an efficiency of 20%. Therefore, the total number of photons from the Nanoscope which would reach a single-cell sample is $N_{nano} = 0.2 \cdot 4.34 \cdot 10^{11} = 8.68 \cdot 10^{10}$.

By comparing the two estimates, we can estimate that the total number of photons entering the Petri dish in the performed experiment is approximately 50 times higher than the number of photons that would reach a single-cell sample.

$$\frac{N_{fullbeam}}{N_{nano}} = \frac{4.45 \cdot 10^{12}}{8.68 \cdot 10^{10}} = 51.24 \quad (6)$$

An X-ray beam is attenuated through a volume according to the Lambert-Beer law. The law can estimate the photon count at the centre of the Petri dish.

$$N(z) = Ne^{-\mu z}, \quad (7)$$

where N is the number of photons, z is the position in the direction of the beam in centimetres, and μ is the attenuation coefficient in cm^{-1}. The petri dish is very thick, which means that the dose at the X-ray beams exit point of the petri dish is much lower than the entry point. The number of photons reaching the centre of the Petri dish will be calculated to account for the beam attenuation.

The sperm swim in a buffer with similar attenuation properties to water. The sperm will be approximated by soft tissue in terms of x-ray attenuating properties. According to the NIST database, liquid water has a mass attenuation coefficient of $5.329\,\mathrm{cm}^2\,\mathrm{g}^{-1}$ and soft tissue has a mass attenuation coefficient of $5.379\,\mathrm{cm}^2\,\mathrm{g}^{-1}$ at 10 keV. They are very similar and exhibit similar x-ray attenuation properties. Therefore, the medium will be approximated as a uniform soft tissue mass. The density of soft tissue according to NIST is $1.060\,\mathrm{g\,cm}^{-3}$, giving μ =$5.649\,\mathrm{cm}^{-1}$. Therefore, the number of photons reaching the centre of the dish is much reduced:

$$N_{center} = N(1.75) = N_{fullbeam} e^{(-5.649 \cdot 1.75)} \approx 2.26 \cdot 10^8. \quad (8)$$

A single-cell sample would only be 75 µm in diameter, and therefore the absorption would be close to zero for such a sample. Comparing the above result with the photon count in the Nanoscope beam, it becomes clear that at the centre of the Petri dish, the number of photons is approximately 380 times smaller than the number of photons in the Nanoscope beam:

$$\frac{N_{nano}}{N_{center}} = \frac{8.68 \cdot 10^{10}}{2.40 \cdot 10^{8}} = 383.45 \tag{9}$$

As the sperm were imaged approximately at the centre of the Petri dish, this value is more indicative of the dose relationship. It is important to note that the rotation of the Petri dish affects the radiation dose, and it is not considered here. The calculations presented are meant to serve as a rough estimate.

3 Results

3.1 Viability of sperm at various exposure times showed a significant effect at 45 minutes exposure

We exposed the sperm in the Petri dish for five different durations, 1, 5, 10, 15 and 45 minutes. After the exposure we measured the sperm viability in a NucleoCounter® SP-100™which has an advised measurement range of 0.5 Mio. ml^{-1} to 7.0 Mio. ml^{-1}. At exposure times 1,5,10, and 15 minutes the number of dead sperm did not change significantly and remained below the advised detection limit. The sample subject to 45 minutes of exposure had just above one million dead sperm. As one million is within the advised measurement range and significantly higher than any of the other viability measurements. Hence, we can reliably state that exposure times of 45 minutes damage the sperm membranes. The total number of sperm before exposure was measured with the NucleoCounter to be 20.14 Mio. ml^{-1}. Even after 45 minutes of exposure, only 5 % to 6 % of the sperm were dead.

3.2 Analysing videos of exposed sperm showed decreasing motility with increasing exposure times

Right after exposure, we visually inspected the sample in an optical microscope to assess the sperm's motility damage. The sperm in the 1-minute exposure sample were very active and kept moving even after being left on the counter for a prolonged period. After 5 minutes of exposure, approximately half the sperm were moving, and the sperm motility steadily declined

when left on the counter, indicating that the radiation, in addition to an acute decrease in motility, also had some long term effect on sperm motility. The sperm motility was substantially reduced above five minutes of exposure, and no moving sperm could be found after forty-five minutes.

To quantify these changes more precisely, we analysed five videos of the sperm during each of the five exposure times. The microscope camera, a Dino-Lite AM5018MZTL that we used to record the videos, had a large field of view but a low image resolution. The sperm are seen as small bright spots in the videos[1], and single sperm cannot be distinguished. However, from the videos, it is clear to see the bright flickers of the sperm as they move. The flickering can also be seen by visually inspecting slices in the temporal direction through the video clips, where the sperm appear as bright streaks in the time directions, see Figure 2. Before exposure, all the slices look similar, with the streaks shifting in the spatial direction over time. The streaks gradually appear as more straight vertical lines with minimal shifting in the spatial direction, with increasing exposure times. The increasing uniformity of the streaks indicates less active sperm.

To quantify the sperm motility, we measured the correlation between the frames and the median entropy of all the pixels in the temporal direction, see Figure 3 and Figure 4. The histograms of the correlation values between individual frames in the video clips shift towards higher values after exposure, and the spread of the values decreases, showing that the frames become increasingly correlated after exposure. As exposure time increases, the effect increases, consistent with motility decreasing with increasing exposure time.

The entropy measurement shows that the entropy is similar in all video clips before exposure. After exposure, all entropy values are lower than before exposure, indicating that the pixel intensities are less random in the time directly after exposure. We also see that the entropy decreases with longer exposures, meaning less overall flickering of the pixel values for higher exposures. When fitting a linear model to the entropy values after exposure, we obtain an $r - value$ of -0.91. The intercept of the linear fit is 0.03, which is close to the median entropy value of all videos before exposure, as expected.

[1]The videos can be found here: `https://data.mendeley.com/datasets/kkszwvx7gk/draft?a=a6a070ec-f148-4fc0-8198-6c0ad3435e95`.

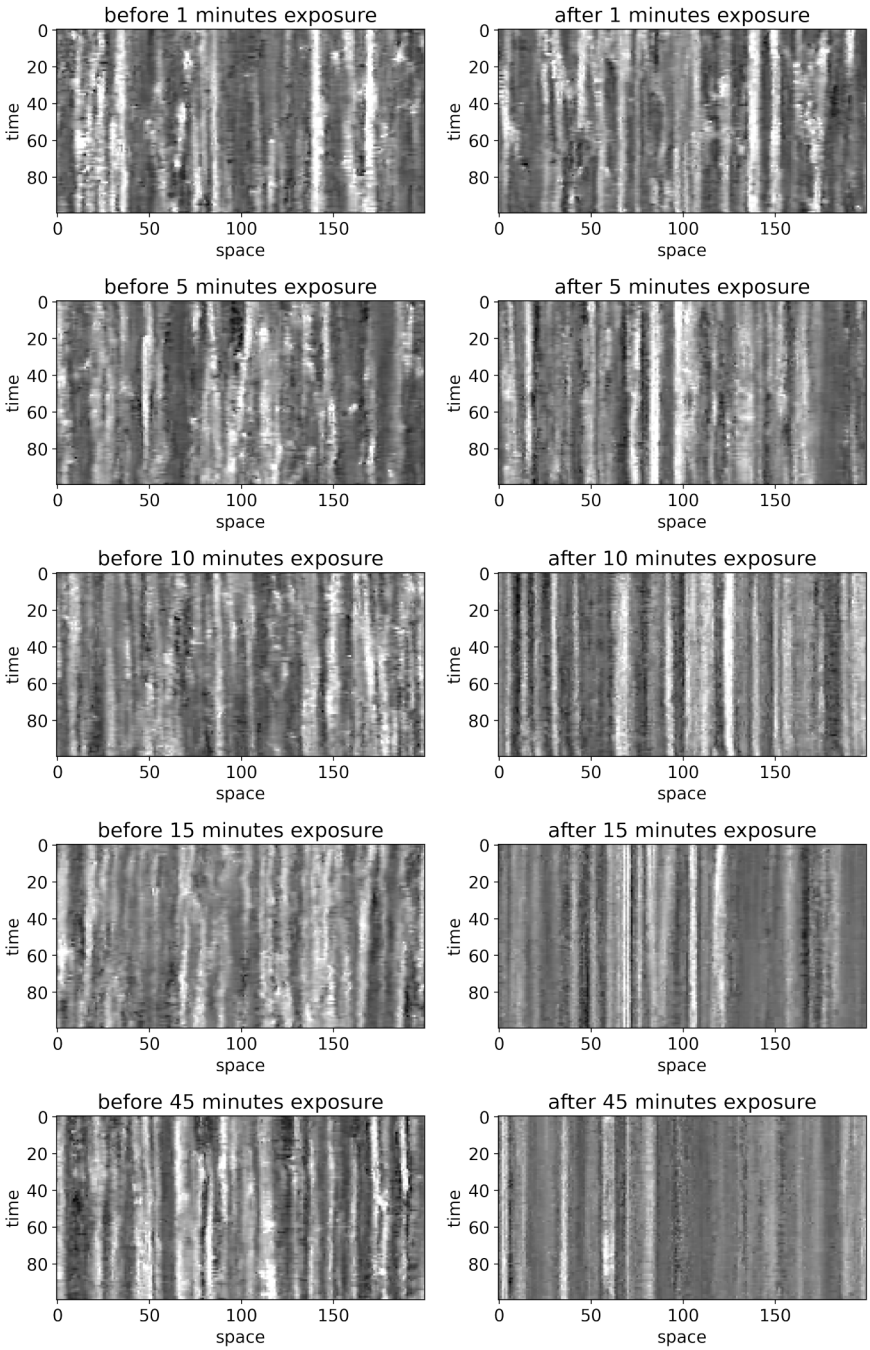

Fig. 2. Temporal slices: A table of temporal slices trough each of the video clips before and after exposure (rows) at different exposure times (columns). Looking at the columns of each image, it is clear that the intensity bands become more constant with longer exposure times.

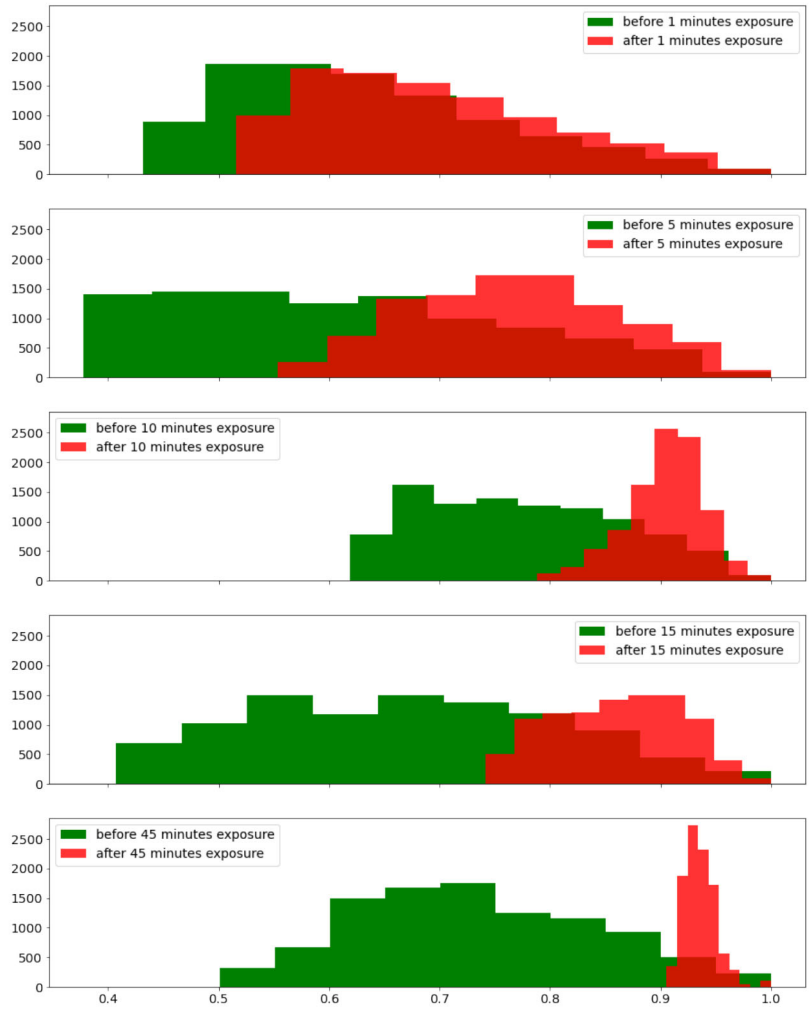

Fig. 3. Autocorrelation between frames. Histograms of the correlation values between the individual frame vectors in the selected portion of the movies. We observe that as exposure time increases (down) the spread of the correlation values after exposure (red) decreases and values move to the right (higher).

r

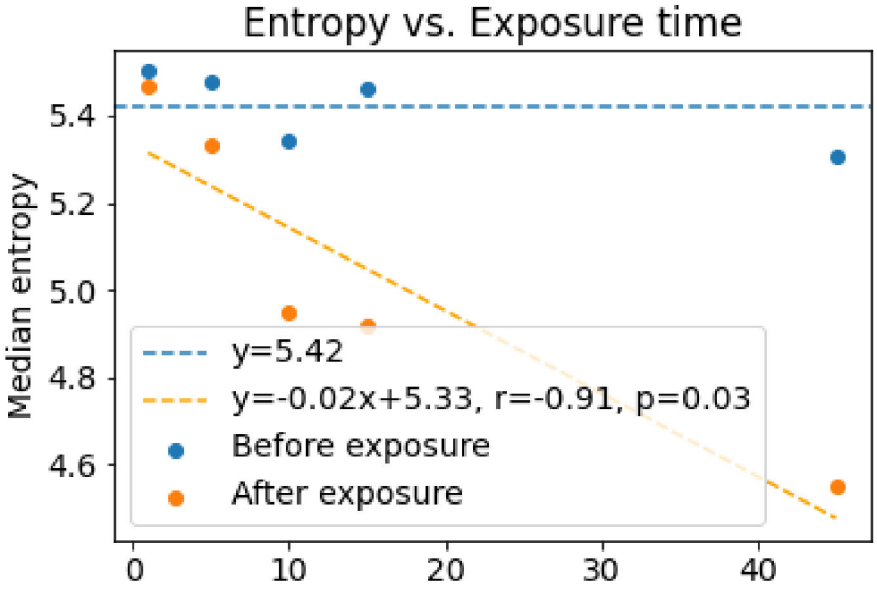

Fig. 4. Entropy The plot shows the median entropy values measured from the five movies. The blue values are from the frames before exposure; the orange values are from the frames after exposure; see Materials and Methods for details. The dashed blue line is a horizontal line corresponding to the median entropy of all videos before exposure. The dashed orange line is a least-squares fitting to the median entropy values after exposure.

4 Discussion

Our results suggest that sperm motility is affected much before viability when exposed to the X-ray beam. To the best of our knowledge, the direct effect of radiation damage to the sperm themselves has never been studied. The videos' correlation and entropy analysis clearly show that sperm motility decreases with increased exposure. At 45 minutes of exposure, the sperm do not move while only 5 % to 6 % of the sperm are classified as dead using the NucleoCounter. The damage caused to sperm by ionizing radiation could be related to several different events. The ionizing radiation could directly affect sperm motility by uncoupling the energy production in mitochondria or causing radiolysis in the surrounding fluid, resulting in damage from free radicals produced in this process. When free radicals accumulate, oxidative stress occurs, which can affect cell signaling (30) and subsequently cause sperm to stop moving, even before any membrane damage has occurred. Furthermore, it seems that cell death measured by membrane permeability is a much slower process and measured in the order of minutes (31).

The radiation dose during the experiment used for assessing the effect on motility was not directly comparable to a future single-cell experiment. During the population experiment, the full X-ray beam was used to expose as many cells as possible and quantitatively assess the damage done by the beam. However, to use the same instrument for SXRT, the focused Nanoscope beam would be used. The dose calculation indicates that a single-cell would receive a higher dose than the cells imaged in the centre of the petri dish during the performed population experiment. The dose calculations do not include sample rotation or the fact that the Petri dish was not fully illuminated as a single-cell sample would be, hence to get a more accurate estimate, a method for including these factors should be found.

The video data is subject to some variability. Known sources include placement of the petri dish and alignment of the microscope, which were both done manually and hence are prone to inaccuracies. Furthermore, the stage is rotated during the exposure, so the area captured by the camera is not identical before and after exposure. Given these variabilities and the small number of different exposure times (5), more measurements are needed to determine an exact relationship between dose and motility.

In conclusion, exposure to ionizing radiation from the full X-ray beam affects sperm motility within a few minutes, while cell viability only seems affected after X-ray extended exposure. The experimental setup described in this article provides a way to assess the radiation damage to sperm function right after exposure before long term effects take over. As sperm are among the most dynamic cells known and easy to come by, the method provides

a practical way to assess functional damage caused to sperm by ionizing radiation. As the motility is already affected after short X-ray exposure times, this first attempt shows that it is unlikely the TOMCAT Nanoscope can image the unaffected tail beating of live sperm without changes to the setup. Our method provides a way to estimate the feasibility of future live single-cell SXRT experiments concerning radiation damage.

5 Acknowledgement

MBL was supported by the Capital Region Research Foundation (Grant number: A5657) on the MAX4Imagers project (PI: Tim Dyrby).

We acknowledge the Paul Scherrer Institut, Villigen, Switzerland, for the provision of synchrotron radiation beamtime (20201724) at the beamline TOMCAT of the Swiss Light Source.

References

(1) R. Mokso et al. "Advantages of phase retrieval for fast x-ray tomographic microscopy". In: *Journal of Physics D: Applied Physics* 46.49 (Dec. 2013). ISSN: 00223727.

(2) H. Gadêlha, P. Hernández-Herrera, F. Montoya, A. Darszon, and G. Corkidi. "Human sperm uses asymmetric and anisotropic flagellar controls to regulate swimming symmetry and cell steering". In: *Science Advances* 6.31 (July 2020). ISSN: 2375-2548.

(3) C. Schiffer et al. "Direct action of endocrine disrupting chemicals on human sperm". In: *EMBO reports* 15.7 (July 2014), pp. 758–765. ISSN: 1469-221X.

(4) A. Rehfeld et al. "EDC IMPACT: Chemical UV filters can affect human sperm function in a progesterone-like manner". In: *Endocrine Connections* 7.1 (Jan. 2018), pp. 16–25. ISSN: 2049-3614.

(5) R. Mokso et al. "GigaFRoST: The gigabit fast readout system for tomography". In: *Journal of Synchrotron Radiation* 24.6 (2017), pp. 1250–1259. ISSN: 16005775.

(6) R. Mokso et al. "Four-dimensional in vivo X-ray microscopy with projection-guided gating". In: *Scientific Reports* 5 (2015), pp. 1–6. ISSN: 20452322.

(7) D. Kazantsev, E. Guo, A. B. Phillion, P. J. Withers, and P. D. Lee. "Model-based iterative reconstruction using higher-order regularization of dynamic synchrotron data". In: *Measurement Science and Technology* 28.9 (2017). ISSN: 13616501.

(8) A. Gonzalez-Tendero et al. "Whole heart detailed and quantitative anatomy, myofibre structure and vasculature from X-ray phase-contrast synchrotron radiation-based micro computed tomography". In: *European Heart Journal - Cardiovascular Imaging* 18.7 (July 2017), pp. 732–741. ISSN: 2047-2404.

(9) J. W. Buurlage et al. "Real-time reconstruction and visualisation towards dynamic feedback control during time-resolved tomography experiments at TOMCAT". In: *Scientific Reports* 9.1 (2019), pp. 1–11. ISSN: 20452322.

(10) A. T. Kuan et al. "Dense neuronal reconstruction through X-ray holographic nano-tomography". In: *Nature Neuroscience* 23.12 (2020), pp. 1637–1643. ISSN: 15461726.

(11) K. Z. Zefreh, F. M. Welford, and J. Sijbers. "Investigation on the effect of exposure time on scintillator afterglow for ultra-fast tomography acquisition". In: *Journal of Instrumentation* 11.12 (2016). ISSN: 17480221.

(12) C. Rau et al. "Micro- and nano-tomography at the DIAMOND beamline I13L imaging and coherence". In: *Developments in X-Ray Tomography XI*. Ed. by B. Müller and G. Wang. Vol. 1741. October 2017. SPIE, Oct. 2017, p. 28. ISBN: 9781510612396.

(13) J. Villanova et al. "Fast in situ 3D nanoimaging: a new tool for dynamic characterization in materials science". In: *Materials Today* 20.7 (2017), pp. 354–359. ISSN: 18734103.

(14) S. Flenner et al. "Pushing the temporal resolution in absorption and Zernike phase contrast nanotomography: Enabling fast in situ experiments". In: *Journal of Synchrotron Radiation* 27 (2020), pp. 1339–1346. ISSN: 16005775.

(15) S. Adjemian et al. "Ionizing radiation results in a mixture of cellular outcomes including mitotic catastrophe, senescence, methuosis, and iron-dependent cell death". In: *Cell Death and Disease* 11.11 (2020). ISSN: 20414889.

(16) A. P. Casarett and C. L. Comar. "Incapacitation and Performance Decrement in Rats Following Split Doses of Fission Spectrum Radiation". In: *Radiation Research* 53.3 (Mar. 1973). ISSN: 00337587.

(17) R. L. Chaput and R. T. Kovacic. “Miniature Pig Performance after Fractionated Supralethal Doses of Ionizing Radiation”. In: *Radiation Research* 44.3 (Dec. 1970). ISSN: 00337587.

(18) H. Ito, H. Watanabe, M. Takehisa, and H. Iizuka. “Isolation and Identification of Radiation-resistant Cocci Belonging to the Genus Deinococcus from Sewage Sludges and Animal Feeds”. In: *Agricultural and Biological Chemistry* 47.6 (June 1983). ISSN: 0002-1369.

(19) J. Kirz, C. Jacobsen, and M. Howells. “Soft X-ray microscopes and their biological applications”. In: *Quarterly Reviews of Biophysics* 28.1 (Feb. 1995). ISSN: 0033-5835.

(20) R. Grosch Daniel S.; Sullivan. “Induced Lethargy and the Radiation Control of Insects”. In: *Journal of Economic Entomology* 49.5 (Oct. 1956). ISSN: 1938-291X.

(21) G. Heidenthal. “THE OCCURRENCE OF X-RAY INDUCED DOMINANT LETHAL MUTATIONS IN HABROBRACON”. In: *Genetics* 30.2 (Mar. 1945), pp. 197–205. ISSN: 1943-2631.

(22) R. C. KING and J. P. WILSON. “Studies of the radiation syndrome in Drosophila melanogaster.” In: *Radiation research* 2.6 (Aug. 1955). ISSN: 0033-7587.

(23) D. S. Grosch. “Entomological Aspects of Radiation as Related to Genetics and Physiology”. In: *Annual Review of Entomology* 7.1 (Jan. 1962). ISSN: 0066-4170.

(24) M. Du and C. Jacobsen. “Relative merits and limiting factors for x-ray and electron microscopy of thick, hydrated organic materials”. In: *Ultramicroscopy* 184 (Jan. 2018), pp. 293–309. ISSN: 18792723.

(25) P. M. BENNETT, G. F. FOSTER, C. J. BUCKLEY, and R. E. BURGE. “The effect of soft X-radiation on myofibrils”. In: *Journal of Microscopy* 172.2 (Nov. 1993), pp. 109–119. ISSN: 00222720.

(26) F. De Felice et al. “Radiation effects on male fertility”. In: *Andrology* 7.1 (Jan. 2019). ISSN: 2047-2919.

(27) S. van der Walt et al. “scikit-image: image processing in Python”. In: *PeerJ* 2 (June 2014). ISSN: 2167-8359.

(28) M. R. Howells, A. P. Hitchcock, and C. J. Jacobsen. “Introduction: Special issue on radiation damage”. In: *Journal of Electron Spectroscopy and Related Phenomena* 170.1-3 (Mar. 2009), pp. 1–3. ISSN: 03682048.

4 Reconstruction

What are the possibilities and limitations of dynamic tomography?

This chapter discusses possible solutions to dynamic reconstructions from X-ray projections. First, a brief overview of some classical tomographic reconstruction algorithms is given, followed by some experimental results for sparse reconstruction, where few but multiple projections of a static state of the object are available to reconstruct each time frame. Finally, true dynamic reconstruction is discussed, where the projections are acquired while the object moves.

4.1 Classical tomography algorithms

One of the cornerstones of X-ray computed tomography is the Radon transform, discovered by Johan Radon in 1917 and later made famous by Allan McLeod Cormack and Godfrey Hounsfield in 1979 when they won the Nobel Prize in Physiology or Medicine for the invention of CT. The Radon transform is the act of taking infinitely many projections of an object onto a lower-dimensional space. An example of taking the Radon transform would be turning a 2D object and collecting all the projections onto the x-axis. The aim of computed tomography is then to recover the higher dimensional object from the lower-dimensional projections. One of the first ways to solve this problem was by use of the Fourier slice theorem, which says that taking the 2D Fourier transform of a 2D object is equivalent to taking the radon transform followed by a 1D Fourier transform, see Figure 4.1.

Let $f(\boldsymbol{x}) : \mathbb{R}^2 \to \mathbb{R}$ be a 2D function such as a gray scale image. Then projection $p(x_1)$ onto the x-axis is given by:

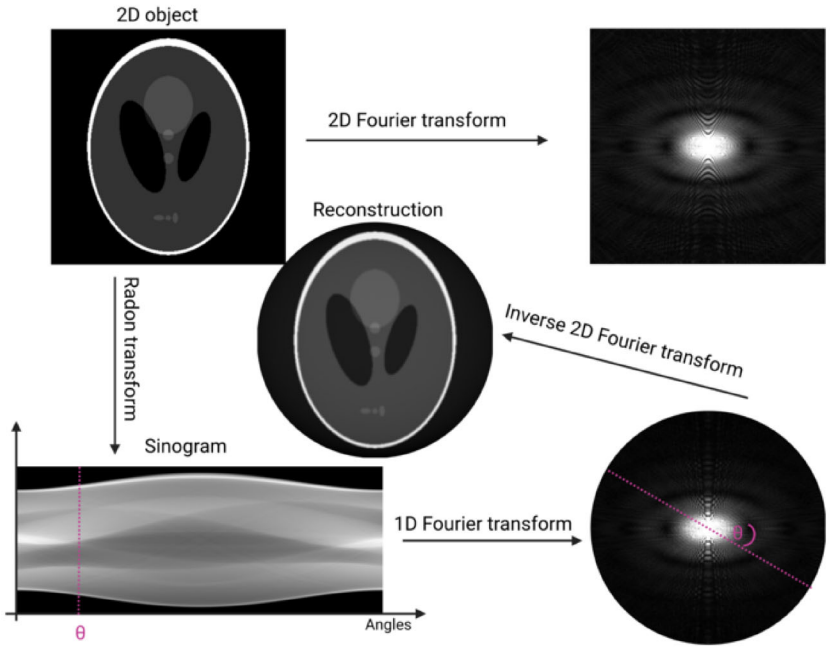

Figure 4.1.: Fourier slice theorem. An illustration showing how to apply the Fourier Slice Theorem to reconstruct a classic Shepp Logan Phantom.

$$p(x_1) = \int_{-\infty}^{\infty} f(\boldsymbol{x}) dx_2$$

The Fourier transform $F(u, v)$ of $f(\boldsymbol{x})$ is defined as.

$$F(u, v) = \int_{-\infty}^{\infty} \int_{\infty}^{\infty} f(\boldsymbol{x}) e^{-2\pi i(ux_1 + vx_2)} dx_1 dx_2$$

One slice, or line of the Fourier transform is simply $s(u) = F(u, 0)$

$$
\begin{aligned}
F(u,0) &= \int_{-\infty}^{\infty}\int_{\infty}^{\infty} f(\boldsymbol{x}) e^{-2\pi i(ux_1)} dx_1 dx_2 \\
&= \int_{-\infty}^{\infty}\left[\int_{\infty}^{\infty} f(\boldsymbol{x}) dx_2\right] e^{-2\pi i(ux_1)} dx_1 \\
&= \int_{-\infty}^{\infty} p(x_1) e^{-2\pi i(ux_1)} dx_1
\end{aligned}
$$

which is exactly the 1D Fourier transform of $p(\boldsymbol{x})$.

Let $\boldsymbol{R} : \mathbb{R}^2 \to \mathbb{R}^2$ be the linear transformation of rotating image $f(\boldsymbol{x})$ by an angle θ then we have

$$
\begin{aligned}
F(f \circ \boldsymbol{R})(\boldsymbol{u}) &= \int_{-\infty}^{\infty}\int_{\infty}^{\infty} f(\boldsymbol{R}\boldsymbol{x}) e^{-2\pi i\langle \boldsymbol{u},\boldsymbol{x}\rangle} dx_1 dx_2 \\
&= \frac{1}{|\det \boldsymbol{R}|}\int_{-\infty}^{\infty}\int_{\infty}^{\infty} f(\boldsymbol{y}) e^{-2\pi i\langle \boldsymbol{u},\boldsymbol{R}^{-1}\boldsymbol{y}\rangle} dy_1 dy_2,
\end{aligned}
$$

by change of variable $\boldsymbol{x} = \boldsymbol{R}^{-1}\boldsymbol{y}$. By the definition of the adjoint operator $\langle \boldsymbol{u}, \boldsymbol{R}^{-1}\boldsymbol{y}\rangle = \langle (\boldsymbol{R}^{-1})^*\boldsymbol{u}, \boldsymbol{y}\rangle$. Since the rotation matrix is orthogonal $(\boldsymbol{R}^{-1})^* = \boldsymbol{R}$ and $|\det \boldsymbol{R}| = 1$, hence

$$
F(f \circ \boldsymbol{R}) = F(f) \circ \boldsymbol{R}.
$$

The Fourier slice theorem leads to the following intuitive reconstruction procedure. Given projections from many rotations of $f(\boldsymbol{x})$, we could fill the Fourier space with the data and perform the reconstruction by a 2D inverse Fourier Transform. The reconstruction approach known as Filtered Back Projection (FBP) is based on this idea with a few modifications to account for practical problems. More details, including a good explanation on where the *filtered* part of the name comes from, can be found in [25]. For 3D reconstruction, there are similar methods, such as the Feldkamp Davis Kress algorithm (FDK) [12].

Another classical method for tomographic reconstruction is based on viewing the problem as a linear system of equations. One can describe the Radon transform as a linear transformation by discretizing the object to be reconstructed into N pixels and modelling the X-rays as straight lines parameterized by an angle θ and a signed distance ρ, $\rho = cos(\theta)x + sin(\theta)y$. Then the sinogram values p_i for each (θ, ρ) are a weighted sum of the attenuation at each pixel f_j that the (θ, ρ) ray passes through:

$$\sum_{j=1}^{N} a_{ij} f_j = p_i \tag{4.1}$$

Where a_{ij} are the weights, corresponding to the fraction of the pixel j that the ray i covers.

The projections can be written as a column vector $\boldsymbol{p}$ and the attenuation values to be reconstructed as a column vector $\boldsymbol{f}$. Then writing the weights as an $M \times N$ matrix $\boldsymbol{A}$, the reconstruction problem can be written on the linear form:

$$\boldsymbol{p} = \boldsymbol{A}\boldsymbol{f}. \tag{4.2}$$

Hence, the matrix $\boldsymbol{A}$ is a discretized version of the Radon transform. The linear system of equations may easily be solved under the right circumstances. However, this is rarely the case for real-world tomography problems. In most real cases, $M > N$, i.e. the number of projections, is larger than the number of pixels to be reconstructed. Furthermore, the weight matrix is typically close to being singular and extremely large. Additionally, the data is often corrupted by noise. Hence typically, an optimization problem is solved instead, such as the least-squares problem:

(a) SIRT iterations

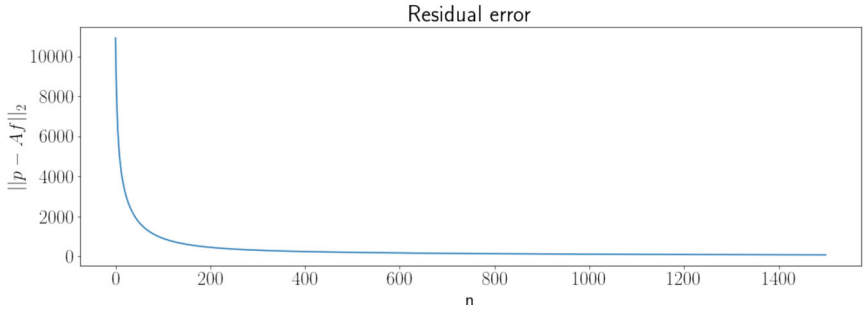

(b) SIRT residual

Figure 4.2.: **Iterative reconstruction** (a) The reconstructions after increasing iterations left-to-right of the SIRT algorithm. (b) The residual decreases with the number of iterations.

$$\boldsymbol{f}_{opt} = \underset{\boldsymbol{f}}{\operatorname{argmin}} \left\{ 1/2 \left\| \boldsymbol{p} - \boldsymbol{A}\boldsymbol{f} \right\|_2^2 \right\} \tag{4.3}$$

Different methods and regularization techniques can be used to find an optimal solution, such as Landweber's method [20]. If we define

$$\mathcal{G}(f) = 1/2 \left\| \boldsymbol{p} - \boldsymbol{A}\boldsymbol{f} \right\|_2^2$$

then we can find the optimal solution $\boldsymbol{f}_{opt}$ of Equation 4.3 by the method of steepest descent where $\nabla\mathcal{G}(f) = -\boldsymbol{A}^T \left(\boldsymbol{p} - \boldsymbol{A}\boldsymbol{f} \right)$. Hence the solution can be found iteratively with each step being defined as:

$$\boldsymbol{f}^{n+1} = \boldsymbol{f}^n + w_n \boldsymbol{A}^T \left(\boldsymbol{p} - \boldsymbol{A}\boldsymbol{f} \right),$$

where w_n is the step size. The operation of $\boldsymbol{A}$ is referred to as forward-projection since this operation models the forward problem, i.e. the process of the X-ray projection. The operation of $\boldsymbol{A}^T$ is called the back-projection. The iterative process can be thought of intuitively as starting with a blank canvas, and for each projection angle, smearing the detector values back across the canvas along the projection lines; this is called back-projection. The canvas is updated with the difference between the forward-projection and the original projection values in each iteration. There are different variations of these algorithms which incorporate weights and constraints to improve convergence and reconstruction quality, with a popular one being the Simultaneous Iterative Reconstruction Technique (SIRT), see Figure 4.2. The matrix $\boldsymbol{A}$ is huge for real reconstruction problems. For this reason, parallel computing is used to speed up the reconstruction problems, as the large number of matrix computations involved make them well suited for parallel computation.

4.1.1 Comparing SIRT and FBP

The traditional tomographic reconstruction algorithms described above are based on three fundamental assumptions 1) that many projections are acquired, 2) widely scattered across different directions, and 3) that the object is static. The first two assumptions are frequently violated at the expense of the reconstruction quality since X-rays are harmful to most living organisms, and hence fewer projections are acquired to minimize the absorbed radiation dose. In this section, some results illustrate how this violation affects the reconstruction quality.

During a visit to Helsinki University, data was collected in collaboration with Alexander Meaney, using their micro-CT device described here [24]. Four phantoms were made consisting of spiral hair bands made of plastic filled with play dough, see Figure 1.3. The geometry of the CT was a cone-beam geometry, meaning that the X-rays were cast from a single point source in a cone to a flat panel detector. The distance from the source to the detector was 630 mm and the distance from the source to the rotation centre was 540 mm. The detector had 2368×2240 detector pixels, and 361 projections were acquired.

To perform reconstruction and compare the different methods described above, the GPU accelerated implementations of FBP and SIRT in the ASTRA toolbox [1,

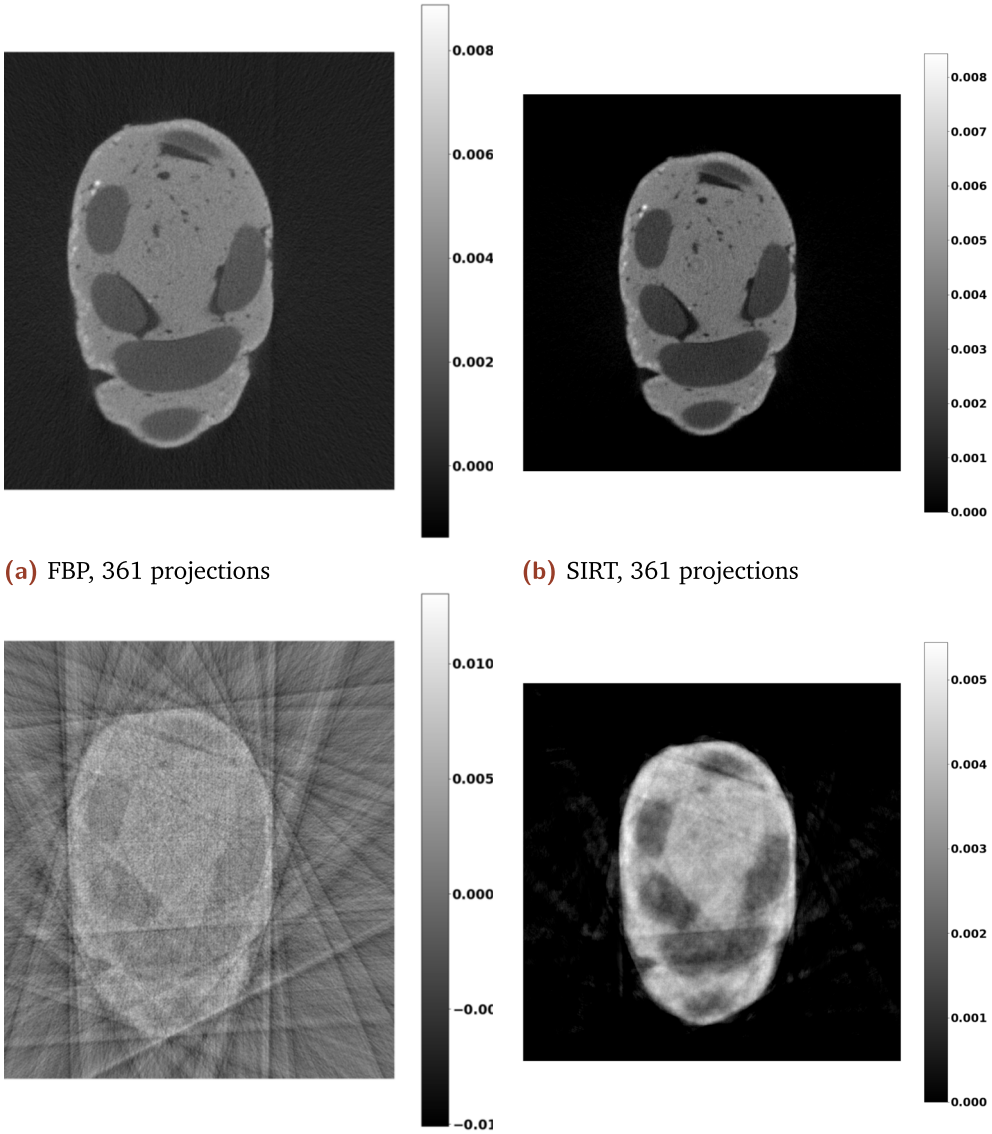

(a) FBP, 361 projections

(b) SIRT, 361 projections

(c) FBP, 16 projections

(d) SIRT, 16 projection

Figure 4.3.: FBP vs. SIRT for a full angle and sparse angle problem In the left column are fast FBP reconstructions of a physical plastic and play-dough phantom, on the right are SIRT reconstructions of the same phantom. In the top row the reconstruction is made with the full set of 361 projections acquired, on the bottom row 16 evenly spaced projections were used.

2, 30] were used. The reconstructions were performed on a GeForce RTX 3090 GPU, and only the central slice was reconstructed, see Figure 4.3. A minimum constraint was applied to the SIRT reconstruction, meaning negative values were clipped to 0.0 at each iteration. A decent reconstruction is obtained using either FBP or SIRT with many projections. However, when only 16 of the projections are used, the SIRT reconstruction performs better when the simple minimum constraint is incorporated. The problem where only a few projection angles are used is referred to as a *sparse reconstruction problem*

The line artefacts are visible in both sparse reconstructions, but because of the minimum constraint, which is easily incorporated in the SIRT implementation, the result is better, allowing the dark areas inside the object to be more easily distinguished. The results can be further improved by regularization techniques that guide the solution towards are more desired outcome. Examples of such regularizers are Tikhonov regularization, which guides the solution towards a smooth outcome, and total variation regularization, favouring piecewise constant solutions.

Algorithms which perform well for sparse tomographic reconstruction are interesting for tomographic reconstruction of living samples for three reasons. Firstly, good algorithms for sparse reconstructions allow imaging at a lower radiation dose. Secondly, it can be faster to take fewer projections, which limits the total amount of movement of the sample. Finally, X-ray setups that can acquire multiple projections simultaneously have been developed [39], and this could allow some dynamic samples to be reconstructed by sparse reconstruction algorithms. Therefore, the following section deals with algorithms particularly well suited for sparse reconstruction.

4.2 Sparse Reconstructions

A sparse reconstruction is a reconstruction made from a limited number of projection views, typically less than 100 views [16]. Such reconstructions suffer from line artefacts, as visible in Figure 4.3(c), or lack of detail as seen in Figure 4.3(d). However, improvements can be made over the basic FBP or constrained SIRT reconstruction. This section will show results from testing

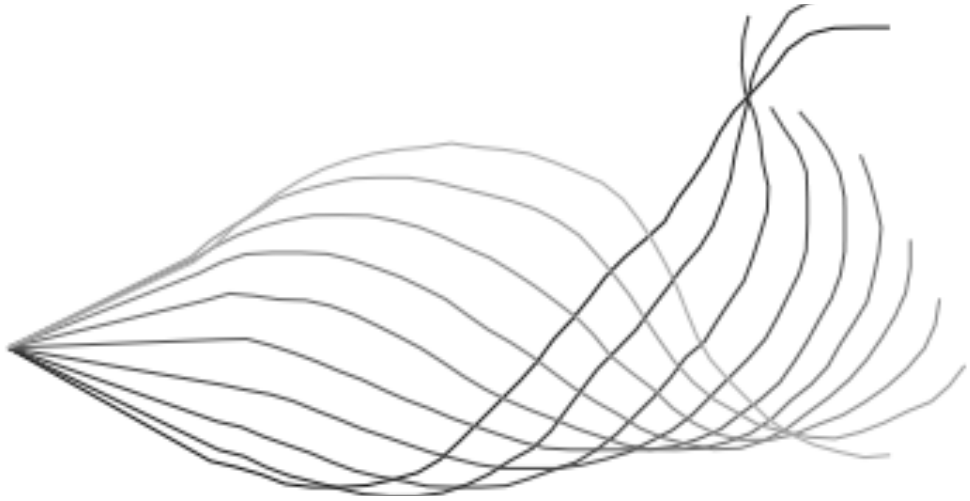

Figure 4.4.: Showing first 10 positions of a sperm cell tailbeat.

two algorithms well suited for sparse reconstruction on a digital 2D sperm phantom.

The work in this section was done in collaboration with Jakeoung Koo and Vedrana Andersen Dahl during a stay at the Technical University of Denmark (DTU). Vedrana Andersen Dahl provided supervision, expert knowledge, the Figure 4.6 and the explanation of her method [10]. The implementations of the reconstruction algorithms were made in collaboration with Jakeoung Koo[1].

4.2.1 Sperm Phantom

A simple binary 2D phantom was constructed based on tracked flagellum data made publicly available with [34]. This data set consists of segmented and skeletonized video recordings of sperm cell tail beatings recorded with a microscope taking pictures every 2 ms. The sperm cell is gently pinned by the head, which causes it to rotate around itself as the tail beats instead of propelling it forward. In Figure 4.4, a sequence of ten consecutive tail configurations of a sperm cell is shown.

On a synchrotron, we have reached 20 ms sampling intervals, see Chapter 2, hence for the reconstructions in this section, we picked skeletons ten frames

[1]The implementations can be found here `https://github.com/JuliaTomo`

apart to match the sampling achieved at the synchrotron. The skeleton was converted to a flattened curve with a constant radius and attenuation.

A finer grid was used for data generation than for the reconstruction to avoid committing an inverse crime [28]. Two methods are compared; Total Variation Reconstruction and Direct Segmentation via Deformable Curves [10]. Sparse reconstructions are particularly sensitive to noise in the data [16], hence for more realistic performance evaluations, a 1% Gaussian noise was added to the sinogram. For all reconstructions in this section, a 609×609 image was reconstructed, and 852 detector positions were used.

4.2.2 Total Variation Regularization

Optimization-based methods with regularization to guide the solution can be used to reconstruct sparse or noisy data. Total variation (TV) regularization promotes piecewise constant solutions and is promising for reconstructing the fat curve sperm phantom. TV minimization has been shown to eliminate line artefacts while preserving fine structures well [16, 15]. The TV minimization problem is defined as:

$$\boldsymbol{f}_{\text{opt}} = \underset{\boldsymbol{f}}{\operatorname{argmin}} \left\{ \|\boldsymbol{A}\boldsymbol{f} - \boldsymbol{p}\|_2^2 + \lambda \|\nabla \boldsymbol{f}\|_{2,1} \right\} \tag{4.4}$$

The variable $\boldsymbol{f} \in \mathbb{R}^n$ is an image in n pixels, the matrix $\boldsymbol{A}$ is the forward operator described above, and $\boldsymbol{p}$ is the data. $\nabla \boldsymbol{f}$ is computed as a finite difference approximation of the image gradient. The algorithm was implemented in Julia using the Primal-Dual approach of Chambolle and Pock [9].

The best reconstructions obtained with this method are shown in Figure 4.5, using eight evenly spaced angles. The best regularization parameter was found to be 0.1, by trying with the following parameters: $0.0001, 0.001, 0.01, 0.05, 0.1, 0.2, 0.3, 0.5$ and picking the parameter which gave the best reconstruction. Reconstructions from fewer angles, such as seen in the bottom row of Figure 4.5 tend to perform poorly in some cases, such as seen in the third frame. In this frame, it is also clear that while the regularization parameter removes line artefacts

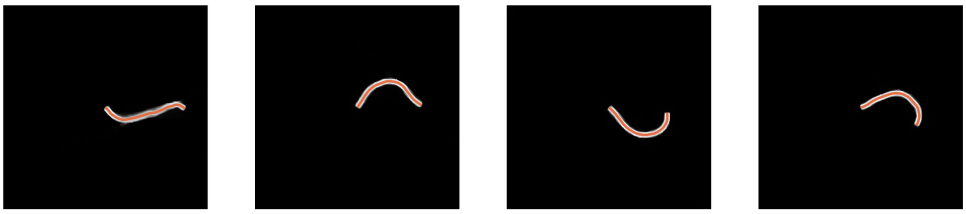

(a)

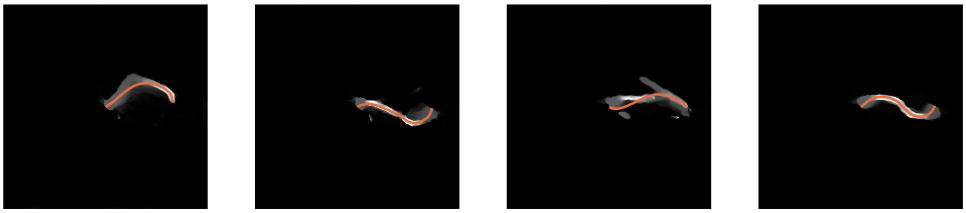

(b)

Figure 4.5.: The reconstruction results using the implemented TV regularized reconstruction method, with $\lambda = 0.1$. The red curves are the ground truth center-lines, and the grey level image in the background is the reconstruction. (a) reconstructions using 8 angles. These reconstructions are very true to the shape of the tail. (b) reconstruction using 4 angles, these reconstructions are not completely true to the shape of the tail.

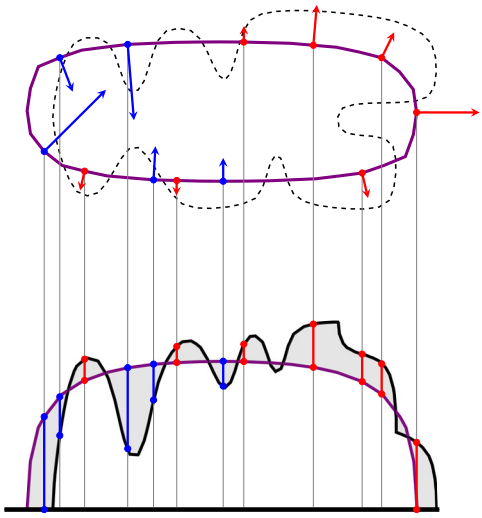

Figure 4.6.: Illustration of the method from [10].

and keeps the reconstruction constant in most cases, it can also give a blocky effect and can emphasize errors in some cases.

4.2.3 Direct Segmentation via Deformable Curves

The method in [10] delineates the object to be segmented using a simple closed curve and is therefore only applicable for solving problems involving a single object. However, when having only one object, the strong regularization provided by the method proves advantageous against intense noise or a limited number of projections. The method achieves the reconstruction by iterative curve deformation to minimize a residual. The essence of the approach is illustrated in Figure 4.6. An unknown object (black dotted line) has produced a projection (black line). The curve initiated in the vicinity of the object (purple) should be deformed such that it comes closer to the boundary of the object. The projection of the curve (also in purple) and the residual (grey) are computed to achieve the deformation. The points of the curve corresponding to the negative residual (blue lines) should be moving inwards (blue arrows), while the positive residual (red) corresponds to the outwards movement (red arrows). For every point on the curve, the corresponding residual (blue lines for negative, red lines for positive values) gives a normal displacement size (blue arrows for inwards and red arrows for outwards).

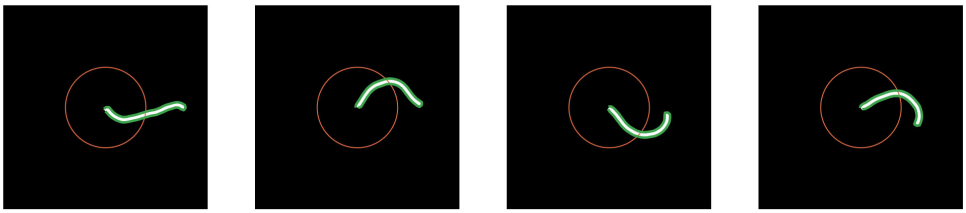

(a)

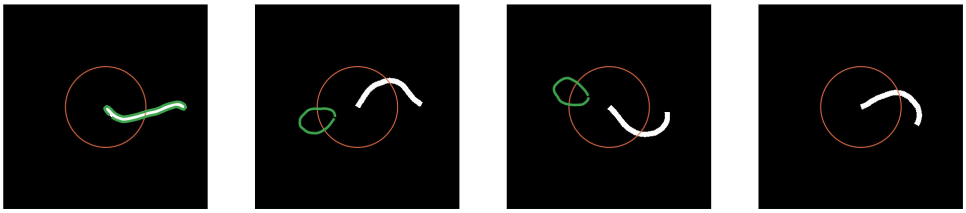

(b)

Figure 4.7.: (a) The results of running the reconstruction method from [10] with eight equally spaced projections. The reconstructions are the green snakes, and the black and white image in the back ground is the ground truth. The red circle is the initialization curve. (b) The same approach when using only 4 angles.

Using the method in [10] very accurate reconstructions are possible from as little as eight static projections, see Figure 4.7. However, while reconstructions from fewer angels are possible, the method becomes less robust concerning the angles chosen, even if they are evenly spaced. In Figure 4.7 the first frame is nicely reconstructed, but the method did not converge for the rest of the reconstructions. The technique has two regularization parameters and a step size that must be tuned. The regularization parameters control the elasticity and stiffness of the curve. A value of 0.01 for both regularization parameters was found to perform best by trying $0.5, 0.2, 0.01$. The step-size 0.2 was found to perform best by trying the same sizes. A downside to the direct segmentation approach is that three parameters need to be tuned.

4.2.4 Comparison Between TV-regularization and Direct Segmentation via Deformable Curves

Both methods perform very well on this simple phantom with as little as eight projection angles. Both ways are extendable to 3D [15, 17], and have different advantages and disadvantages. The total variation reconstruction (TV-reconstruction) can be used for reconstructing multiple objects of various grey levels. Furthermore, the overall approach is flexible in that the regularization term can be changed to match prior knowledge of the object grey level structure. However, iterative algorithms such as the TV-minimization procedure require many applications of the forward-and back-projections to converge. The article following this section shows that these operations are slow to compute but can be effectively parallelized. The segmentation via deformable curves has the advantage of being fast and directly providing a segmentation. Hence, this is a significant advantage if segmentation is needed since a post segmentation step can be skipped. However, it is limited to reconstructing a single object having one attenuation value. Both methods require some parameter-tuning to work well, which can be rather time-consuming.

Using a high-level parallel programming language for GPU-accelerated tomographic reconstruction

Mette Bjerg Lindhøj[1,2], Troels Henriksen[1], Kari Pedersen[1], Jon Sporring[1]
[1] Department of Computer Science, University of Copenhagen, Copenhagen, Denmark
[2] Danish Research Centre for Magnetic Resonance, Center for Functional and Diagnostic Imaging and Research Copenhagen University Hospital Hvidovre, Hvidovre, Denmark
memo@di.ku.dk, athas@sigkill.dk, laerke.b.pedersen@gmail.com, sporring@di.ku.dk

***Abstract*—This paper aims to determine the usefulness of using a high-level parallel programming language for implementing parallel high-performance tomographic reconstruction algorithms. The purpose of this is to make it easier for researchers to implement advanced model-based iterative reconstruction algorithms for use at synchrotron facilities, while still taking advantage of hardware such as GPUs. To this end, we implement the forward- and back-projection in the programming language *Futhark*, and verify their applicability through an implementation of an algebraic reconstruction algorithm. We obtain promising performance results by use of algorithmic considerations instead of low-level optimizations. Finally, we demonstrate that the implementation makes it possible to prototype implementations of iterative reconstruction algorithms on a standard laptop while still obtaining good scaling towards high-end GPUs.**

***Index Terms*—Futhark, SIRT, tomographic reconstruction, algebraic reconstruction, forward-projection, back-projection, parellelization, high-level language, GPU, OpenCL**

I. Introduction

The inverse problem of reconstructing an image or volume from its x-ray projections is a well-studied problem with applications in for example synchrotron imaging of biological samples. Efficient algorithms and implementations with high-quality results exist when it is possible to acquire enough angles at optimal exposure. However, when the data is nonoptimal with lots of noise or few angles, more advanced methods are needed. Iterative reconstruction techniques are promising for this branch of tomographic reconstruction as they can incorporate priors, regularization, and constraints [1, 2, 3]. The drawback of iterative techniques is a high computational cost. Many examples show that parallel implementations accelerated by GPUs greatly improve the performance but, to the best of our knowledge, all such implementations are based on the low-level language implementations in CUDA or OpenCL [4, 5, 6, 7, 8, 9, 10]. While these implementations can have great performance, they lack flexibility in terms of easy modifications from an algorithmic research perspective.
An exception is an implementation in the ASTRA toolbox [11], an open source toolbox for tomographic reconstruction algorithms. The ASTRA toolbox includes CUDA implementations of the forward- and backward-projection steps, which are the basic components of most iterative reconstruction algorithms, effectively corresponding to two matrix-vector products, where the two matrices are each others' transpose. These primitives are callable from a Matlab or Python interface for easy prototyping of new tomographic algorithms. The performance of running a forward- or back-projection in ASTRA is good, and most simple quality-optimizing methods are readily available or possible to implement via `pygpu`. However, for more advanced model-based iterative algorithms it becomes difficult to use these primitives without incurring the overhead of data transfer to and from the GPU or resorting to writing custom OpenCL/CUDA kernels, which are hardware specific and time-consuming to write. Furthermore, the forward- and back-projections in ASTRA are *unmatched*, meaning that the matrix used during the back-projection is only an approximate transpose. Using an unmatched back-projector is a technique used to improve the performance of the back-projection, and can improve convergence of the algorithm, but it may also ruin convergence guarantees [12]. Hence, when using the primitives for a variety of algorithms with convergence guarantees based on a matched projection pair, a matched implementation is needed, or a proof of the validity in each use case. For related work on matched projectors see [7].
For work on new model-based iterative reconstruction algorithms, we needed an implementation where we could easily incorporate our models in the parallel implementation, such that the modeling would also benefit from hardware acceleration. To this end, we investigated how the high-level parallel programming language *Futhark* [13] could be used for implementation of the forward- and back-projection primitives, and exemplified their use in reconstruction in an implementation of the Simultaneous Iterative Reconstruction Technique (SIRT). Since we will be working with synchrotron data, which is most commonly *parallel beam*, we limited our study to this simple geometry. However, the algorithm we base our implementation on also has an extension to the cone beam case. The main contributions of our study are:

- We show that forward- and back-projection can be implemented as portable code in a high-level language, and still achieve competitive performance on a GPU, by use of algorithmic considerations.
- We show that this implementation makes it possible to perform reconstruction on both a multicore CPU and GPUs from both NVIDIA, AMD, and Intel.

- We show that we can get a speedup of 2× for a matched back-projection implemented in a high-level language compared to a low-level optimized unmatched back-projection.

II. Background

Computed tomography is the inverse problem of reconstructing an image or volume from its x-ray projections. The x-ray source spins around the object to be analyzed and sends x-rays through the object onto a detector on the opposite side. The rays through the object provide a measure for attenuation used in reconstruction.

Reconstruction algorithms are roughly divided into two classes of algorithms: fast analytic algorithms based on the Fourier slice theorem, and iterative algorithms, which give better results for noisy and sparse data, but has slower sequential run-time. Here, we consider a subclass of iterative algorithms, called algebraic reconstructions methods.

The projection process can be modeled as a linear transformation by discretizing the solution space into n pixels. First, we place a coordinate system with origin at the center of the object to be reconstructed and denote by $\boldsymbol{\theta}$ the vector of projection angles. For each angle, several equidistant x-rays are cast from the source. Let $\boldsymbol{\rho}$ be the signed distances from each line to the origin. Each ray, r_i, can be modelled as a straight line given by the equation $\rho = \cos(\theta)x + \sin(\theta)y$. For each ray, the weighted sum of attenuation at each pixel f_j that the ray passes through approximates the projection value p_i as illustrated in Fig. 1. Writing $\boldsymbol{p}$ and $\boldsymbol{f}$ as column vectors, the model for the system is:

$$\boldsymbol{A}\boldsymbol{f} = \boldsymbol{p}, \tag{1}$$

where the system matrix $\boldsymbol{A}$ is the $m \times n$ matrix of weights a_{ij} modelling our system. We have used the line model where

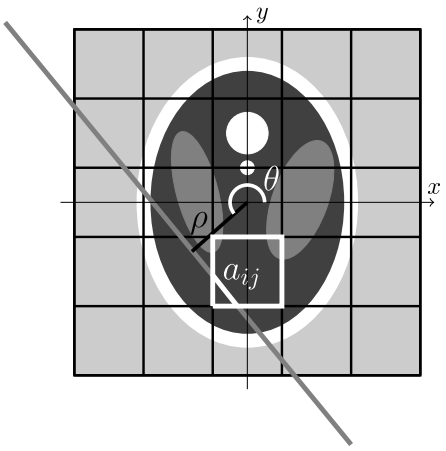

Figure 1. A schematic of the model where the ray r_i (grey line) passes through the pixel f_j (highlighted in white). The angle θ is the angle between the x-axis and the normal to the ray. The value ρ is given by the equation $\rho = \cos(\theta)x + \sin(\theta)y$.

a_{ij} is the length of the intersection between the pixel f_j and the ray r_i.

The system of equations may be solved directly when $n = m$. However, the system matrix is typically close to being singular and extremely large, making a solution by pseudo-inverse impractical. In most real cases $m > n$, i.e., the number of projections is larger than the number of pixels to be reconstructed. Nevertheless, we are particularly interested in the sparse case where $n < m$. Algebraic methods approximate a solution by solving the optimization problem:

$$\min_{\boldsymbol{f} \in C} \left\| \boldsymbol{M}^{1/2}(\boldsymbol{A}\boldsymbol{f} - \boldsymbol{p}) \right\|_2, \tag{2}$$

where C is a convex set of constraints, and $\boldsymbol{M}$ is a weight matrix.

Many algebraic reconstruction algorithms proposed in the literature can be seen as special cases of the optimization algorithm given in Algorithm 1. In the algorithm, $\boldsymbol{D}$ and $\boldsymbol{M}$ are

Algorithm 1 General projected gradient algorithm

for $k = 0, 1, 2 \ldots :$ **do**
  $\boldsymbol{f}^{k+1} = P_C(\boldsymbol{f}^k + \lambda \boldsymbol{D}\boldsymbol{A}^T\boldsymbol{M}(\boldsymbol{p} - \boldsymbol{A}\boldsymbol{f}^k))$
end for

positive definite matrices, P_C denotes projection onto a convex set of constraints, $0 < \lambda < 2 \left\| \boldsymbol{D}^{-1/2}\boldsymbol{A}\boldsymbol{M}^{-1/2} \right\|_2^2$ [14], and $\boldsymbol{f}^0$ is an initial guess at the object to be reconstructed - typically the zero vector.

The performance of Algorithms following the general scheme shown in Algorithm 1 must be improved, as the sequential runtime makes them impractical. There are two ways to improve their performance:

- Improve convergence of the algorithm and hence reduce the number of iterations.
- Improve the run-time of each iteration.

In this study, we focused on improving the run-time of each iteration through parallelization. The update step has two primary bottlenecks: Determining the matrix $\boldsymbol{A}$ and the subsequent matrix multiplications involving it. The operations $\boldsymbol{A}\boldsymbol{f}$ and $\boldsymbol{A}^T\boldsymbol{p}$ are called the forward- and back-projections [15], a terminology which will be adapted here for the more general solution in Algorithm 1. For our study, we chose to focus on implementing these two operations in the high-level data-parallel language Futhark, and exemplify their use by implementing the SIRT algorithm. SIRT is a special case of the general projected gradient algorithm where each update step is given by:

$$\boldsymbol{f}^k = \boldsymbol{f}^{(k-1)} + \boldsymbol{C}\boldsymbol{A}^T\boldsymbol{R}(\boldsymbol{p} - \boldsymbol{A}\boldsymbol{f}^{(k-1)}), \tag{3}$$

where $\boldsymbol{C}$ and $\boldsymbol{R}$ are the diagonal matrices containing the inverse column and row sums of the system matrix $\boldsymbol{A}$ respectively.

III. Implementation

Futhark is a data-parallel purely functional array language that uses an optimizing compiler to generate parallel OpenCL

```
map (\θ ->
   map (\ρ ->
        reduce (+) 0.0 (
             map (\i ->
                  calculate x_i in ρ = cos(θ)x_i + sin(θ)i
                  calculate x_{i+1} equivalently
                  calculate l_i and l_{i+1} by (4) and (5)
                  get pixel value f_i at (x_i, i)
                  get pixel value f_{i+1} at (x_{i+1}, i+1)
                  in l_i · f_i + l_{i+1} · f_{i+1}
             ) ((-n/2)...(n/2-1))
        )
    ) rhos
) thetas
```

Figure 2. A description of the forward-projection, which uses two nested `maps` and an innermost composition of `map` and `reduce`, for a total of three levels of application parallelism.

code. It is similar to other languages in the ML family (SML, OCaml, F#, Haskell, etc.). Using Futhark for our implementation has three major advantages. Firstly, we can draw upon the compiler to parallelize the code and keep the implementation simple and easily modifiable. Second, Futhark is hardware agnostic and can translate to sequential C, OpenCL, PyOpenCL and others, [16] which makes it both easy to develop our algorithms and easy for the end user to use from their preferred interface. Thirdly, Futhark can take advantage of several levels of parallelism which means that the code can be optimized for different hardware and data configurations without any code change [17]. For our implementations, we mainly used the two second-order array combinators (SOACs) `map` and `reduce` in Futhark. The map operator applies a function to every element of the input array and returns a new array of the transformed elements, while reduce is used for summary operations [13]. For example, summing an array `xs` is expressed as: `reduce (+) 0 xs`.

The system matrix $\boldsymbol{A}$ is too large to fit on most GPUs for real-world problems [18], and therefore, we chose to compute the matrix on the fly. A common approach is to use a standard ray tracing technique based on the incremental Siddon algorithm [19]. However, to allow for more compiler optimizations, and optimize our implementation towards the sparse reconstruction case, we chose a slightly different algorithm described in [20] and adapted it to the parallel beam geometry.

The main idea in the forward-projection in [20] is that if the slope of the ray is greater than 1 (steep rays), then the ray will pass through at most 2 pixels in each row. Using this we chose to implement the forward-projection as shown in Fig. 2.

On GPUs, accessing memory is a significant bottleneck. To minimize the overhead of reading and writing to memory, it is beneficial to have *coalesced memory access*, which is achieved when consecutive threads access consecutive memory addresses. The approach used in our forward-projection guarantees coalesced write operations, as the forward-projection values are in the order of the rays, and almost coalesced read

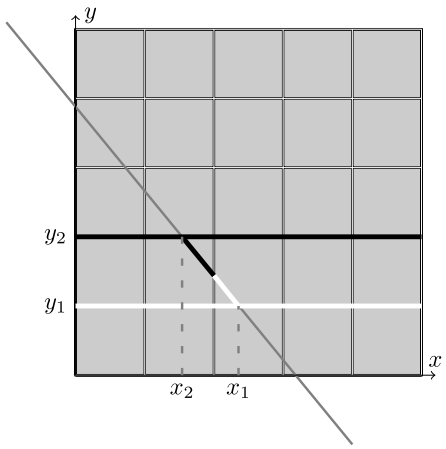

Figure 3. An illustration of the method for finding the intersection lengths. The steep ray (slanted grey line) intersects two pixels in the grid row between y_1 and y_2. The length of the black segment is l_2, the length of the white segment is l_1.

operations for steep rays as the pixel values are read in row-wise order. When the slope of a ray is less than one (flat lines), each ray will intersect at most two pixels per column in the pixel grid. To avoid reading the pixel values in column-wise order for flat rays, we transpose the image and the rays, so the flat rays become steep.

The flat lines are transposed in a preprocessing step. During the preprocessing, we also exploit that the rays are parallel, and calculate the length of intersection between a single pixel and a ray with the given θ. We call this the base length and denote it by l_{base}. In the case where a ray only intersects one pixel in the grid row, the pixel weight will be equal to the base length. In the case where the ray intersects two pixels, the sum of the lengths is equal to the base length, and thus each length can be found by multiplying the base length by the proportion of the difference between the x values lying inside the pixel:

$$l_1 = \left| \frac{x_1 - \lfloor \max(x_1, x_2) \rfloor}{x_1 - x_2} \right| \cdot l_{base}, \tag{4}$$

$$l_2 = \left| \frac{x_2 - \lfloor \max(x_1, x_2) \rfloor}{x_1 - x_2} \right| \cdot l_{base}. \tag{5}$$

This is illustrated in Fig. 3.

For the back-projection we use a similar approach, but interchange the order of the `maps` to perform coalesced writes. The structure then becomes an outer double `map` over the rows, then columns of the grid. Inside these outer `maps`, we do a `reduce` over a `map` of the prepossessed angles. We then estimate which ρ values for the given angle result in a ray that can pass through the given pixel. The implementation is summarized in Fig. 4.

The possible ρ values are estimated in the following manner: If we inscribe the pixel in a circle with radius $\frac{\sqrt{2}}{2}$ and center

```
map (\x_j ->
   map (\y_j ->
        reduce (+) 0.0 (
             map (\θ ->
                  calculate (x, y) by (6) and (7)
                  calculate ρ = cos(θ)x + sin(θ)y
                  calculate s = ⌈(ρ − ρ_0)/δ_ρ⌉
                  calculate m' by (8)

                  in reduce (+) 0.0 <| map(\i ->
                       calculate s' = s + i
                       calculate ρ' = s'δ_rho + ρ_0
                       calculate l_i = l(s', θ, x_j, y_j)
                       get projection value p_i for (θ, s')
                       in l_i · p_i
                  )(0...m)
             ) (lines)
        )
    ) ((-n/2)...(n/2-1))
) ((-n/2)...(n/2-1))
```

Figure 4. A description of the back-projection, which uses two outer `maps` followed by a composition of `reduce` and `map`, for a total of four levels of application parallelism. The innermost nested `reduce` and `map` is simply for convenience as m' might vary but is generally is a very small number (< 10) and hence it is not counted as a level of parallelism. $l(s', \theta, x_j, y_j)$ denotes the intersection length of the ray given by θ and s' and the pixel with lower left corner at (x_j, y_j). The calculations for l_i are equivalent to those mentioned under forward-projection.

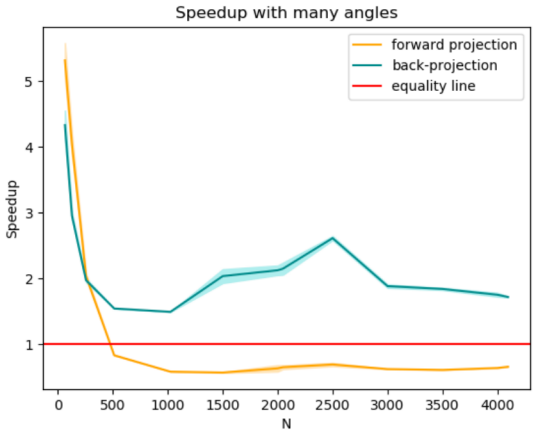

Figure 5. Speedup graphs (higher is better) of our forward-projection and back-projection measured against ASTRAs forward-projection and back-projections.The horizontal line at $y = 1.0$ and the shaded areas behind each graph show the standard deviation. The value of N is varied on the x-axis.

in the center of the pixel, then we can determine the tangent point (x, y) for a ray of angle θ to the circle by:

$$x = x_j + \frac{1}{2} - \frac{\sqrt{2}}{2}\cos(\theta), \tag{6}$$

$$y = y_j + \frac{1}{2} - \frac{\sqrt{2}}{2}\sin(\theta), \tag{7}$$

Where (x_j, y_j) is the bottom left corner of the pixel. From these, we can determine the minimal ρ value by inserting into the line equation. The maximum number of rays that can pass through a single pixel for a given angle is

$$m' = \frac{\sqrt{2}}{2\delta_\rho}, \tag{8}$$

where δ_ρ is the difference between two consecutive rho values. Hence, in our innermost `map` of the back-projection, we map over these ρ values and weigh the projection value for the ray by the intersection length for the pixel. We use the same approach for calculating the intersection length as for the forward-projection, but only use the value within the given pixel, thus ensuring a matched forward and back-projection.

IV. Results

We compared the performance of our implementation of the forward- and back-projections to that of the ASTRA toolbox. To time the ASTRA algorithms we first transferred the data to the GPU via `pygpu` in order not to time the data transfer. For Futhark, we used the built-in benchmarking tools.

We compared the algorithms using synthetic images of random shapes, varying the size of the image and the number of projections. The sizes $N \times N$ were varied from 64×64 pixel images to 4096×4096 pixel images. We chose to use $\lceil \frac{\pi \cdot N}{2} \rceil$ angles and $\lceil \sqrt{2N^2} \rceil$ rays per angle with a spacing of 1.0 pixel between two consecutive rays. We made these choices to mimic the data obtained in a situation where fast analytic reconstruction would be applicable. For the run time tests we included no noise in the images. All reported results are based on the average of 10 runs of the algorithm and run on a GeForce RTX 2080 Ti graphics card.

The results of the test are shown in figure 5. For forward-projection we perform well for minimal problems, but in problems of realistic size, the forward-projection of the ASTRA toolbox is about a factor 1.4 faster. However, in the back-projection case, our implementation is approximately $2\times$ faster for most realistic problems compared to the implementation in ASTRA. The reason for ASTRA outperforming our Futhark implementation in the forward-projection is due to its attention paid to low-level GPU details, particularly exploiting so-called *texture memory*, which is spatially cached, and storing the angles in *constant memory*. The Futhark compiler does not do this.

In our second test, we kept the size N fixed at 1024 pixels, but varied the number of angles between 1 and 100, thus mimicking the sparse reconstruction case where algebraic methods have an advantage in terms of reconstruction quality over fast Fourier based methods.

The results of the sparse angle test are shown in figure 6. It is evident that the forward-projection performs relatively better in the sparse case, as the extra layers of parallelism in our implementation compared to ASTRAs pay off. In the forward-projection, the outer parallelism is reduced because of fewer angles, and exploiting the inner parallelism is very beneficial. Both the forward-projection and back-projection show a speedup between $1.2\times$ and $2\times$ in the sparse case.

For our last test, we measured the run-time of reconstructing

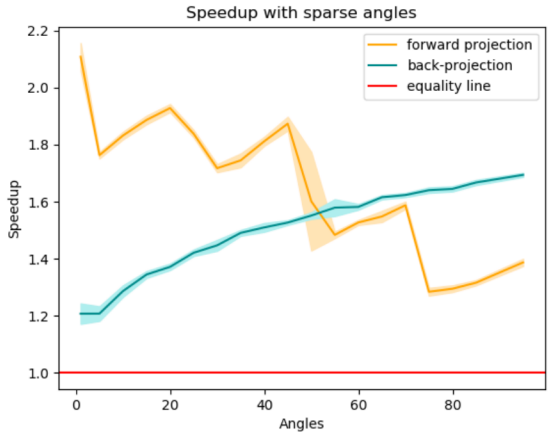

Figure 6. Speedup graphs (higher is better) of our forward-projection and back-projection measured against ASTRAs forward-projection and back-projections for sparse angles. The horizontal line at $y = 1.0$ is equal performance and the shaded areas behind each graph show the standard deviation. The number of angles is varied on the x-axis.

Table I

Hardware	Runtime
Compiled to OpenCL	
Radeon RX Vega 64	622ms
NVIDIA TITAN Xp	642ms
GeForce GTX 780 Ti 1869	1869ms
2 × Intel Xeon E5-2650 CPU	11900ms
Intel(R) HD Graphics Kabylake ULT GT2	22151ms
Compiled to sequential C	
Intel Xeon E5-2620 CPU	15min

Futhark timings of a slice of the Tomopy tooth data set of size 640×640 on different hardware. All results are based on 200 iterations of the algorithm. A reconstruction with ASTRA's SIRT is only possible on the two CUDA cards.

a slice of the Tomopy [21] [22] "tooth.h5" data set from the APS beamline on different hardware, including several devices that ASTRA does not support. To do the reconstruction we used Tomopy for preprocessing, then our Futhark-based algorithms for reconstruction. We tested the reconstruction on different hardware - two CUDA cards, an AMD card, an integrated graphics card in a laptop and an older multi-core CPU. In all cases, we generate code with Futhark's OpenCL backend, without modifying our application code to suit the target better. The results are shown in table IV. Unsurprisingly, the high-end GPUs significantly outperform both executions on dual multicore CPUs as well as on an integrated laptop GPU. However, the difference from fastest to slowest is a mere $\times 35$, suggesting that algorithmic prototyping is viable on low-powered but cheaper and more accessible hardware.

V. Discussion and Conclusions

We have shown that forward- and back-projection can be implemented in a high-level language and perform comparably to a low-level CUDA accelerated implementation. The high-level implementations make use of an inherently more parallel algorithm, which is a benefit in the sparse reconstruction case. Besides being useful in solving problems based on limited data, this also has high importance for utilizing the implementations as subroutines in block algebraic methods, which can achieve faster convergence based on more updates per iteration with few angles [14] per update.

We have shown that we can perform the reconstruction of a slice even on a standard laptop. We have also seen that our forward-projection scales well with the hardware. When we ran our tests on a GeForce GTX 780 Ti, ASTRA was approximately 2.5 times faster on the forward-projection, while on a TITAN Xp card this factor was reduced to 1.4. We suspect that this is due to the superior parallelism in our implementation, and have hopes that this will mean better performance in the future.

This implementation has the potential for making it easy for researchers to prototype new tomographic algorithms on cheap and accessible development hardware, which can then be directly transferred to a high-end computer at a synchrotron facility. Implementing the algorithms in a high-level language is a massive advantage as it allows for a more abstract implementation which is closer to the original mathematical, thus letting researchers focus on new algorithmic tools, instead of time-consuming low-level optimizations. The results are especially promising for developing sparse reconstruction algorithms, block algebraic algorithms, and model-based iterative methods. We plan to extend the code to other geometries and develop a method for reconstructing volumes which can not directly fit in the GPU memory. The code is available for download at https://github.com/tomograph/synkrotomo.

VI. Acknowledgment

MBL was supported by the Capital Region Research Foundation (Grant number: A5657) on the MAX4Imagers project (PI: Tim Dyrby).

References

[1] V. V. Nieuwenhove, J. D. Beenhouwer, J. Vlassenbroeck, M. Brennan, and J. Sijbers. "MoVIT: a tomographic reconstruction framework for 4D-CT". In: Opt. Express 25.16 (Aug. 2017), pp. 19236–19250.

[2] D. Kazantsev, E. Guo, A. B. Phillion, P. J. Withers, and P. D. Lee. "Model-based iterative reconstruction using higher-order regularization of dynamic synchrotron data". In: Measurement Science and Technology 28.9 (Aug. 2017), p. 094004.

[3] M. Burger et al. "A variational reconstruction method for undersampled dynamic x-ray tomography based on physical motion models". In: Inverse Problems 33.12 (Nov. 2017), p. 124008.

[4] B. Keck, H. Hofmann, H. Scherl, M. Kowarschik, and J. Hornegger. “GPU-accelerated SART reconstruction using the CUDA programming environment”. In: Progress in Biomedical Optics and Imaging - Proceedings of SPIE 7258 (Feb. 2009).

[5] W.-M. Pang et al. “Accelerating simultaneous algebraic reconstruction technique with motion compensation using CUDA-enabled GPU.” eng. In: International journal of computer assisted radiology and surgery 6 (2 Mar. 2011), pp. 187–99.

[6] L. Flores, V. Vidal, P. Mayo, F. Escriba, and G. Verdú. “CT image reconstruction based on GPUs”. In: Radiation Physics and Chemistry 95 (Feb. 2014), pp. 247–250.

[7] V. Nguyen and S. Lee. “Parallelizing a Matched Pair of Ray-Tracing Projector and Backprojector for Iterative Cone-Beam CT Reconstruction”. In: IEEE Transactions on Nuclear Science 62.1 (Feb. 2015), pp. 171–181. ISSN: 0018-9499.

[8] X. Jia, B. Dong, Y. Lou, and S. Jiang. “GPU-based Iterative Cone Beam CT Reconstruction Using Tight Frame Regularization”. In: Physics in medicine and biology 56 (July 2011), pp. 3787–807.

[9] M. Leeser, S. Mukherjee, and J. Brock. “Fast reconstruction of 3D volumes from 2D CT projection data with GPUs”. In: BMC Research Notes 7.1 (Aug. 2014), p. 582. ISSN: 1756-0500.

[10] P. Després and X. Jia. “A review of GPU-based medical image reconstruction”. In: Physica Medica 42 (Oct. 2017), pp. 76–92.

[11] W. van Aarle et al. “Fast and flexible X-ray tomography using the ASTRA toolbox”. In: Opt. Express 24.22 (Oct. 2016), pp. 25129–25147.

[12] G. L. Zeng and G. T. Gullberg. “Unmatched projector/backprojector pairs in an iterative reconstruction algorithm”. In: IEEE Transactions on Medical Imaging 19.5 (May 2000), pp. 548–555. ISSN: 0278-0062.

[13] T. Henriksen, N. G. W. Serup, M. Elsman, F. Henglein, and C. E. Oancea. “Futhark: Purely Functional GPU-programming with Nested Parallelism and In-place Array Updates”. In: Proceedings of the 38th ACM SIGPLAN Conference on Programming Language Design and Implementation. PLDI 2017. Barcelona, Spain: ACM, 2017, pp. 556–571. ISBN: 978-1-4503-4988-8.

[14] H. Sørensen and P. Hansen. “Multicore Performance of Block Algebraic Iterative Reconstruction Methods”. English. In: S I A M Journal on Scientific Computing 36.5 (2014), pp. C524–C546. ISSN: 1064-8275.

[15] Y. Long, J. A. Fessler, and J. M. Balter. “3D Forward and Back-Projection for X-Ray CT Using Separable Footprints”. In: IEEE Transactions on Medical Imaging 29.11 (Nov. 2010), pp. 1839–1850. ISSN: 0278-0062.

[16] A. Klöckner et al. “PyCUDA and PyOpenCL: A scripting-based approach to GPU run-time code generation”. In: Parallel Computing 38.3 (2012), pp. 157–174. ISSN: 0167-8191.

[17] T. Henriksen, F. Thorøe, M. Elsman, and C. Oancea. “Incremental Flattening for Nested Data Parallelism”. In: Proceedings of the 24th Symposium on Principles and Practice of Parallel Programming. PPoPP ’19. Washington, District of Columbia: ACM, 2019, pp. 53–67. ISBN: 978-1-4503-6225-2.

[18] D. Matenine, G. Cote, J. Mascolo-Fortin, Y. Goussard, and P. Despres. “System matrix computation vs storage on GPU: A comparative study in cone beam CT.” eng. In: Medical physics 45 (2 Feb. 2018), pp. 579–588.

[19] R. L. Siddon. “Fast calculation of the exact radiological path for a three-dimensional CT array.” eng. In: Medical physics 12 (2 Apr. 1985), pp. 252–5.

[20] H. Gao. “Fast parallel algorithms for the x-ray transform and its adjoint.” eng. In: Medical physics 39 (11 Nov. 2012), pp. 7110–20.

[21] D. Gursoy, F. De Carlo, X. Xiao, and C. Jacobsen. “TomoPy: A framework for the analysis of synchrotron tomographic data”. In: Journal of Synchrotron Radiation 21 (Sept. 2014).

[22] D. M. Pelt et al. “Integration of TomoPy and the ASTRA toolbox for advanced processing and reconstruction of tomographic synchrotron data.” eng. In: Journal of synchrotron radiation 23 (Pt 3 May 2016), pp. 842–9.

4.3 Dynamic Tomography

The motion of living objects is often complicated to arrest, e.g. breathing and heartbeats. As tomographic imaging is often used for medical imaging, e.g. CT-scans, the assumption that the object of interest is static during the scan is problematic and is repeatedly violated for imaging of living samples.

In this section, dynamic tomographic reconstruction approaches will be discussed, where the following setup, which is typical for SXRT, is assumed. The object of interest, *the sample*, is placed on a rotation stage. An X-ray beam passes through the object and hits a detector on the opposite side. The X-rays follow a parallel beam geometry, which is often a good approximation for synchrotron data. The acquisition of each projection takes some amount of time which is called the *exposure time*. During the acquisition, the sample is continuously rotated on the rotation stage. The data collected during a $180°$ rotation is a full sinogram. If only a small wedge of projection angles is used, it is referred to as a limited angle problem.

It is not possible to reconstruct all dynamic objects from their projections, as in the extreme case with no assumptions on the deformations the object could attain, this would be equivalent to being able to reconstruct all objects from a single projection in the case where an object had changed into something completely different between one projection and the next. Essential parameters for the quality of reconstruction are 1) the motion of the object, 2) the set of projection angles, 3) the spatial resolution of each projection, and 4) the physical features of the object. For some types of dynamics, static reconstruction methods are applicable without any modification. If the object moves in a stop motion fashion and a full sinogram can be captured for each frame, naturally, each frame may be reconstructed separately. The same applies if the motion is periodic, except that the projections need to be reordered. The approach for periodic motion is called gating and has been used with success for different applications, including reconstructing blowfly flight motor dynamics, [40, 27] and medical CT imaging of the heart and lungs [31, 42].

Assuming that the object does not move periodically or in a stop motion, the quality of the reconstruction will suffer, even for small amounts of motion. The reconstruction method is based on a back-projection step in filtered back

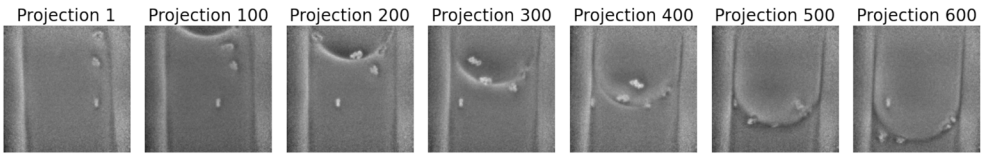

Figure 4.8.: Projections of moving gold nanoparticles in paraffin oil

projection and algebraic reconstruction. Assume the object is static, then during the back-projection, all the projection values of a particular point will intersect. Assume instead that the point moved slowly in one direction during the acquisition. Then the lines will no longer intersect in a single point. Thus, static reconstructions of dynamic objects appear smeared. Furthermore, the error from the movement is not only localized to the moving object itself in the reconstruction but is smeared to the whole 2D strip the object passes through. Essentially, the back-projection of a relocated point will instead intersect with the back-projection of another point, causing errors widely in the reconstruction and not only locally for the moving object.

In the following sections, approaches to dynamic tomography which go beyond reconstruction of periodic or stop motion objects will be explored. The section is structured as follows. First, some reconstructions of a dynamic data set acquired at the TOMCAT Nanoscope, PSI, are shown to clarify the challenges faced when working with real dynamic data. Then some theoretical results are shown using different phantoms and approaches to dynamic tomography.

4.3.1 Dynamic SXRT data

During a visit to the TOMCAT beamline, PSI, a dynamic SXRT dataset was collected. The sample consisted of gold nanoparticles in paraffin oil inside a Ø50 μm glass capillary. During the acquisition, the oil ran out the bottom of the capillary. The projection data showed five particles. One was static, and five were falling with the oil. The edges of the capillary, the particles and the oil meniscus are all visible in the projections; see Figure 4.8. The capillary walls appear as vertical lines in the projections, the meniscus is the parabola at the top of the projections, and the particles appear as five bright blobs inside the capillary. One of the particles is stuck to the side of the glass. Three particles are visible from the beginning, and the rest appear with the

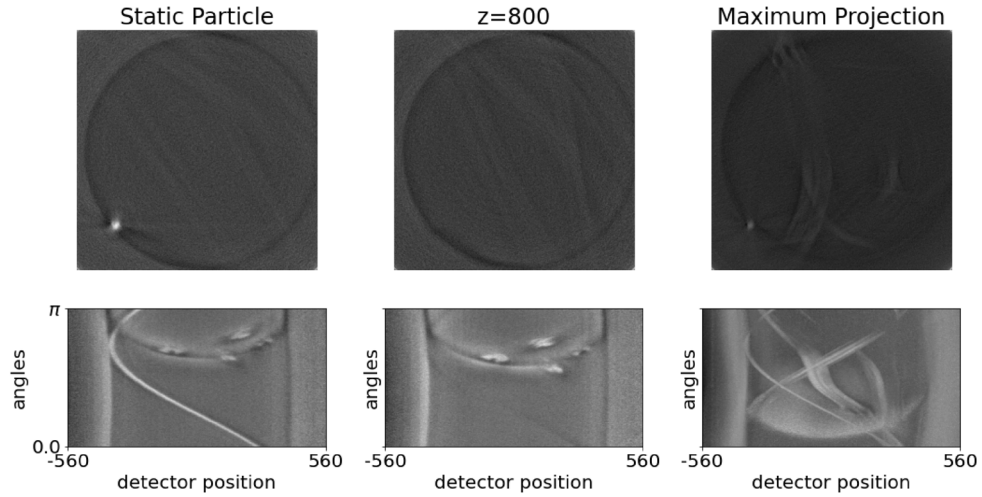

Figure 4.9.: **Gold Particles** On the left, the sinogram and the corresponding FBP reconstruction of a slice containing the static gold nanoparticle are shown. The sinogram and corresponding FBP reconstruction of a z-slice for $z = 800$ with no static particles are shown in the middle. The sinogram and reconstruction generated by taking the maximum projection are shown on the right. It is clear that the static particle on the left can be reconstructed, while in the slice for $z = 800$, only the ring of the capillary, which is static, can be seen. The reconstruction is still not good when taking the maximum projection, and obtaining exact (x, y) coordinates is impossible. However, it is possible to discern five higher intensity smears, consistent with five moving particles in the data.

meniscus. The data were acquired during 180° continuous rotation, with a 80 ms exposure time.

Three initial reconstructions were made, clearly showing the artefacts that appear when reconstructing dynamic data with the classical FBP algorithm. The results are shown in Figure 4.9. The one static particle can be reconstructed and appears to be stuck to the inside of the capillary. When reconstructing a z-slice through the capillary, which the particles flow through but which contains no static elements other than the capillary, only the capillary ring can be identified. Through the ring is white smears which are the artefacts from the moving particles. The last reconstruction is based on the assumption that the only movement the particles make is flowing downwards. By taking the maximal projection of the projections in the vertical directions, it could be possible to obtain the sinogram corresponding to the horizontal location of the particles and hence reconstruct a top projection of the tube. The sinogram looks much more as expected by this approach, i.e., the particles forming vertical sine curves. In the reconstruction five-light smear can be seen corresponding to the five particles. However, it is still not possible to locate the particles.

The gold particle data clearly shows that using static reconstruction methods based on back-projection, such as FBP, causes smears in the reconstruction as expected.

One could consider dividing the projection data into sections by applying a windowing function and reconstructing a frame from each window. Multiple angles would be available for each frame, and there would be less movement. However, only a small wedge of angles would be available because of the sequential acquisition. This type of problem is a limited angle problem, and microlocal analysis has shown that these problems have inherent issues [18]. Essentially only those singularities which are parallel to the X-rays can be reconstructed.

4.3.2 TV Regularization in Time

A natural idea for improving the reconstruction quality of dynamic data is applying regularization in the time direction [29]. To test this idea experi-

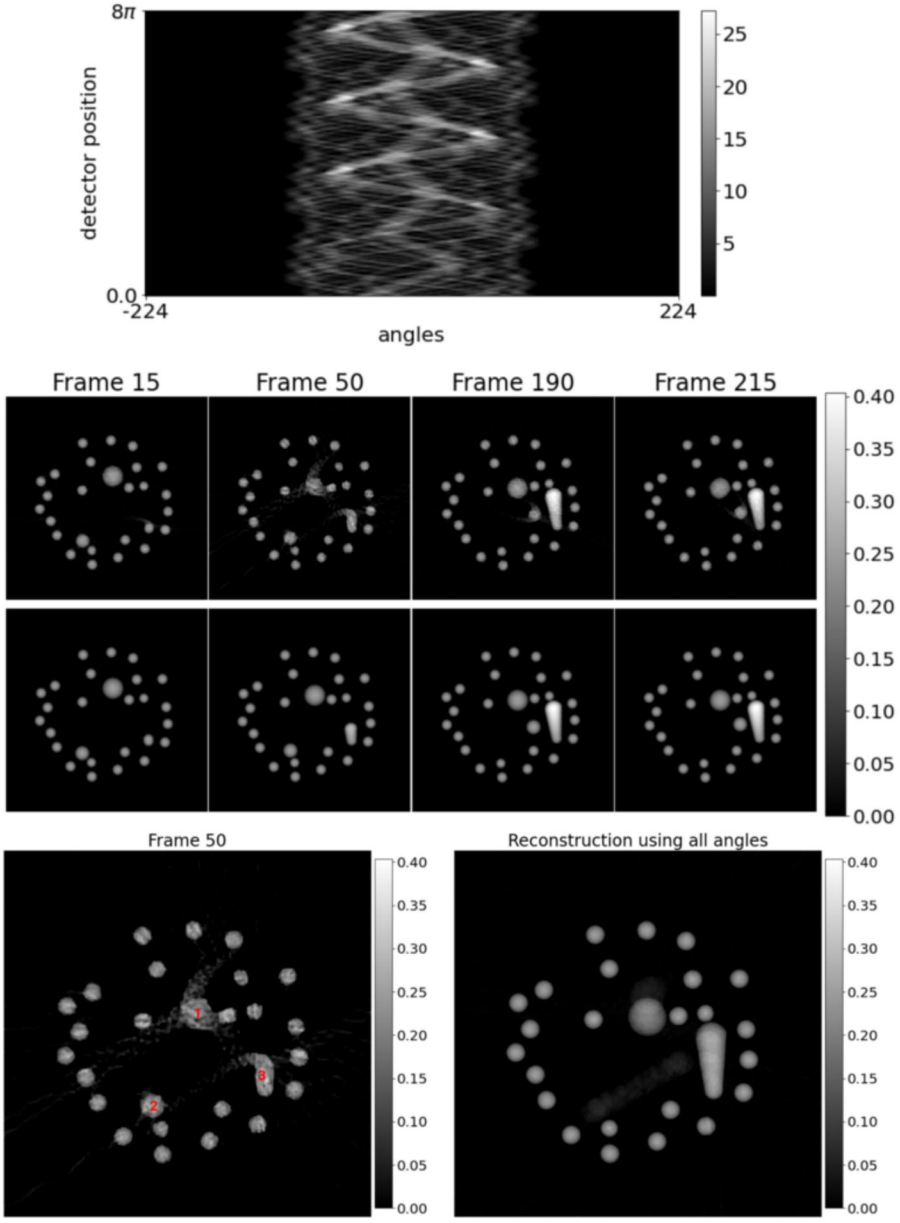

Figure 4.10.: **Dynamic Blender Phantom** On the top, the sinogram used in the reconstructions is shown. The TV reconstructions are shown in the middle. The first row contains the reconstructions, and the ground truth is in the second row. On the bottom, the left image is a close up of the reconstruction of frame 50. The particles numbered in red are moving. The particle labelled "1" moves rapidly between frames 40 and 60. The particle labelled "2" moves during the entire acquisition, speeding up. The particle labelled "3" expands upwards from frame 1 to 120. All other particles, such as the one indicated by the green arrow, are static. The reconstruction on the bottom right is based on using all 240 angles.

mentally, a phantom, which was similar to the data presented [29], consisting of several spheres, was created, see Figure 4.10. The phantom was created using Blender, a free and open-source 3D computer graphics tool-set. The built-in ray casting of Blender was used through a python script[2] to simulate the projection data. The simulated data has 448 detector positions and 240 projections recorded during a total rotation of 8π, giving 30 projection angles for each complete sinogram. There are three moving particles, labelled 1-3 in the phantom. "1" moves fast during a short time interval, "2" moves during the entire acquisition and "3" expands upwards during the first half of the acquisition. The rest of the particles are static. A reconstruction of frame "50" where the rapid particle "1" is moving shows reconstruction errors in both the static and dynamic particles as expected. When the reconstruction is based on all 240 angles, the particle which moves during the whole acquisition becomes almost invisible. The artefacts in all other particles are practically gone.

For unknown reasons, obtaining meaningful reconstructions from the code included with the original article [29] was never successful, though the method worked as published on the data included with the code. Therefore, a simpler implementation was made[3], using the ODL framework [4] to solve the optimization problem presented in [29]:

$$\boldsymbol{f}_{\text{opt}} = \underset{\boldsymbol{f}}{\operatorname{argmin}} \left\{ \|\boldsymbol{A}\boldsymbol{f} - \boldsymbol{p}\|_2^2 + \lambda_1 \|\nabla_{\lambda_2} \boldsymbol{f}\|_{2,1} \right\} \tag{4.5}$$

with

$$\lambda_1 \|\nabla_{\lambda_2} \boldsymbol{f}\|_{2,1} = \lambda_1 \left\| \sqrt{\left(\frac{\delta f}{\delta x}\right)^2 + \left(\frac{\delta f}{\delta y}\right)^2 + \lambda_2 \left(\frac{\delta f}{\delta t}\right)^2} \right\|_1 \tag{4.6}$$

The reconstruction in Figure 4.11 shows the reconstructions of the blender phantom with varying λ_2 levels for frame 50, where the rapid particle "1" is moving fast. The reconstructions and ground truth have been thresholded

[2]The script and details for running the X-ray simulation can be found on GitHub `git@github.com:tomograph/PhantomGenerator.git`
[3]https://github.com/tomograph/DynamicExplore.git
[4]https://github.com/odlgroup/odl.git

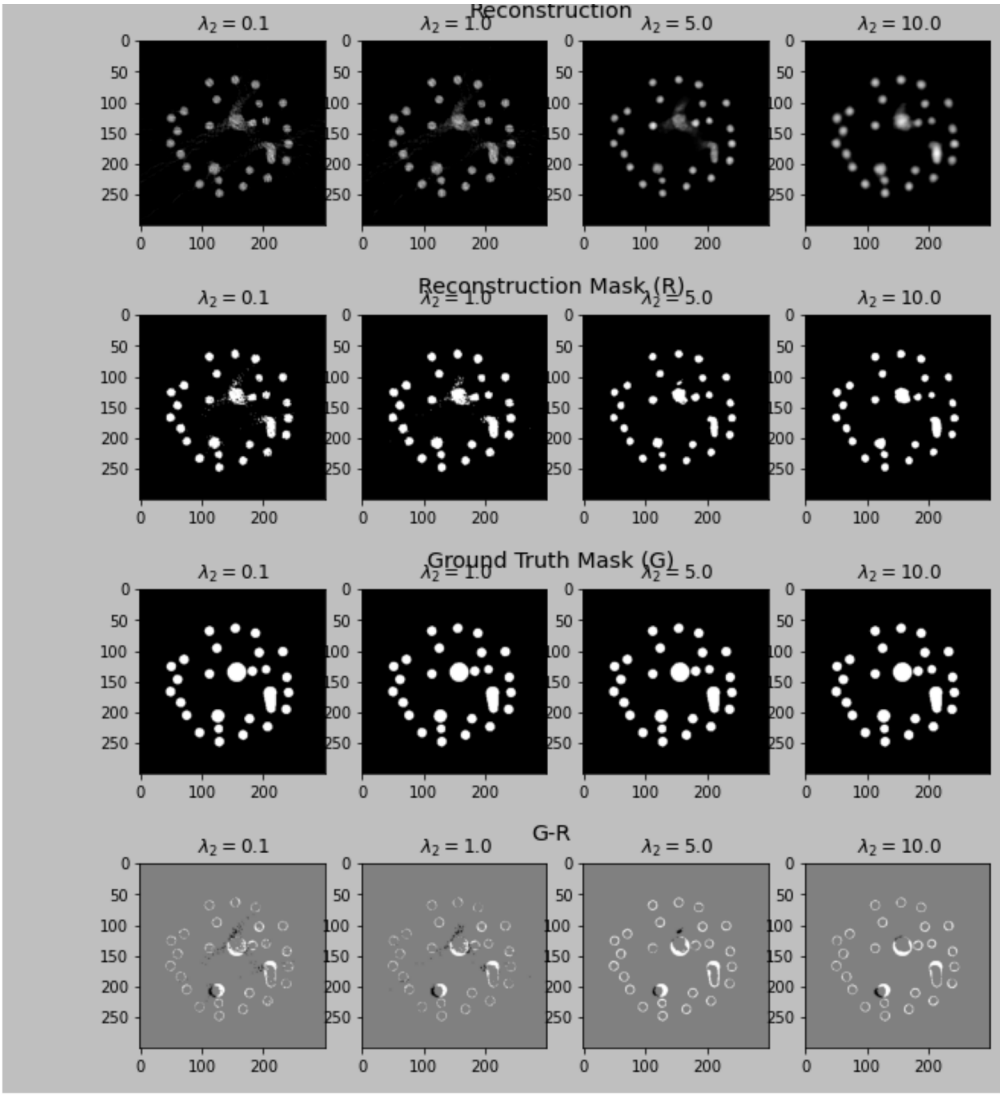

Figure 4.11.: **Reconstruction using TV-regularization in the time direction** Top row: A reconstruction of frame 50 of the phantom in Figure 4.10 using TV-regularization in the time direction. Second row: Mask of top row. Third row: Mask of ground truth. Bottom row: The difference between row two and row three. In each row four images are shown, one for each λ_2 in $\{0.1, 1.0, 5.0, 10.0\}$.

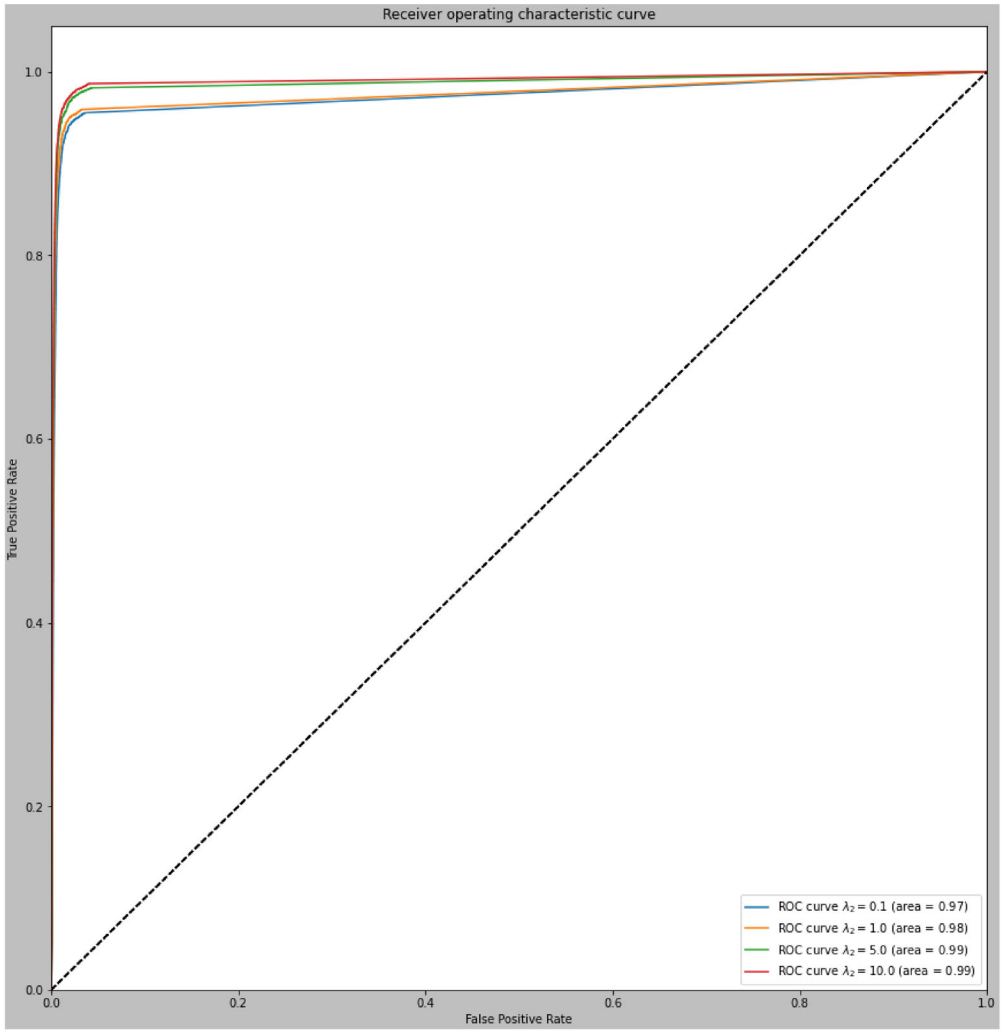

Figure 4.12.: Receiver operating characteristic curve The plot shows the receiver operating characteristic curve for the reconstruction shown in Figure 4.11. The area under the curve is growing with increasinghttps://www.overleaf.com/project/60f6825581b2f372f536c0a1 values of the regularization parameter λ_2.

Figure 4.13.: A reconstruction of the dynamic gold particle data set described in Section 4.3.1 using TV-regularization in the time direction with $\lambda_2 = 10.0$ and a window size of 5 angles. Window size of 40, 100 and 300 were tried with very little difference. Values of 1, 10 and 100 were tried for λ_2, also with very little effect.

to obtain a mask. In figure 4.12 the receiver operating characteristic curve of the reconstruction is displayed. The area under the curve increases with increasing values of λ_2 indicating that the regularization parameter suppresses the motion artifacts.

However, the data was based on eight rotations with thirty angles per rotation. Much data is required for reconstruction, and if only $180°$ of data is available such as for the nanoparticle data in Figure 4.9, the reconstruction for each frame becomes a limited angle problem, and the reconstruction suffers from limited-angle artefacts, see Figure 4.13.

4.3.3 Joint Reconstruction and Motion Estimation via Optical flows

Optical flow is a popular method for estimating the motion between two images. The dynamic reconstruction method described in [8] incorporates an optical flow estimate $\boldsymbol{v}$ into the standard TV-reconstruction approach. The procedure iteratively performs a TV-minimization step using a warping operator based on the optical flow estimate and refines the flow based on the reconstructions. The TV-minimization step, which includes the optical flow $\boldsymbol{v}$ is formulated as:

$$\boldsymbol{f}_{\text{opt}} = \underset{\boldsymbol{f}}{\operatorname{argmin}} \left\{ \|\boldsymbol{A}\boldsymbol{f} - \boldsymbol{p}\|_2^2 + \lambda_{TV} \|\nabla \boldsymbol{f}\|_{2,1} + \lambda_{flow} \sum_{t=1}^{N_t-1} \left\| \boldsymbol{f}_{t+1} - \boldsymbol{f}_t + \nabla \boldsymbol{f}_t \cdot \boldsymbol{v} \right\|_1 \right\}.$$

The authors use a primal-dual method [9] for both reconstruction and estimating the flow. Unfortunately, the code for their algorithm was not available, and hence a new implementation was made. For the implementation of the reconstruction step, the primal-dual approach described in the original article was used, but for motion estimation, a more accurate and fast method was used [7, 21][5]. For the forward-and back-projections, sequential ASTRA tool-

[5]The implementation of the optical flow method that was used can be found here `https://github.com/pathak22/pyflow.git`

box implementations are used [1, 2, 30]. The implementation was made in collaboration with Jakeoung Koo.

The implementation was first tested on a phantom where a disc translates across the image. For this phantom, the inclusion of the optical flow constraint improved the reconstruction considerably, see Figure 4.14, which shows a reconstruction of a disc phantom that translates to the right. Similar to the original article, it was found that the method performs best when random angles are used and not sequential angles, as is custom for SXRT. See Figure 4.15. Furthermore, for the disc phantom, almost perfect reconstructions can be obtained by adding just a single static angle to the reconstruction of each frame, see Figure 4.16.

However, looking at the two-angle TV reconstruction in Figure 4.16 compared to the TV reconstruction in Figure 4.15, it is also evident that the good results are also in large part due to the simplicity of the phantom. From the optical flow estimation assumptions, it is also clear that the translating disc is an optimal phantom to yield good results from the optical flow estimation. Not only does the phantom itself perfectly fit the assumptions, but a simple back-projection will also almost satisfy the assumptions since the projections of the disc are rotation invariant. The difference between the phantoms is illustrated in Figure 4.17. This problem also gives a natural practical solution for improving objects such as the fat curve object. If high-intensity dots were added to the object, such as adding nanoparticles to sperm cells as described in Chapter 2 then these could guide the optical flow estimations. A result of this approach can be seen in Figure 4.19.

One downside to the joint reconstruction and motion estimation method based on optical flows is that it requires many parameters to be tuned, i.e. finding the best parameters for the optical flow estimation and the right weight for the optical flow and TV constraints. A limited number of parameters were tested, and in the end $\lambda_{flow} = 0.5$ and $\lambda_{TV} = 0.1$ were chosen, by trying $0.0001, 0.001, 0.01, 0.05, 0.1, 0.2, 0.3, 0.5$ for both parameters. For the optical flow estimation, the parameters found in the demo of the optical flow implementation[6] were used. The same parameters were chosen for all tests, as these seemed to produce the most robust results.

[6] `https://github.com/pathak22/pyflow.git`

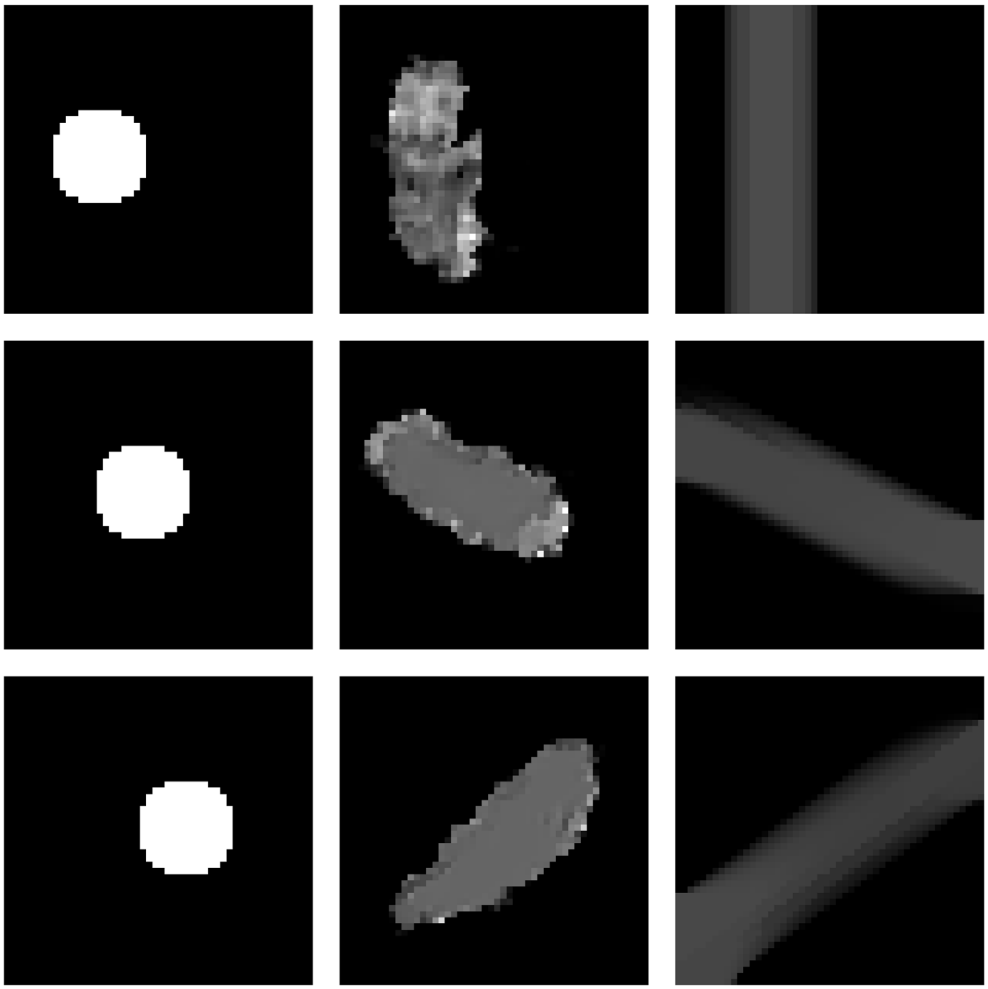

Figure 4.14.: The reconstruction results using the method in [8] of a disc phantom translating to the right, using 20 evenly spaced sequential angles from 0 to π. The left column is the ground truth, the middle column is the reconstruction including the optical flow constraint, and the right column is the regular TV reconstruction.

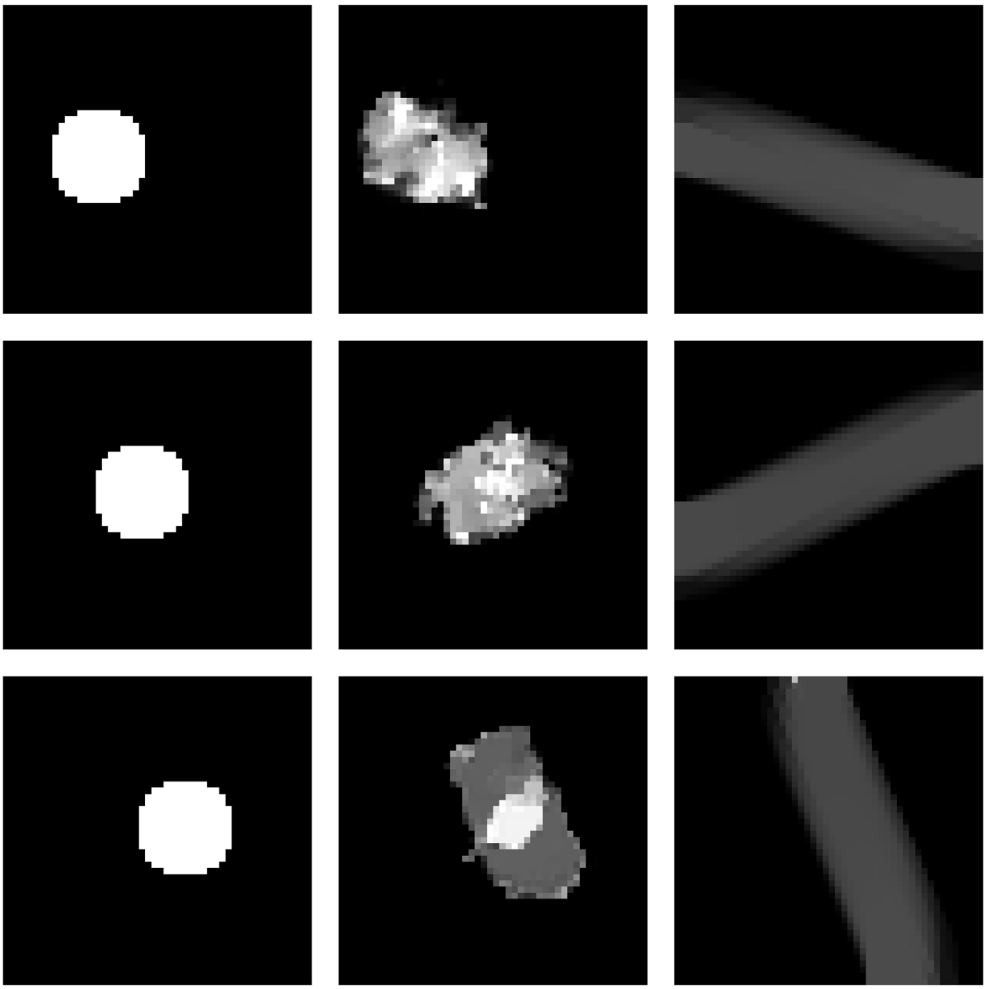

Figure 4.15.: The reconstruction results using the method in [8] of disc phantom translating to the right, using one random angle per frame. The left column is the ground truth, the middle column is the reconstruction including the optical flow constraint, and the right column is the regular TV reconstruction.

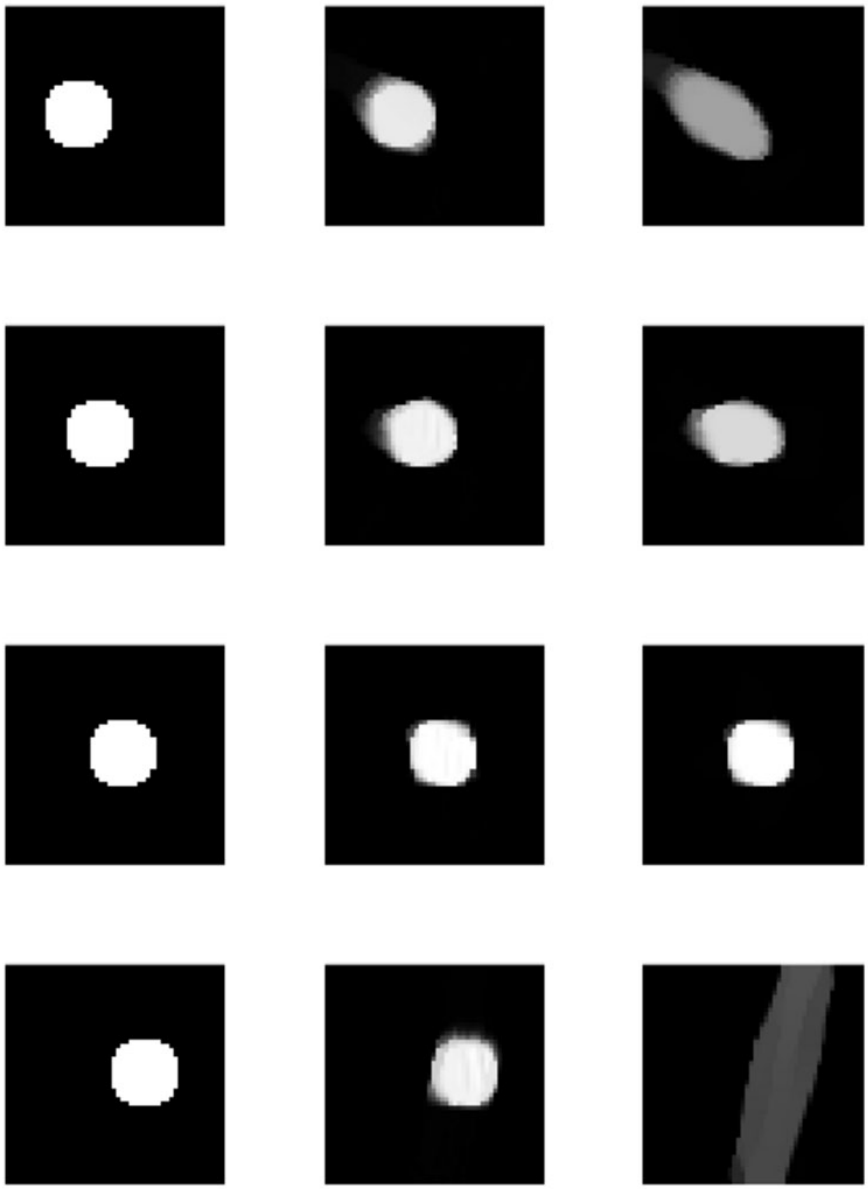

Figure 4.16.: Some reconstruction results using the method in [8]. The phantom is a white disc moving from left to right. The left column is ground truth. The middle column contains reconstructions via the optical flow algorithm, with two static projections per frame. The last column is a total variation reconstruction. The total variation parameter used was 0.3, and for the flow, the weight was 0.05. The same angles were used for the plain TV reconstruction and the reconstruction with the optical flow constraint. From top to bottom are frames 3, 8, 13 and 18. For this phantom, the flow implementation seems to make a considerable improvement. Especially for frames 3 and 18.

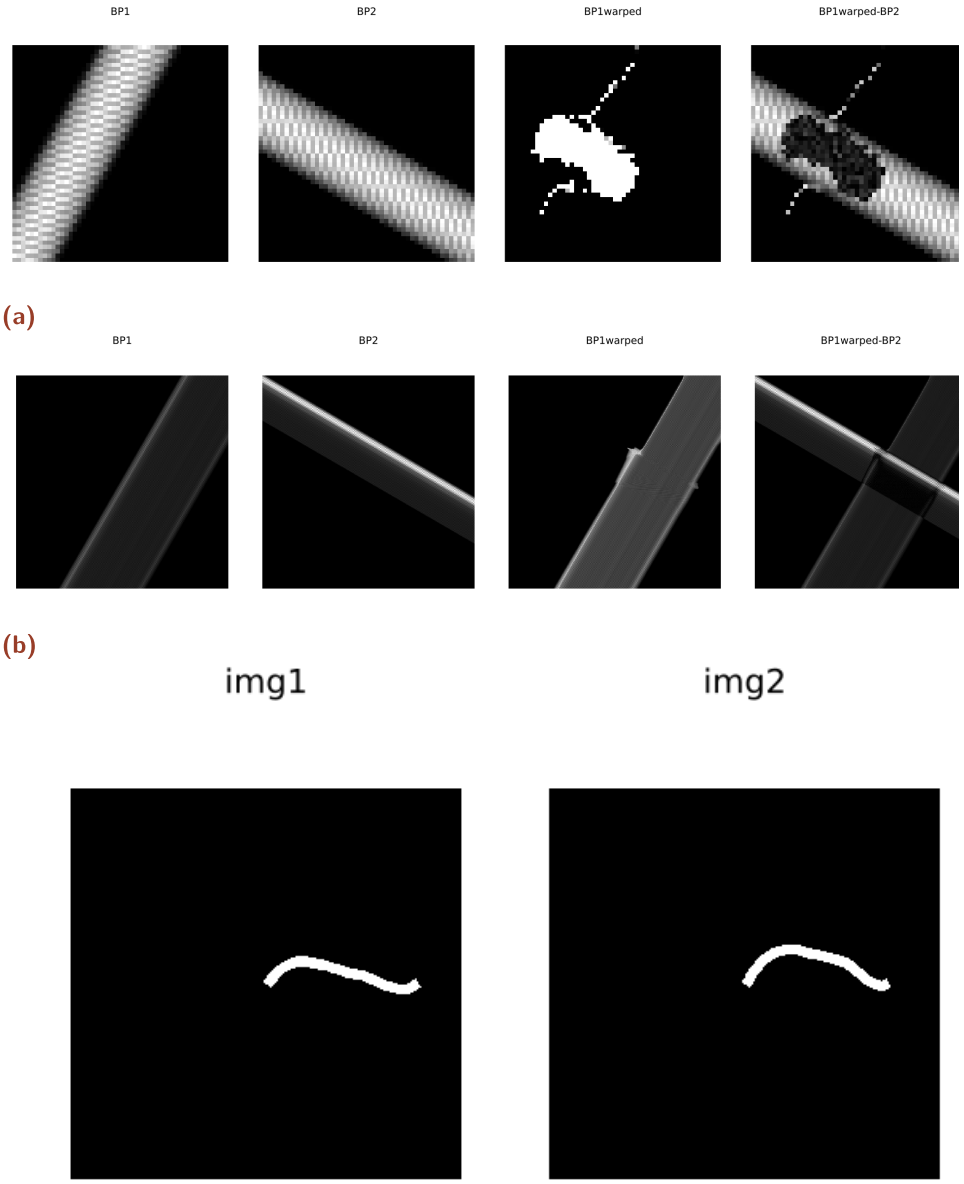

Figure 4.17.: Warping of back-projection of disc vs. fat curve phantom (a) From left to right the back-projection of the first projection (BP1) of the dynamic disc phantom is shown, followed by the second projection (BP2), i.e. another angle view of the second frame. The third image in the row shows the second back-projection warped by the estimated flow (BP1Warped). The final image shows the difference between the warped image and the first image (BP1Warped-BP2). (b) The same as (a) but for the fat curve phantom described in the previous section on sparse reconstructions, but altered to be 2 ms apart. (c) The phantom used in (b). The disc phantom was a 50×50 pixel image. The detector was 70 pixels wide.

(a) Ground Truth

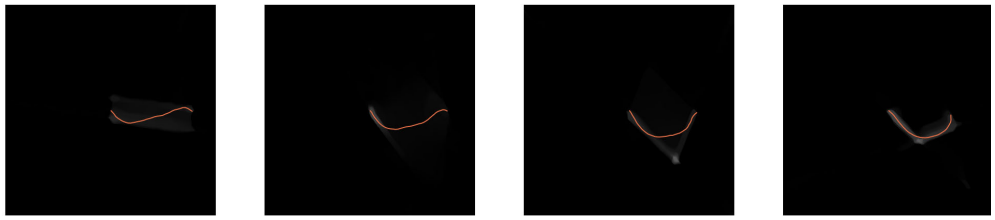

(b) Total Variation Reconstruction

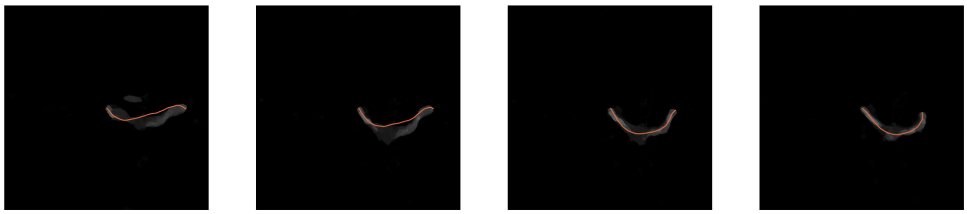

(c) Total Variation with Optical Flow Constraint

Figure 4.18.: Joint motion estimation and reconstruction results for the sperm phantom (a) Ground truth. (b) Plain TV reconstruction. (c) TV with optical flow constraint. The sperm phantom was used with a sampling interval of 2 ms.

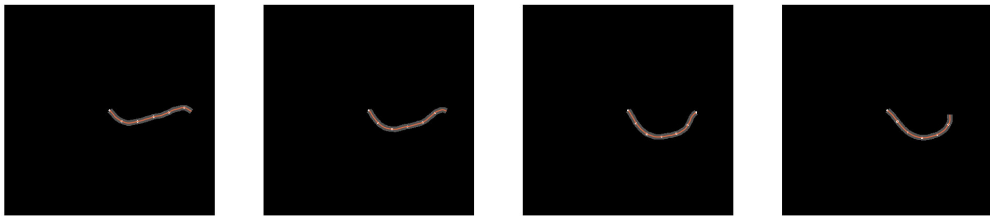

(a) Ground Truth

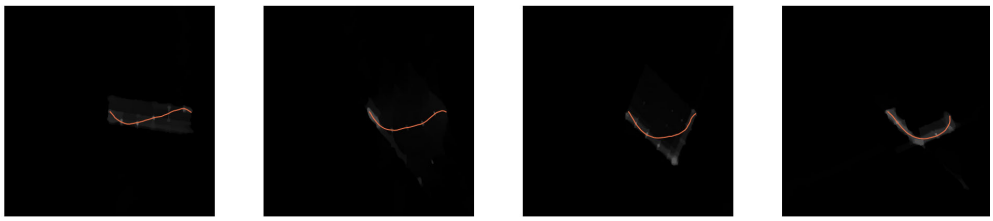

(b) Total Variation Reconstruction

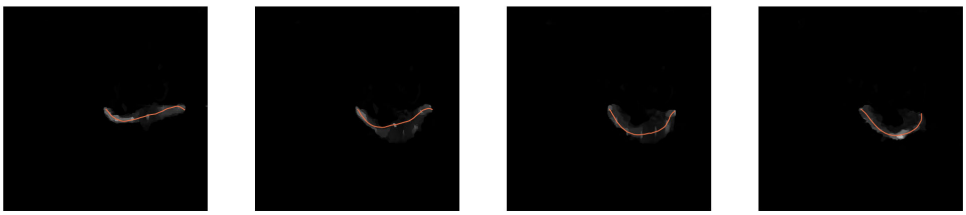

(c) Optical Flow Reconstruction

Figure 4.19.: Effect of adding high intensity particles (a) Shows the ground truth sperm tail phantom described in Section 4.2.1 with the centerlines marked in red. The frames going from left to right are 2 ms apart. High intensity dots have been added to the center line, to simulate the effect of adding high intensity nanoparticles as a contrast agent to sperm tails.(b) A TV-reconstruction of the phantom using 3 static projections pr. frame. (c) A reconstruction using joint motion estimation and reconstrution. The flow causes the high intensity regions to align with the centerline. This figure should be compared to Figure 4.18, where no particles were added to the phantom. The fat curve phantom has an intensity of 1. The particles have an intensity of 3. The intensity values shown are scaled by a factor $\frac{1}{3}$ to be able to distinguish the particles and curve from each other.

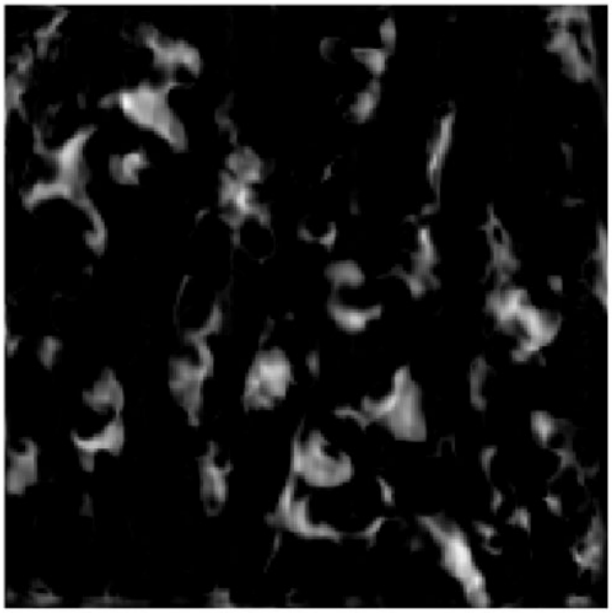

Figure 4.20.: Optical flow reconstruction of the gold nanoparticle data. A reconstruction gone wrong of the nanoparticle dataset described in Section 4.3.1. The reconstruction is made using the maximum projection sinogram in Figure 4.9. While the motion artifacts are obvious in the FBP reconstruction, and the motion objects simply disappear, the high regularization of the optical flow algorithm results in a reconstruction in which non-existent objects appear in the reconstruction instead.

The implementation of the method was slow and could benefit from using the parallel versions of the forward and back-projections, which would also enable more parameters to be tested. Overall, the limited tests show that the method has much potential for dynamic reconstructions and that labelling with nanoparticles could be a promising method for increasing the quality of reconstructions with this method.

Unfortunately, when testing on the real dynamic dataset of gold nanoparticles, described in Section 4.3.1, it was not possible to find any parameters which gave a decent reconstruction, and when looking at the reconstruction in Figure 4.18 and Figure 4.20 it also becomes clear that the method has another major drawback. While dynamic objects are clearly smeared in regular static FBP reconstructions and therefore easily recognized, it is easy to over-regularize the reconstruction with the optical flow constraint. Examples of over-regularized TV reconstructions with the optical flow constraint are shown in Figure 4.18, where the last sperm tail pose seems to propagate to previous frames, and in Figure 4.20, which is not a correct reconstruction of the nanoparticle dataset described in Section 4.3.1.

4.3.4 Perspectives

The joint motion estimation and reconstruction algorithm provide good results when the motion is properly estimated in the optical flow step. It has been shown that if the motion of the object is diffeomorphic and known, and some properties of microlocal analysis are satisfied, i.e. all singularities are detected in the data, then good dynamic reconstructions can be made even with the fast FBP algorithm [13]. In essence, if the motion is diffeomorphic and known, the forward problem can be reformulated so that the projections no longer occur along straight lines but along curved paths. By back-projecting along the same curved paths, it is possible to obtain superior reconstructions. In practice, this has applied with success for motion compensation in [33], where the motion between two frames is first estimated using optical flows, and then the reconstruction is improved by back-projecting along the curved paths corresponding to the estimate. However, this approach requires that the initial reconstructions are rather good.

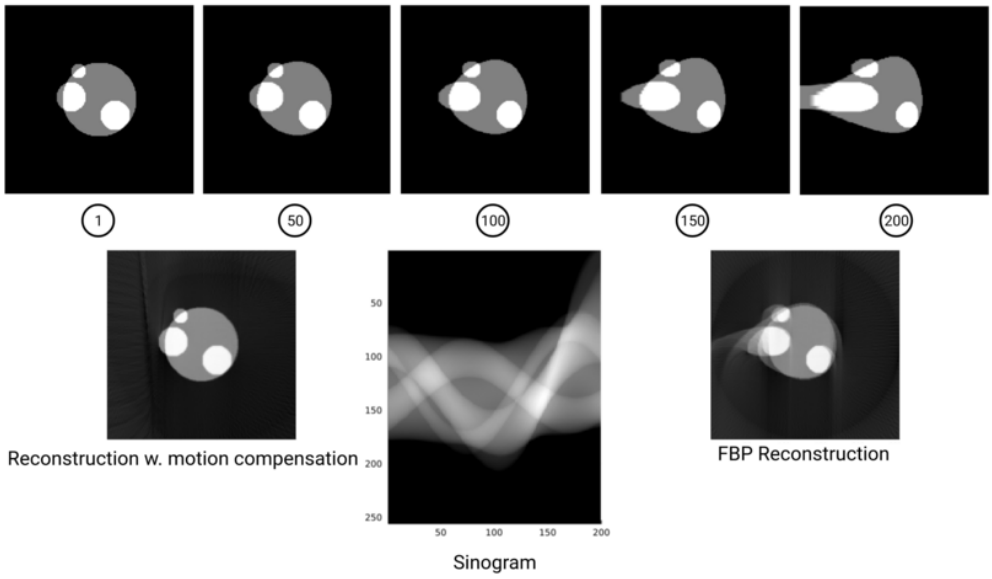

Figure 4.21.: **FBP along curved paths** The top row shows the dynamic phantom over 200 frames. Below in the middle is the sinogram resulting from 200 projections, one for each frame, turning a total of $180°$ degrees. On the left is a reconstruction from an implementation based on the method of FBP along curved paths presented in [13]. On the right is the corresponding FBP reconstruction.

For affine deformations, approaches have been proposed for estimating the deformation from the projection data and applied in practice, such as reconstructing the rising of baked goods [38]. For non-linear dynamics, a similar approach based on estimating the motion from the sinogram has been proposed [14]. The method relies on estimating the motion from high-intensity nodal points in the sinogram.

For large deformations such as sperm tail beating, motion estimation via nodal points such as nanoparticles attached to the tails could be a promising approach, ideally coupled with a motion model as a prior for the estimation.

5 Discussion and Conclusion

The main research question studied in this thesis was:

Can Synchrotron X-ray tomography (SXRT) be used for reconstructing the dynamic tail beating pattern of living sperm in 3D?

To answer this question three sub-questions were explored, and the main findings to each of these will be stated below

How can we obtain a signal from a moving sperm in a synchrotron?

Iron oxide nano particles are a promising staining technique for synchrotron imaging of sperm at high energies. The particles are non-toxic to the cells, and provide enhanced contrast during high-energy synchrotron imaging.

Can the sperm survive the beam?

It seems highly improbable that the TOMCAT nanoscope can be used for dynamic imaging of sperm without any further development to protect the sperm from radiation damage. While the membrane of the sperm stays intact during extended exposure to the beam, the motility of the sperm is affected within minutes at a reduced dose. However, a practical approach based on observing the effect of the beam on the cells has been developed, and could be used to test future approaches to synchrotron imaging of live sperm.

What are the possibilities and limitations of dynamic tomography?

Dynamic tomographic reconstruction is possible for stop motion, periodic, and affine motion, or known diffeomorphic deformations. Sperm are a challenging object to reconstruct due to their fast and complex dynamics, and their long slim shape. If multi-projection setups with the field of view

and spatio-temporal resolution needed to see sperm were developed, sparse reconstruction methods could be used. If multiple projections are not available, adding high contrast markers such as nanoparticles can be useful for motion estimation and dynamic reconstruction.

It is possible that synchrotron x-ray tomography can be used for reconstructing the dynamic tail beating pattern of sperm in the future. The non-toxic labelling method with iron oxide nanoparticles, is a step towards obtaining enough contrast, without affecting their tail-beating pattern prior to imaging. However, for a successful synchrotron acquisition a method for containing the sperm within the field-of-view must be developed, and new approaches to protecting their function during acquisition must be found. If data can be acquired, the most promising approach for reconstruction was found to be sparse reconstruction from multiple projections acquired at once, or good estimates of the sperm dynamics to compensate for the motion.

[3]

Bibliography

6

[1] Wim van Aarle, Willem Jan Palenstijn, Jeroen Cant, Eline Janssens, Folkert Bleichrodt, Andrei Dabravolski, Jan De Beenhouwer, K. Joost Batenburg, and Jan Sijbers. „Fast and flexible X-ray tomography using the ASTRA toolbox“. In: *Optics Express* 24.22 (2016), p. 25129.

[2] Wim van Aarle, Willem Jan Palenstijn, Jan De Beenhouwer, Thomas Altantzis, Sara Bals, K. Joost Batenburg, and Jan Sijbers. „The ASTRA Toolbox: A platform for advanced algorithm development in electron tomography“. In: *Ultramicroscopy* 157.2015 (2015), pp. 35–47.

[3] Chikit Au. „A simple algorithm for medial axis transform computation“. In: *Engineering with Computers* 29.2 (2013), pp. 139–149.

[4] Tom Baden, Andre Maia Chagas, Greg Gage, Timothy Marzullo, Lucia L. Prieto-Godino, and Thomas Euler. „Open Labware: 3-D Printing Your Own Lab Equipment“. In: *PLOS Biology* 13.3 (Mar. 2015).

[5] S. Ben-David Makhluf, R. Arnon, C. R. Patra, D. Mukhopadhyay, A. Gedanken, P. Mukherjee, and H. Breitbart. „Labeling of sperm cells via the spontaneous penetration of Eu3+ ions as nanoparticles complexed with PVA or PVP“. In: *Journal of Physical Chemistry C* 112.33 (Aug. 2008), pp. 12801–12807.

[6] Matteo Bernardello, Radoslaw J. Gora, Patrick Van Hage, Gustavo Castro-Olvera, Emilio J. Gualda, Marcel J. M. Schaaf, and Pablo Loza-Alvarez. „Analysis of intracellular protein dynamics in living zebrafish embryos using light-sheet fluorescence single-molecule microscopy“. In: *Biomedical Optics Express* 12.10 (2021), p. 6205.

[7] Thomas Brox, Nils Papenberg, and Joachim Weickert. „High Accuracy Optical Flow Estimation based on warping - presentation“. In: *Lecture Notes in Computer Science (including subseries Lecture Notes in Artificial Intelligence and Lecture Notes in Bioinformatics)* 3024.May (2014), pp. 25–36.

[8] Martin Burger, Hendrik Dirks, Lena Frerking, Andreas Hauptmann, Tapio Helin, and Samuli Siltanen. „A variational reconstruction method for undersampled dynamic x-ray tomography based on physical motion models“. In: *Inverse Problems* 33.12 (Dec. 2017), p. 124008.

[9] Antonin Chambolle and Thomas Pock. „A First-Order Primal-Dual Algorithm for Convex Problems with Applications to Imaging“. In: *Journal of Mathematical Imaging and Vision* 40.1 (May 2011), pp. 120–145.

[10] Vedrana Andersen Dahl, Anders Bjorholm Dahl, and Per Christian Hansen. „Computing segmentations directly from x-ray projection data via parametric deformable curves“. In: *Measurement Science and Technology* 29.1 (2018).

[11] Ming Du and Chris Jacobsen. „Relative merits and limiting factors for x-ray and electron microscopy of thick, hydrated organic materials“. In: *Ultramicroscopy* 184 (Jan. 2018), pp. 293–309.

[12] L. A. Feldkamp, L. C. Davis, and J. W. Kress. „Practical cone-beam algorithm“. In: *Journal of the Optical Society of America A* 1.6 (June 1984), p. 612.

[13] B N Hahn and M-L Kienle Garrido. „An efficient reconstruction approach for a class of dynamic imaging operators“. In: *Inverse Problems* 35.9 (Sept. 2019), p. 094005.

[14] Bernadette N. Hahn. „Motion Estimation and Compensation Strategies in Dynamic Computerized Tomography“. In: *Sensing and Imaging* 18.1 (2017), pp. 1–20.

[15] P C Hansen and J H Jørgensen. „Total Variation and Tomographic Imaging from Projections“. In: *Proceedings of WSC 2011, Conference of the Dutch-Flemish Numerical Analysis Communities, Woudschouten (Invited conference contribution)* October (2011), pp. 44–51.

[16] G T Herman and R Davidi. „Image reconstruction from a small number of projections“. In: *Inverse Problems* 24.4 (Aug. 2008), p. 045011.

[17] Jakeoung Koo, Anders Bjorholm Dahl, and Vedrana Anderson Dahl. „A Direct Segmentation Method from Projections via Deformable Mesh“. In: 14.8 (2019), pp. 1–12.

[18] Venkateswaran P. Krishnan and Eric Todd Quinto. „Microlocal analysis in tomography“. In: *Handbook of Mathematical Methods in Imaging: Volume 1, Second Edition* (2015), pp. 847–902.

[19] G Kroemer, L Galluzzi, P Vandenabeele, *et al.* „Classification of cell death: recommendations of the Nomenclature Committee on Cell Death 2009“. In: *Cell Death & Differentiation* 16.1 (Jan. 2009), pp. 3–11.

[20] L. Landweber. „An Iteration Formula for Fredholm Integral Equations of the First Kind“. In: *American Journal of Mathematics* 73.3 (July 1951), p. 615.

[21] Ce Liu. „Beyond pixels: exploring new representations and applications for motion analysis“. PhD thesis. 2009.

[22] Shirly Ben David Makhluf, Riam Qasem, Sara Rubinstein, Aharon Gedanken, and Haim Breitbart. „Loading magnetic nanoparticles into sperm cells does not affect their functionality“. In: *Langmuir* 22.23 (2006), pp. 9480–9482.

[23] Edwin M. McMillan. „A History of the synchrotron“. In: *Physics Today* 37.2 (1970), pp. 31–37.

[24] Alexander Meaney. „Design and Construction of an X-ray Computed Tomography Imaging System“. In: 1 (2015), p. 75.

[25] M E Metska and Thorsten M. Buzug. „Computed Tomography“. In: (2008), p. 526.

[26] Edward Mitchell, Peter Kuhn, and Elspeth Garman. „Demystifying the synchrotron trip: A first time user's guide“. In: *Structure* 7.5 (1999), pp. 111–121.

[27] Rajmund Mokso, Daniel A. Schwyn, Simon M. Walker, Michael Doube, Martina Wicklein, Tonya Müller, Marco Stampanoni, Graham K. Taylor, and Holger G. Krapp. „Four-dimensional in vivo X-ray microscopy with projection-guided gating“. In: *Scientific Reports* 5 (2015), pp. 1–6.

[28] Jennifer L. Mueller and Samuli Siltanen. *Linear and Nonlinear Inverse Problems with Practical Applications*. USA: Society for Industrial and Applied Mathematics, 2012.

[29] Viktor V. Nikitin, Marcus Carlsson, Fredrik Andersson, and Rajmund Mokso. „Four-Dimensional Tomographic Reconstruction by Time Domain Decomposition“. In: *IEEE Transactions on Computational Imaging* 5.3 (2019), pp. 409–419.

[30] W.J. Palenstijn, K.J. Batenburg, and J. Sijbers. „Performance improvements for iterative electron tomography reconstruction using graphics processing units (GPUs)“. In: *Journal of Structural Biology* 176.2 (Nov. 2011), pp. 250–253.

[31] Cameron J. Ritchie, Jiang Hsieh, Michael F. Gard, J. David Godwin, Yongmin Kim, and Carl R. Crawford. „Predictive respiratory gating: A new method to reduce motion artifacts on CT scans“. In: *Radiology* 190.3 (1994), pp. 847–852.

[32] Wilhelm C. Röntgen. „On a New Kind of Rays“. In: *Nature* 53.1369 (1896), p. 274.

[33] A. Ruhlandt, M. Töpperwien, M. Krenkel, R. Mokso, and T. Salditt. „Four dimensional material movies: High speed phase-contrast tomography by backprojection along dynamically curved paths“. In: *Scientific Reports* 7.1 (Dec. 2017), p. 6487.

[34] Guglielmo Saggiorato, Luis Alvarez, Jan F. Jikeli, U. Benjamin Kaupp, Gerhard Gompper, and Jens Elgeti. „Human sperm steer with second harmonics of the flagellar beat“. In: *Nature Communications* 8.1 (2017).

[35] M. Stampanoni, F. Marone, P. Modregger, B. Pinzer, T. Thüring, J. Vila-Comamala, C. David, and R. Mokso. „Tomographic hard x-ray phase contrast micro- and nano-imaging at TOMCAT“. In: *AIP Conference Proceedings* 1266.July 2010 (2010), pp. 13–17.

[36] Daniela Tiedemann, Ulrike Taylor, Christoph Rehbock, Jurij Jakobi, Sabine Klein, Wilfried A. Kues, Stephan Barcikowski, and Detlef Rath. „Reprotoxicity of gold, silver, and gold-silver alloy nanoparticles on mammalian gametes“. In: *Analyst* 139.5 (2014), pp. 931–942.

[37] Jussi Toivanen, Alexander Meaney, Samuli Siltanen, and Ville Kolehmainen. „Joint reconstruction in low dose multi-energy CT“. In: *Inverse Problems & Imaging* 14.4 (2020), pp. 607–629.

[38] Vincent Van Nieuwenhove, Jan De Beenhouwer, Thomas De Schryver, Luc Van Hoorebeke, and Jan Sijbers. „Data-Driven Affine Deformation Estimation and Correction in Cone Beam Computed Tomography“. In: *IEEE Transactions on Image Processing* 26.3 (2017), pp. 1441–1451.

[39] P. Villanueva-Perez, B. Pedrini, R. Mokso, *et al.* „Hard x-ray multi-projection imaging for single-shot approaches“. In: *Optica* 5.12 (Dec. 2018), p. 1521.

[40] Simon M. Walker, Daniel A. Schwyn, Rajmund Mokso, Martina Wicklein, Tonya Müller, Michael Doube, Marco Stampanoni, Holger G. Krapp, and Graham K. Taylor. „In Vivo Time-Resolved Microtomography Reveals the Mechanics of the Blowfly Flight Motor“. In: *PLoS Biology* 12.3 (2014).

[41] Viroj Wiwanitkit, Amornpun Sereemaspun, and Rojrit Rojanathanes. „Effect of gold nanoparticles on spermatozoa: the first world report“. In: *Fertility and Sterility* 91.1 (Jan. 2009), e7.

[42] Wenhui Wu, Joseph Budovec, and W. Dennis Foley. „Prospective and Retrospective ECG Gating for Thoracic CT Angiography: A Comparative Study“. In: *American Journal of Roentgenology* 193.4 (Oct. 2009).

Electron Microscopy

A

Two 3D electron microscopy data sets were collected at Core Facility for Integrated Microscopy, Department of Biomedical Sciences, Copenhagen University. One dataset contains a volume of human sperm; the other contains a volume of boar sperm. The boar sperm was of the Duroc breed. The sperm was spun into a pellet using a centrifuge in both cases. The sperm were then fixed with glutaraldehyde and stained with Osmium, and encased in Epon.

The data was segmented by the neural network implemented by William Laprade while employed at the Department of Computer Science, Copenhagen University. Training data was created by segmenting some of the data manually. The work is ongoing. Below is a status of the progress showing images of the progress.

A.0.1 The human sperm data

The human dataset was analyzed first. Masks, as shown in Figure A.1(a), were created manually. A neural network was trained with the masks and segmented the data. The segmented data was thresholded and converted to a mesh, Figure A.1(b). The initial results showed that the data was very dense, so it is impossible to distinguish single cells in the rendering of the segmented volume. As the sperm are long and thin, a combination of high resolution and a large volume is needed to capture the whole cell. The volume shown comprises nine separate blocks of segmented data, which was necessary to find a whole cell. Because of the density of the data, the cells were not separated, and the data needed much post-processing to obtain just one cell shown in Figure A.1(c). A script was created to automatically create a centerline for the segmented cell, shown in orange. The skeletonized output was the desired output. The aim was to build a model for sperm poses using the skeletons. However, the post-processing was too time-consuming, and therefore more work was put into improving the initial segmentation.

(a) Human sperm mask

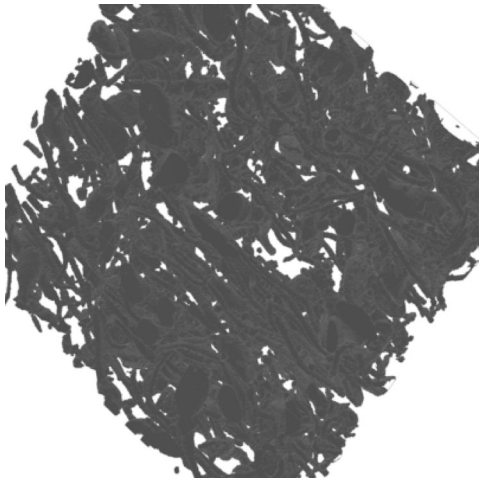

(b) Segmented volume of human sperm

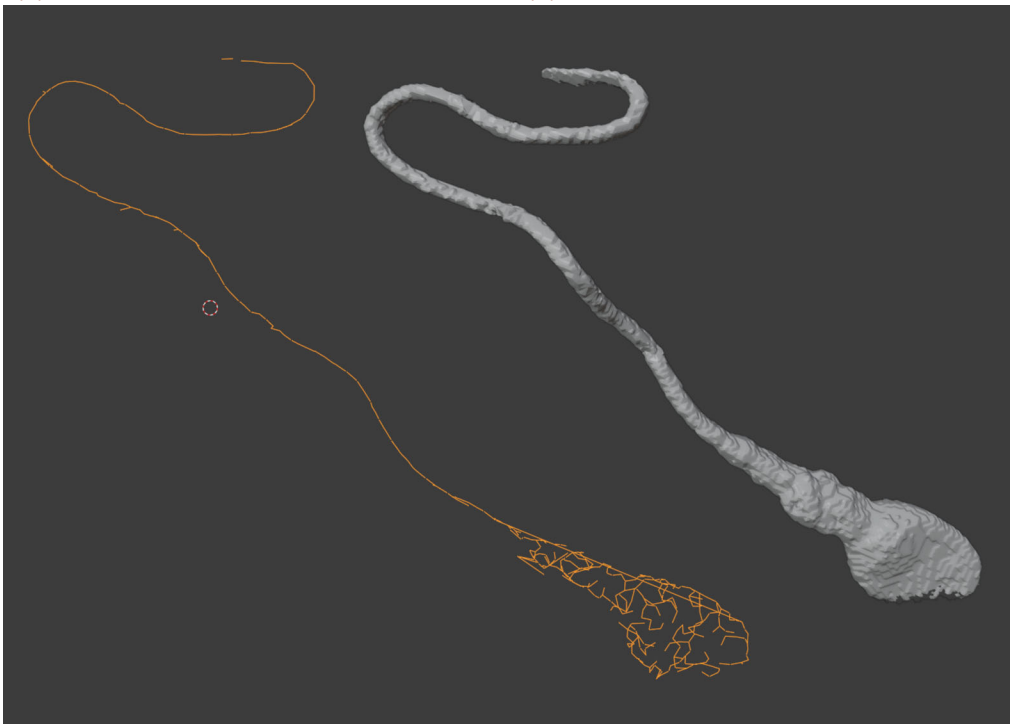

(c) Segmented single human sperm

Figure A.1.: Human sperm (a) An example of a mask used to train the network (b) An example of the output of the segmentation. (c) The output after manually finishing the segmentation and skeletonizing the mesh of one human sperm.

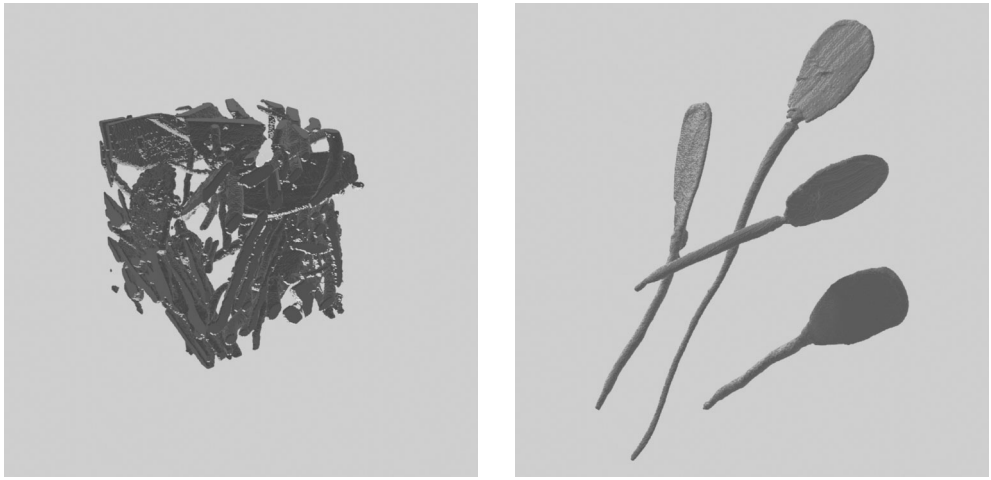

(a) Segmented volume of boar sperm **(b)** Segmented single boar sperm

Figure A.2.: Boar sperm (a) An example of a block of segmented boar sperm (b) Four single boar sperm automatically segmented. (c)

A.0.2 The boar sperm data

The focus was redirected at segmenting the boar sperm data as boar sperm were easier to use for practical reasons during the synchrotron X-ray experiments that the segmentation was meant to support. New masks were created for the boar sperm data. The initial segmentations suffered from the same problems as the human data. The data was very dense, and the sperm were too close together to get a good separation. Therefore, a block of the data was converted to meshes, Figure A.2(a), and was manually post-processed in 3D in Blender, where it was much easier to see the errors. The post-processed meshes were then voxelized to create new training data. In the end, it was possible to get single sperm automatically segmented, see Figure A.2(b). Unfortunately, none of them was full length when the cells were measured. Only the heads, mid-pieces and sometimes part of the tails were visible.

B

Light Sheet Flourescent Microscopy

A total of four datasets using light-sheet flourescent microscopy at the Spanish Institute of Photonic Sciences (ICFO) in Barcelona were acquired. The instrument has also been used to image zebra fish [6].

The data acquired showed promise as an alternative to SXRT for live 3D+t sperm imaging. The first imaging provided 3D+t volumes of live boar sperm at a speed of ten volumes per second. However, when the data were analyzed, it became clear that a strange and unexplainable mirror artefact was present, see Figure B.1. The same segmented sperm is shown from the front and the top. This initial segmentation based on a crude threshold looks promising when looking from the front, as the sperm shape is evident. However, when looking from the top, the sperm is mirrored.

Furthermore, the data is highly anisotropic with voxel sizes measuring $0.29 \times 0.29 \times 3\mu$m, which makes especially tail segmentation hard. Various attempts were made at improving the data and the segmentation. In December 2021, following an upgrade of their imaging system, we received a final dataset from ICFO. Two datasets were received, one with a time resolution of 40 full volumes per second and one with 70 full volumes per second. Unfortunately, there was no time to analyze the data as part of this PhD project, but the work is still ongoing.

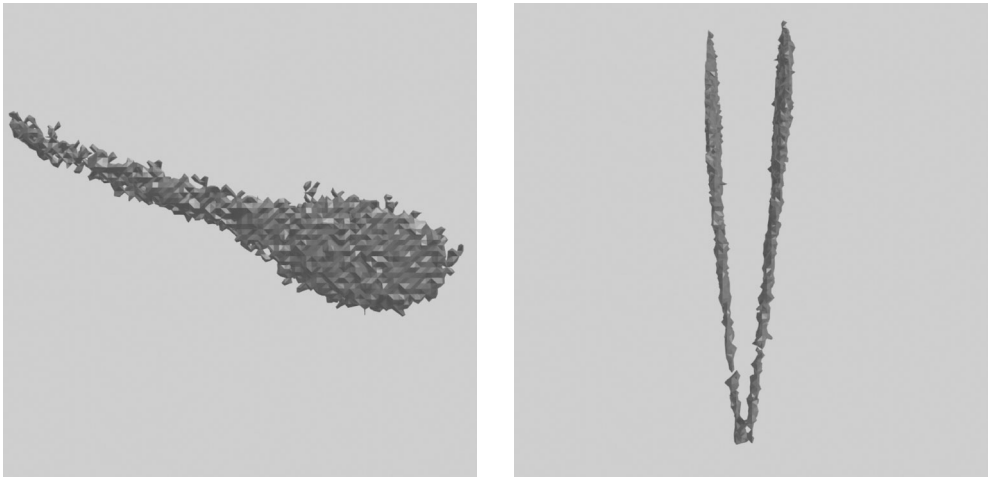

(a) Front view of segmented sperm

(b) Top view of segmented sperm

Figure B.1.: LSFM segmentations